DEFORMATION PROCESSES OF METALLIC OPEN-CELL FOAM SUPPORTED SHEET METALS

A Dissertation

by

CHENG-KANG YANG

Submitted to the Office of Graduate and Professional Studies of
Texas A&M University
in partial fulfillment of the requirements for the degree of

DOCTOR OF PHILOSOPHY

Chair of Committee,	Jyhwen Wang
Committee Members,	Anatasia Muliana
	Ibrahim Karaman
	Ramesh Talreja
Head of Department,	Andreas A. Polycarpou

December 2016

Major Subject: Mechanical Engineering

ABSTRACT

Sandwich panel has been widely applied to enhance the stiffness to weight performance of components in many industries. The manufacturing procedure of curved metal sandwich panels typically consists of forming the sheet and core material into prescribed shapes and applying the adhesive to bond the material in shaped molds. An alternative manufacturing method is to apply the conventional sheet metal forming technique to deform the flat sandwich panel into a curved panel. However, the face sheet will significantly limit the formability of the sandwich panel. To solve the problem, one face sheet was removed in the sandwich panel to increase the formability, then the metal sheet and the metallic open-cell foam were selected as the face sheet and the core material to form the metallic open-cell foam supported sheet metals.

The main objective of this study is to develop a proper forming method to deform the metallic open-cell foam supported sheet metal without failure occurring. Two forming processes, press brake bending and hydroforming, which can reduce the contact stress to avoid the structure damage were investigated. Experiments were designed to understand the possible failure modes and the failure mechanism. Through the parametric study in the experimental results, the effects of material dimensions, material properties, and test parameters were analyzed to establish a failure criterion. In addition, a finite element analysis with a proper foam model was implemented to further inspect the failure mechanism and develop a guideline for the selection of materials and test parameters.

For the press brake bending process, the experiment results have shown that the supported sheet metal can be successfully bent into a curved panel within small thickness reduction. The prediction in both geometric hoop strain failure criterion and shear strain failure in the finite element analysis were matched and agreed with the experimental result. For the hydroforming process, the experimental result indicated that the major failure mode is the adhesive failure. The early adhesive failure at the perimeter of the attached foam disc caused the open-cell foam to separate from the sheet metal. The required adhesive strength to the attainable dome height relationship was given by finite element analysis.

ACKNOWLEDGEMENTS

I would like to thank my committee chair, Dr. Wang, and my committee members, Dr. Muliana, Dr. Karaman, and Dr. Talreja, for their guidance and insightful comments on my research and dissertation.

Thanks also go to my friends, Yin-Ping Chen, Ya-Jen Yu, and Chia-Lan Liu, my colleagues and the department staff for their help and advice.

Finally, thanks to my mother, Chun-Man Hsu, my father, Wu-Hsiung Yang, and my wife, Hsing-Yi Tsai, for their patience, love, and endless support.

CONTRIBUTORS AND FUNDING SOURCES

Contributors

This work was supervised by a dissertation committee consisting of Professor Jyhwen Wang [advisor], Professor Anatasia Muliana and Professor Ibrahim Karaman of the Department of Mechanical Engineering and Professor Ramesh Talreja of the Department of Aerospace Engineering.

The experiment in the Michigan State University apparatus for Chapter V was conducted by Professor Farhang Pourboghrat at Michigan State University. The sample used in the Michigan State University apparatus for Chapter V was provided by Mahesh Nair and Bright Wadja.

All other work conducted for the dissertation was completed by the student independently.

Funding Sources

The work was supported by National Science Foundation under Grant Number CMMI-0825986.

TABLE OF CONTENTS

Page

LIST OF FIGURES

Page

LIST OF TABLES

Page

CHAPTER I

INTRODUCTION

Light-weight sandwich panels are commonly used in various industries to improve the stiffness or reduce the weight of structure components. In aviation and aerospace industry, sandwich panels are widely adopted in body and airfoil design to obtain a better stiffness to weight ratio. In automotive industrial, sandwich panels are designed as shock-absorbing and impact-resistant materials in the racing car. In the past decades, researchers have developed new materials and also improved the manufacturing processed to create the high-performance sandwich panels. Sandwich panel is a structure made of two layers of face sheets and one layer of light-weight core material. The light-weight core material is bonded by the two face sheets to provide high structure stiffness. The commonly used face sheet material includes sheet metal and fiber-reinforced polymers. The commonly used core material includes honeycomb structures, polymer foam, and balsa wood.

Traditionally, the wet lay-up and prepreg layup methods are used to fabricate sandwich panels. These methods require only simple workshop techniques, inexpensive tools, and equipment to bond the face sheet and core materials together. With the evolution of manufacturing automation, flat sandwich panels could be continuously laminated by the double belt press, as shown in Figure 1. In contrast, manufacturing sandwich panels with a curvature requires a more complicated manufacturing procedure before the adhesive being applied, especially for those hard-to-form face sheet and core

materials. For instance, the stiff metal sheet needs to be stamping into curved shape before the bonding process, and the core materials, such as metallic foam, require a CNC or EDM machine to cut them into the curved shape. Besides the additional procedures, one or multiple molds that fit the final shape are also essential to keep the panels in shape during the adhesive curing process. Due to these additional procedures, the processes of producing curved sandwich panels become costly and timing consuming.

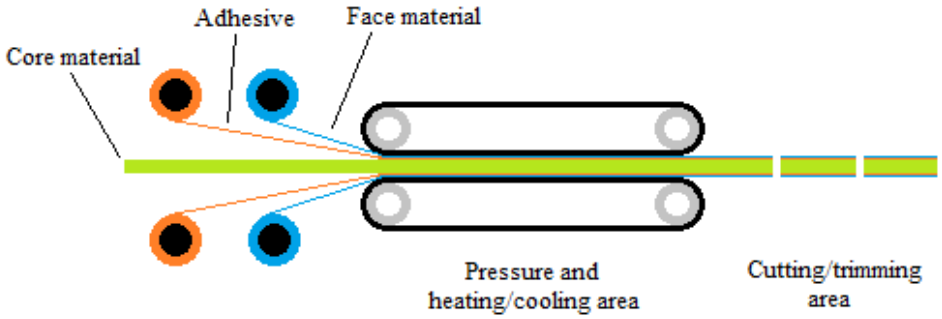

Figure 1 Schematic of continuous lamination using a double-belt press [1].

An alternative to replace the traditional approach for manufacturing curved sandwich panels is to utilize the sheet metal forming processes, such as bending, forging, deep drawing, and incremental forming, to deform the flat sandwich panels into curved shapes. These processes, however, generally resulted in the collapse of the core materials and damaged the sandwich structure as observed from the previous research results. Elzey et al. analyzed the open die forging of structural sandwich with the porous core material [2]. The result showed that the forging process could lead to non-uniform core density and thickness distribution, indicating an uneven collapse of the core material, in

the panels. Mohr conducted deep drawing experiments using thin sandwich blanks with metal face sheets and perforated sheet metal core [3]. The experiment results showed that bending could lead to a core shear failure, which is also the dominant failure mechanism. Moreover, the numerical analysis result also indicated that the required core shear strength to successfully form sandwich panels by deep drawing is proportional to the face sheet strength. Jackson conducted experiments in incremental sheet forming of sandwich panels [4]. With the loading from the forming tool/pin, the soft core was non-uniformly deformed. Figure 2 illustrates the deformed sandwich panels under these forming processes.

From the previous results, it is found that the high contact stress between the tool/die and the sandwich blank can cause the crushing or fracture of the lower strength core material. Once the structure is damaged, the panel no longer has the original stiffness. The structure of sandwich panel could not sustain a large deformation. The high bending stiffness causes a large contact stress to forming, and the process could result in indenting the face sheets or crushing the core material. Meanwhile, the two bonded face sheets guide the core material to a large shear deformation, causing adhesive failure (debonding) or shear failure in the low strength core materials.

Some sheet metal forming techniques could be applicable in forming of two layered panels, which consists of a face sheet supported by a core material. Although the two-layered panels have a reduced bending stiffness compared to the typical sandwich structures, it could prevent the panels from debonding and core shear during the forming process. With controlled contact stress during forming, the two-layered panels could be

kept at a thickness close to that of the original. Besides, an additional face sheet could be attached to the formed two layered panels to produce sandwich panels with increased stiffness.

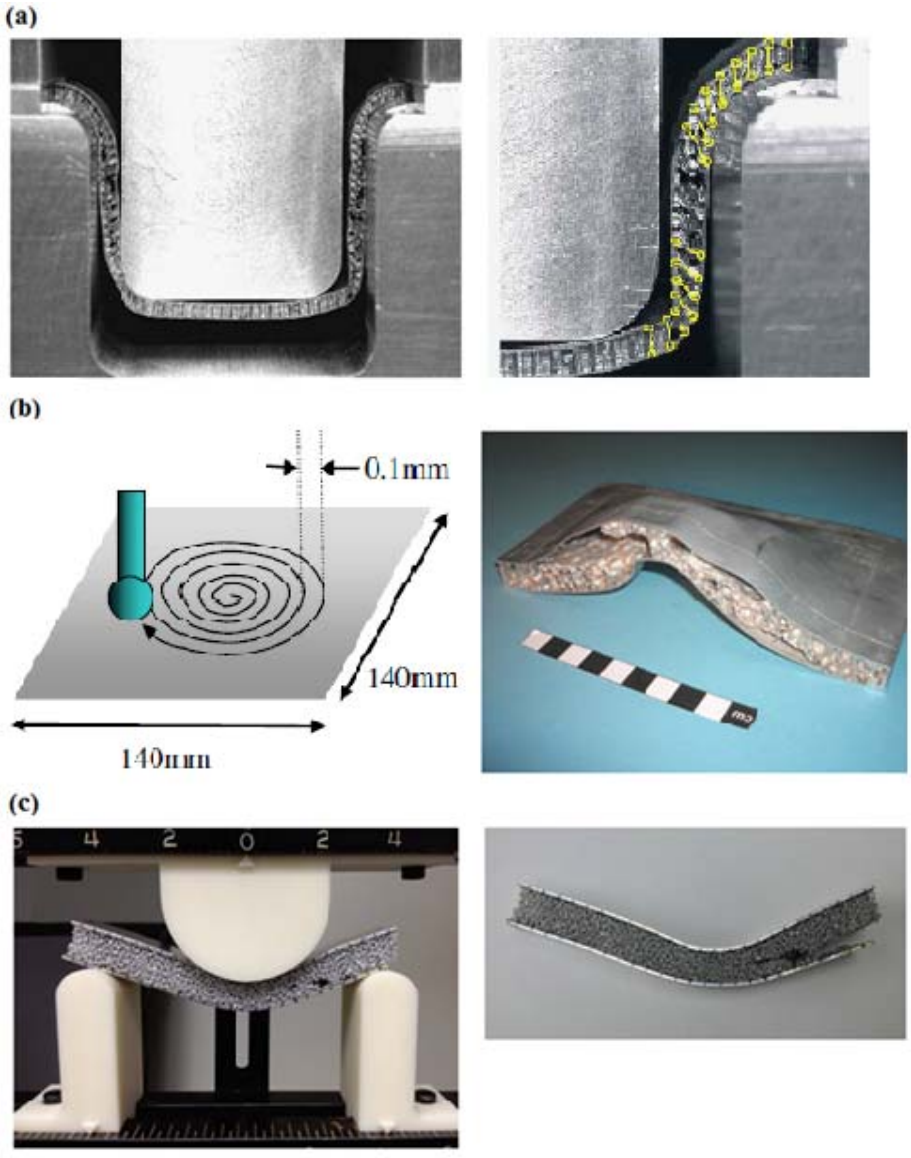

Figure 2 Sandwich panels failure under different forming processes: (a) Deep drawing [3], (b) Incremental forming [4], (c) Three points bending.

This research takes the structural advantages of the two-layered panels, and proposed two different manufacturing methods, press brake bending and hydroforming, to deform the panels into a curved shape. These two processes are designed to distribute the forming force evenly over the panel, and prevent the large contact stress causing the collapse of the core materials. The first method, press brake bending process, is developed based on the mechanics of three points bending. The support pins and center pin are changed to a larger semicircular punch. Ideally, the forming force is dispersed over the panels with the increased contact area. The second method, hydroforming process, utilizes the hydraulic fluid as working media to distribute the forming pressure uniformly over the panel, as shown in Figure 3.

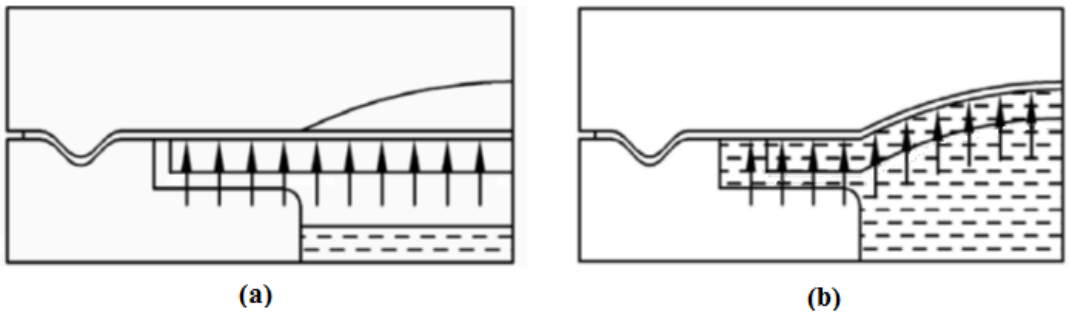

Figure 3 (a) The upper face sheet is clamped to sealed the chamber, (b) With continuous increase of the hydraulic pressure, the panel can be deformed.

The two-layered panel is expected to be under a larger plastic deformation in the forming processes; therefore, a good formability of the panel is essential. The aluminum sheet metal and the aluminum metallic open-cell foam are selected to construct the two-layered panels. The face sheet and the core are joined by a thin layer of commercial

acrylic adhesive. The good ductility in the sheet metal and the acrylic adhesive makes the panel formable for the tensile deformation, and the porosity of the open-cell foam gives the space for the compression deformation. The pores of the open-cell foam are also beneficial to the hydroforming process. The fluid could enter the pores and directly exert the forming pressure on the sheet metal; hence the foam crushing failure could be prevented.

To summarize the work in this dissertation, previous works on sandwich bending theory, sheet hydroforming process, and the material properties characterization of metallic open-cell foams are reviewed in Chapter II. The experiment result of the press brake bending process is concluded and analyzed in Chapter III. In addition, a geometric failure criterion is proposed to predict the indentation failure based on the experimental observations. In Chapter IV, Kelvin cell model is introduced to simulate the bending behavior of open-cell foam in the finite element analysis of the press brake bending process. Chapter V presents the experimental results and the finite element analysis of hydroforming process. The conclusions and future works are discussed in Chapter VI.

CHAPTER II

LITERATURE REVIEW

In this research, the main objective is to deal with the plastic deformation of the metallic open-cell foam supported sheet metal. To provide a basic background of this research, the review of previous works is divided into three areas: beam bending theory, material characterization of metallic open-cell foam, and sheet hydroforming deformation process. To describe and model the deformation behavior of metallic open-cell foams appropriately, the material response, effective material property model, yielding criterion, and modeling technique of metallic open-cell foam are reviewed in the first section To benefit from the past works on the bending of the layered material, elastic-plastic beam bending theory, sandwich beam bending theory, and failure mode map of bending sandwich panels are reviewed in the bending theory section. The last section is to inspect the research methodology of sheet hydroforming process. Based on the literature review, the research method of this dissertation is described in the last section.

2.1 Material behavior of metallic open-cell foam

Metallic open-cell foam is used intensively in light-weight sandwich panels as core materials. Various manufacturing methods can lead to dissimilar foam structures and material behaviors in open-cell metallic foams. In general, the structure of metallic open-cell foam consists of numerous random ligaments and cavities. The metallic open-cell foam can be produced by creating gas bubbles in the metal liquid or by casting in the

investment which is used a polymer foam as a filler material to create the casting space. Figure 4 illustrates the fabrication methods of metallic open-cell foam. These fabrication methods usually lead to a non-uniform foam structure. In the gas injection process, the buoyancy of the bubbles rises to the liquid surface, and the viscosity of the liquid causes the gas bubble shape to become an ellipsoid. In the investment cast process, the filled polymer foam is subjected to the weight of the slurry, and in the compressed foam, the length of the cavity in the gravity direction is shorter than that in the directions perpendicular to the gravity direction. In both processes, the cavity of the open-cell foam structure can be considered as stretched in one direction. To identify the microstructure of the open-cell foam, the direction in stretch direction is called the rise direction, and the perpendicular direction is called the transverse direction. Figure 5 shows the rise and transverse direction in the open-cell foam structure. The stretched cavity leads the ligaments length in the rise direction is slightly longer than the ligament in the transverse direction and generates the anisotropy in the material properties of open-cell foam.

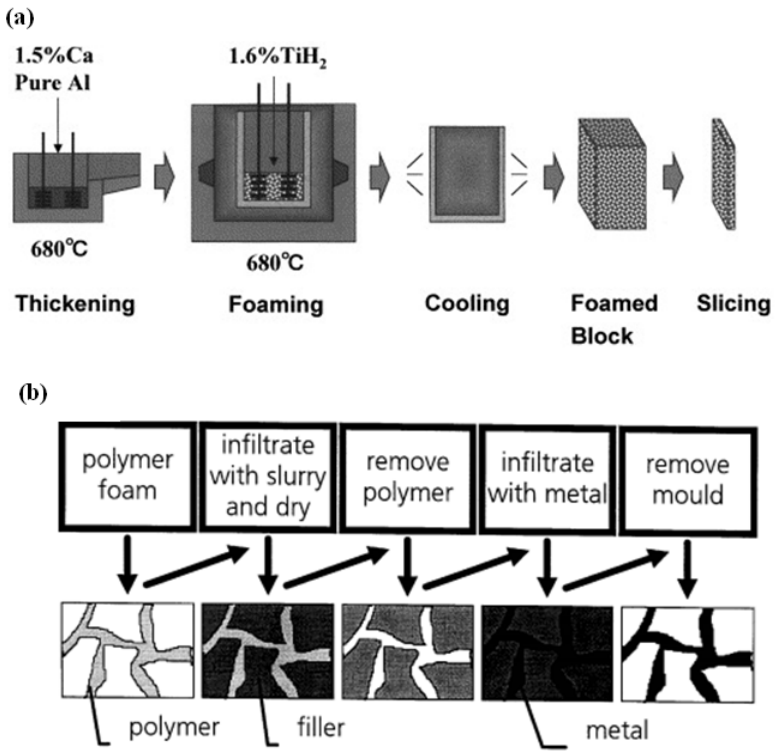

Figure 4 Metallic open-cell foam fabrication methods, (a) Gas injection method, (b) Investment casting (down casting) [5].

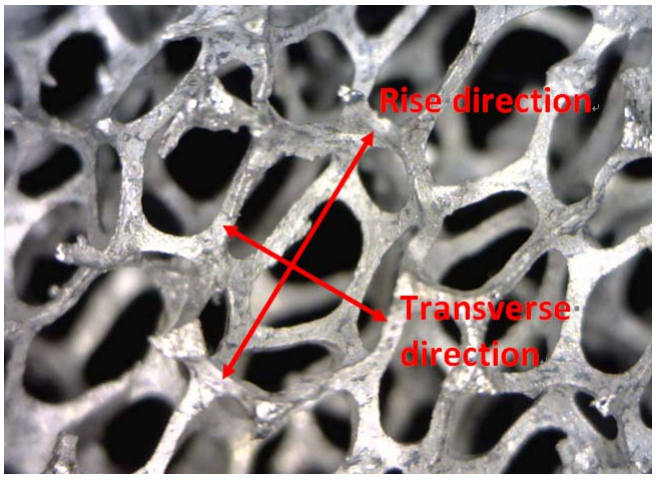

Figure 5 Rise direction and transverse direction of the cavity in Duocel 40 PPI 4-6% Al 6101-T6 open-cell foam.

2.1.1 Structure characterization

To characterize a metallic open-cell foam structure, pore size and relative density are the most important parameters that describe the shape and the composition of the open-cell foam. The pore size defines the cell size of the microstructure and the relative density gives the ligament size of the cell. Combined these parameters with the base material, the mechanical response of the open-cell foam can be described. The following paragraphs discuss the pore size, relative density, and base material individually and explain their effects on the mechanical properties.

Pore size

During the fabrication process, each bubble in the open-cell foam will build a cell generally consists of 14 windows, and pore is the open window in the cell. Figure 6 plots the definition of pore and cell. The size and shape of each pore are different from one to another. To statistically specify the open-cell foam, the value of pores number per inch (PPI) is used to evaluate the pore size. The average value of PPI in metallic open-cell foam is 5 to 40 [6]. Figure 7 shows the cell size difference of Duocel 6-8% Al 6101 aluminum in 10, 20 and 40 PPI. The pore size has a direct effect on the size of the geometric parameters in open-cell foam, such as nominal cell size, ligament length, cross-section area and pore diameter.

Relative density

Relative density is the ratio of the actual foam density to the fully solid material density. The relative density value counts the percentage of the occupied volume by the

material in the foam structure. Metallic foam is defined as a high porosity material, and the relative density range is 3% to 25%. Typically, the relative density for metallic open-cell foam is 3% to 15%, and the relative density for metallic close-cell foam is above 15% to 25%. A large value of relative density means the open-cell foam has thicker ligaments, and the pores may be filled with the material. The cross-section profile of metallic open-cell foam also varies with the relative density. The ligament profile has a direct effect on the mechanic response of the open-cell foam. Figure 8 demonstrates Duocel aluminum open-cell foam in 4.85%, 7.69%, and 11.14% at 40 PPI. Figure 9 shows the cross-section profile of Duocel foam in different relative density. Hence, relative density controls the size and the shape of the cross-section profile in the ligament.

Base material

Open-cell foam can be manufactured with many materials such as carbon, aluminum, steel, and various polymers. This base material determines the physical properties of open-cell foam, such as thermal expansion, melt temperature, and specific heat. The mechanical properties of the open-cell foam, such as modules, yielding strength, and thermal conductivity are related to the base material properties and the relative density. In general, the relative density has a dominant influence on the open-cell foam mechanical properties.

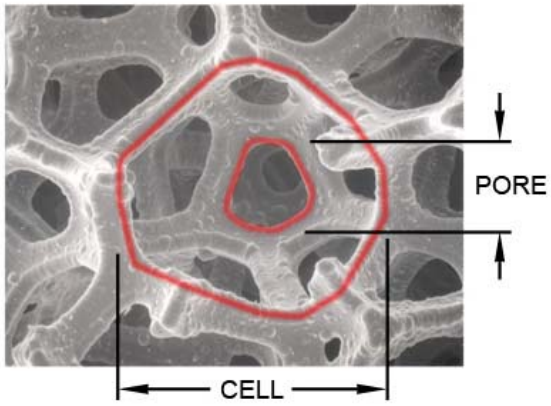

Figure 6 Pore and cell definition in open-cell foam structure [6].

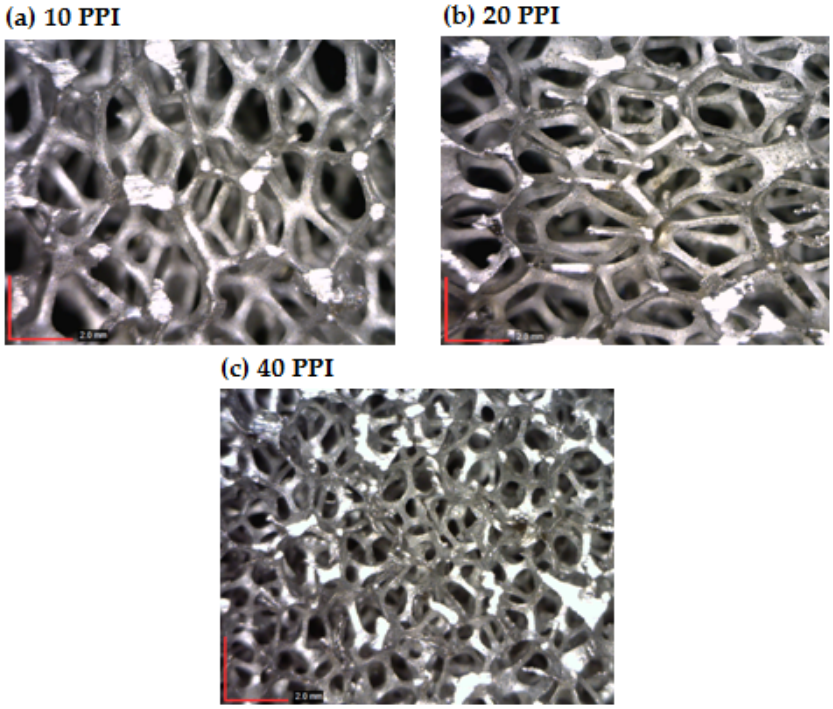

Figure 7 6-8% Duocel aluminum open-cell foam in various pore size, (a) 10 PPI, (b) 20 PPI, (c) 40 PPI.

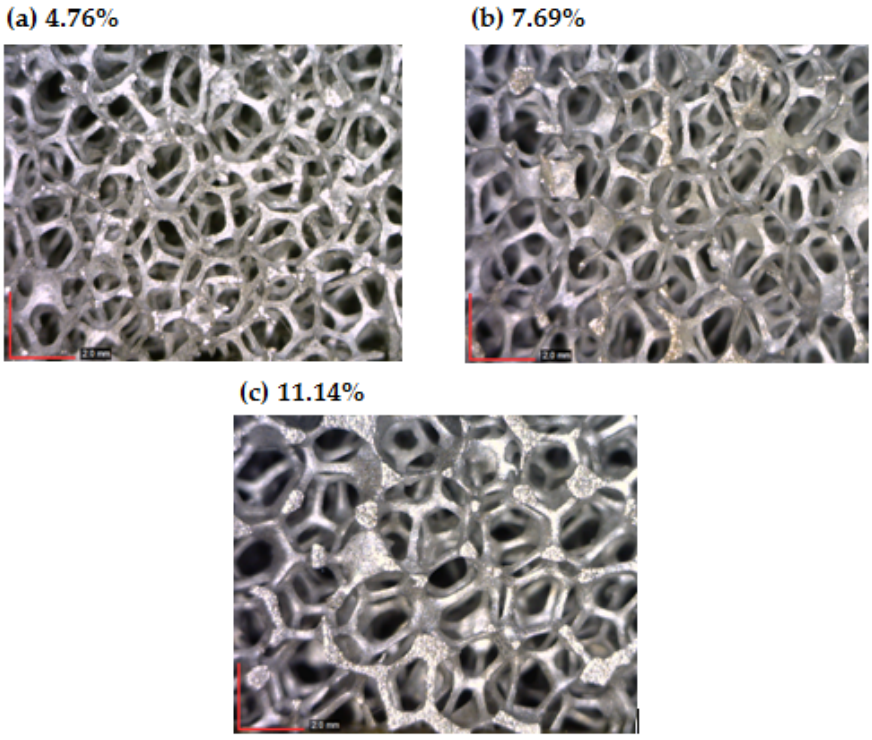

Figure 8 Duocel 40 PPI Al 6101-T6 open-cell foam in (a) 4.76%, (b) 7.69%, (c) 11.14 %.

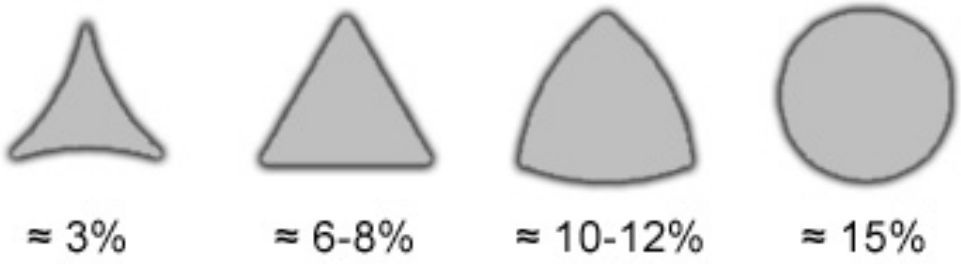

Figure 9 Ligament cross-section profile of Duocell open-cell foam at various relative density [6].

2.1.2 Deformation of metallic open-cell foam

From the experimental observation in the compress test, metallic open-cell foam has an elastic-plastic stress-strain response. Figure 10 shows the schematic compressive stress-strain curve of an elastic-plastic foam. The curve shows a linear stress response at low strain, then followed by a long collapse plateau and ended in a steep stress hardening behavior due to densification. Through the detail observation in the microstructure of metallic open-cell foam, the linearity of elasticity is controlled by the ligament bending. The plateau is associated with the plastic hinge in the ligament. When the foam was around 70% compress strain, the further compression led to ligaments contact and caused the rapidly increased stress. From the material property aspect, a larger relative density of open-cell foam will build up the elastic modulus, raise the plastic plateau stress, and reduce the strain at the initial densification [7].

The stress-strain response of the metallic foam in the double lap shear test is demonstrated in Figure 12. The shear stress is linear at the low shear strain and turns into a decreasing curve after it passes the peak value. The shear strength is defined as the peak point in the curve. Figure 13 shows the shear strength of metal foam with various relative densities.

Past research and experiments result indicated the measured shear response of the open-cell foam is affected by the sample size in the experiment. Gibson et al. have indicated the size effects on the elastic modulus, yielding strength and shear strength of Alpha and Duocel foams [8]. Figure 14 illustrates the measured material properties in different sample size ratios. When the normalized size of the test sample is close to the

unit cell length, the elasticity module is less than half of the value of that measured from the sufficient size. In contrast, the value of shear strength becomes larger when the sample dimension is close to the length of a unit cell. Fleck and Chen indicated the sample is constrained at the boundary when the test dimension is not enough [9]. The suggested test sample size is 7 cells in the length direction for uniaxial compress test and 3 cells in the thickness direction for the double lap shear test [10].

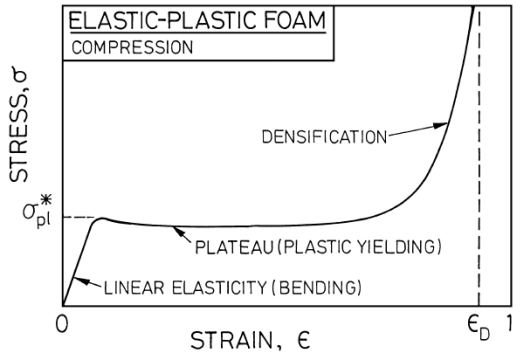

Figure 10 Typical compressive response of cellular metal foam [7].

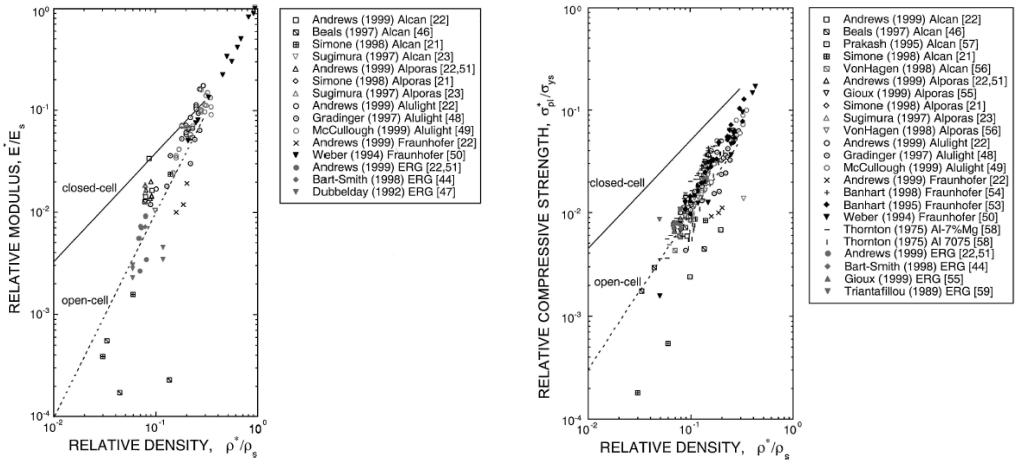

Figure 11 Effective material properties of open-cell foam via different relative density (a) Relative modulus (b) Relative compressive strength [7].

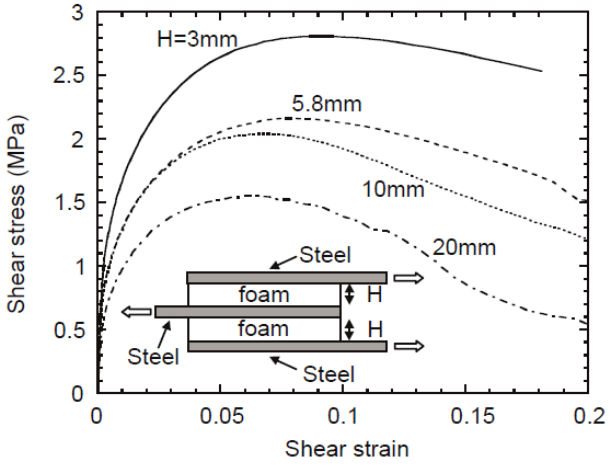

Figure 12 The shear response of Alporas aluminum foam at 11% relative density in the double lap shear test via various foam thickness [9].

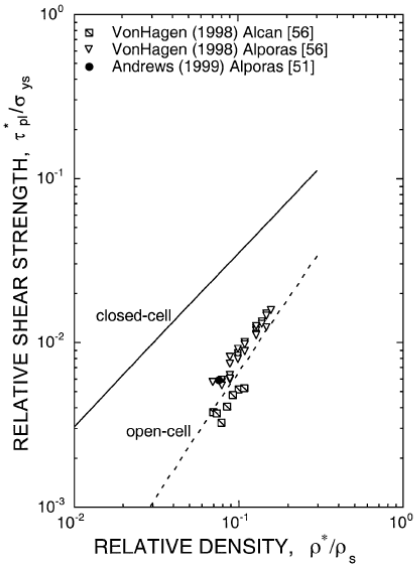

Figure 13 The shear response of Alporas aluminum foam at 11% relative density in the double lap shear test via various foam thickness [9].

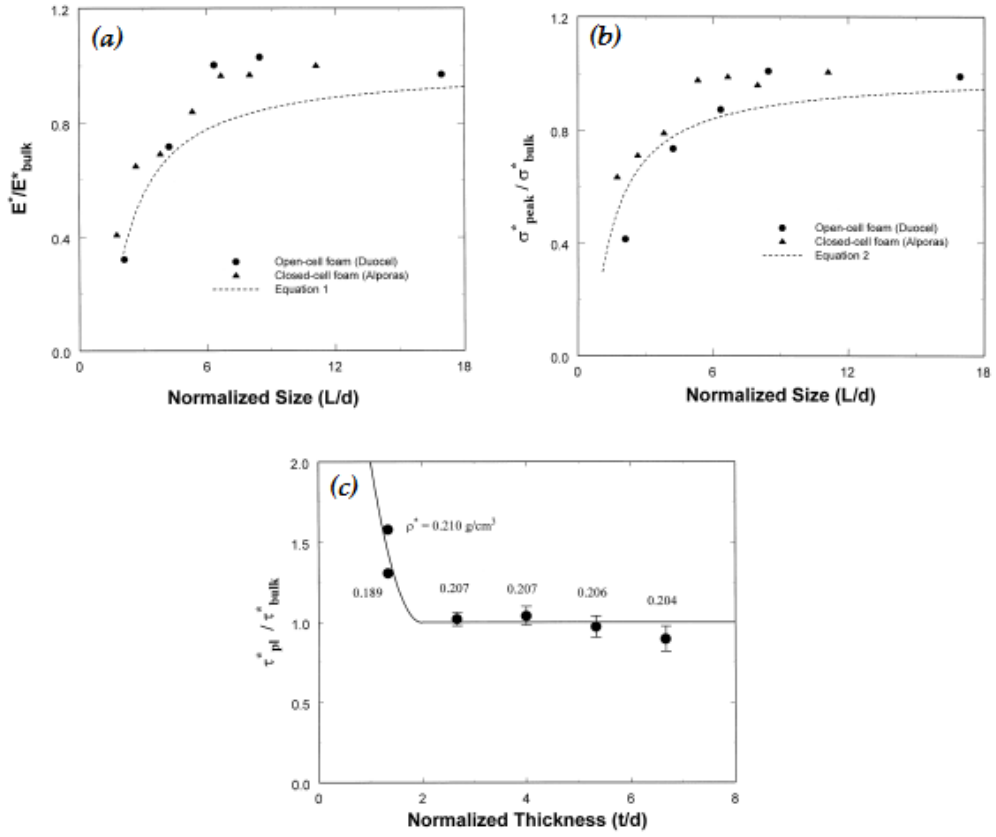

Figure 14 Size effects on the measured mechanical properties via various sample size: (a) Relative elastic modulus, (b) Relative collapse strength, (c) Relative shear strength [11, 12].

2.1.3 Mechanical properties of metallic open-cell foam

Useful surveys on the mechanics of cellular solids are contributed by Gibson and Ashby [7], and Kraynik and Warren [13], and Betts [14]. From the observation in the experimental result of the uniaxial compression test and shear test, the relative mechanical properties for low density foams are linear to the power of the relative density. A review of the material behavior investigation in metallic open-cell foam shows the major modeling methods fall into two major categories, (1) Analytical

analysis with idealized cell structures; (2) Numerical analysis in repeated unit cells or random cells [14, 15]. Analytical modeling methods provide an excellent prediction of the mechanical properties in the linear small strain, and the prediction is off from the experimental observation when the strain is large. As a result, scientists applied numerical methods to simulate the nonlinear behavior of open-cell foam under large strain deformation.

Analytical modeling methods utilize the dependent foam properties to analyze the mechanical response of open-cell foam and predict the effective mechanical properties. In analytical method, an idealized geometry is selected to depict the microstructure of open-call foam and the dependent foam parameters, such as relative density and pore number, are used to describe the ligament size and the scale of the unit cell. The equivalent material properties are obtained through the investigation of the mechanical response in isolated strut [11, 16-19], isolated joints [13, 20-22], or isolated cell [23]. Among the idealized cell geometries, Ashby and Gibson cubic model and Kelvin cell model are the most significant microstructure for open-cell foams. The numerical methods typically consider a similar ligament arrangement to real open-cell foam in the simulation of the linear and nonlinear response. The perturbed Kelvin cell model and random Voronoi cell model are widely used to model the ligament arrangement in the numerical simulation. Figure 15 shows Ashby and Gibson's cubic cell model, Kelvin cell model and Voronoi cell model. Ashby and Gibson cubic cell model is discussed separately from Kelvin cell model and Voronoi cell model.

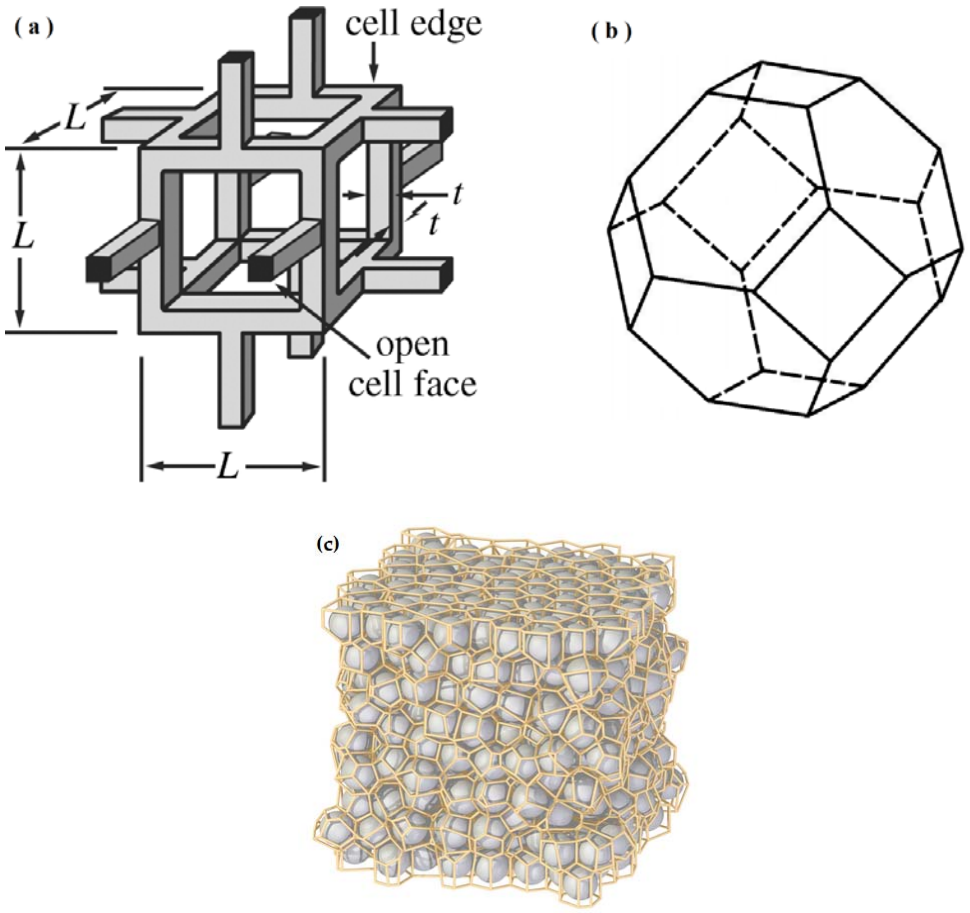

Figure 15 Idealized microstructure of open-cell foam, (a) Ashby and Gibson cubic cell model [24], (b) Kelvin cell model [8], (c) Voronoi cell model [25].

Ashby and Gibson cubic cell model

Ashby and Gibson have contributed significant efforts in the material behavior characterization of open-cell foams through experimental and analytical methods. The relative density was selected as the key parameters to predict open-cell foams' effective material properties. Ashby and Gibson constructed an idealized cubic open-cell model to analysis the elastic modulus and the collapsing stresses of open-cell foam [7]. The proposed open-cell foam material model shows the elastic modulus and yielding are proportional to the relative density of open-cell foam. The linear mechanical properties derivation of Ashby and Gibson's cubic model is presented in the following paragraph.

A typical cubic model is demonstrated in Figure 15.(a). The relative density of the cell, ρ^*/ρ_s (the foam density, ρ^*, divided by the solid material density of the cell ligament, ρ_s), and the second moment of area of a strut, I, are related to the dimensions t and l by:

$$\frac{\rho^*}{\rho_s} \propto \left(\frac{t}{l}\right)^2 \tag{2.1}$$

and

$$I \propto t^4 \tag{2.2}$$

Young's modulus for the open-cell foam is obtained from the calculation of the elastic deflection of the beam, which is loaded in the midpoint. The edge bending schematic is shown in Figure 16. From the beam bending theory, the deflection, δ, is proportional to Fl^3/E_sI, where E_s is the Young's modulus for the raw material. The load, F, is related to the effective stress, σ, by $F \propto \sigma l^2$ and the effective strain, ϵ, is

related to the deflection, δ, by $\epsilon \propto \delta/l$. The effective Young's modulus of open-cell foam, E^*, is given by

$$E^* = \frac{\sigma}{\epsilon} = \frac{C_1 E_s I}{l^4} = C_1 E_s \left(\frac{t}{l}\right)^4 \tag{2.3}$$

by substitute the relative density in the equation

$$\frac{E^*}{E_s} = C_1 \left(\frac{\rho^*}{\rho_s}\right)^2 \tag{2.4}$$

where C_1 is the geometric constant. The experiment results suggest $C_1 \approx 1$ for open-cell foam.

Shear modulus of open-cell foam is calculated with the similar method. The shear stress, τ, induces the shear strain, γ, through the bending of the ligament. The deflection is proportional to $Fl^3/E_s I$, the shear stress and shear strain are proportional to F/l^2 and δ/l, respectively. The effective shear modulus, G^*, is given by

$$G^* = \frac{\tau}{\gamma} = \frac{C_2 E_s I}{l^4} = C_2 \left(\frac{t}{l}\right)^4 \tag{2.5}$$

from which

$$\frac{G^*}{E_s} = C_2 \left(\frac{\rho^*}{\rho_s}\right)^2 \tag{2.6}$$

for cubic cell. The experimental data suggest $C_2 \approx 3/8$ for open-cell foam.

$$\frac{{\sigma_{pl}}^*}{\sigma_{ys}} = C_2 \left(\frac{\rho^*}{\rho_s}\right)^2 \tag{2.7}$$

The linear elastic and isotropic material indicates

$$G^* = \frac{E^*}{2(1+\nu)} \tag{2.8}$$

Substituting the effective Young's modulus and shear modulus in the equation, the effective Poisson's ratio is given by

$$\nu = \frac{C_1}{2C_2} - 1 = C_3 \tag{2.9}$$

where $C_3 \approx 1/3$.

The plastic collapse of the cubic cell happens when the moments exceed the maximum limit, and all the joints are under the plastic hinge. The formation of the plastic hinge in the cubic model is demonstrated in Figure 17. The plastic bending moment, $\mathrm{M_p}$, at the joint is

$$\mathrm{M_p} = \frac{1}{4}\sigma_{\mathrm{ys}}\mathrm{t}^3 \tag{2.10}$$

where σ_{ys} is the yielding strength of the raw material. The plastic bending moment, $\mathrm{M_p}$, is proportional to *Fl*. The stress of the foam is proportional to F/l^2. The effective plastic strength of open-cell foam, σ_{pl}^*, can be expressed as

$$\sigma_{pl}^* \propto \frac{M_p}{l^3} \tag{2.11}$$

Combined with the relative density, the relative plastic collapse strength is given by

$$\frac{\sigma_{pl}^*}{\sigma_{ys}} = C_4\left(\frac{\rho^*}{\rho_s}\right)^{3/2} \tag{2.12}$$

where C_4 contains the geometric constants. The experiment results suggest $C_4 \approx 0.3$ for open-cell foam.

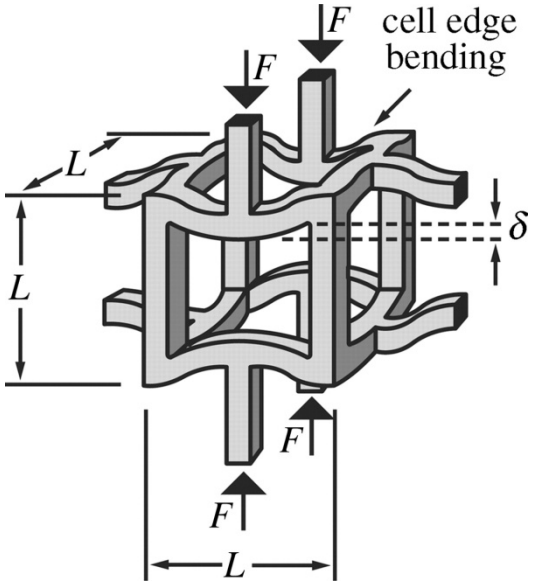

Figure 16 Cell edge bending during the elastic deformation [7].

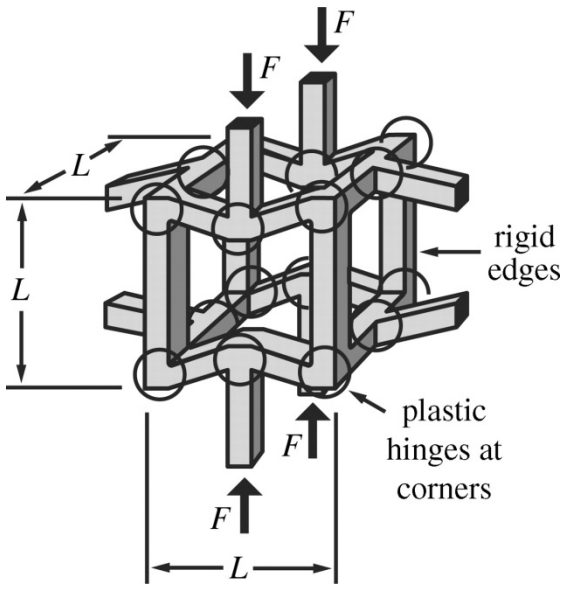

Figure 17 The plastic hinge formation in open-cell foam [7].

Kelvin cell model or Voronoi cell model

Kelvin cell model is a tetrakaidecahedron unit cell which contains six planar square faces and eight hexagonal faces and can be stacked up to show a regularly repeated foam structures [7]. Open-cell foam was first modeled with the tetrakaidecahedron unit cell by Dement'ev and Tarakanov [26]. Warren and Kraynik et al. presented a micromechanical analysis to obtain the linear elastic behavior of low density open-cell foam [13, 20-22]. Zhu and Mills et al. extended the analysis of tetrakaidecahedron unit cell into the high compression strain for PU foam [27, 28]. Gong and Jang developed several models for predicting the complete response of PU foam and aluminum open-cell foam [29]. From the result of the above research, Kelvin cell model also precisely predicts the elastic mechanical properties of open-cell foam.

For the nonlinear behavior of open-cell foam, such as the crushing response, the numerical analysis is introduced to analyze the behavior under the randomized structure and large strain deformation. It has been found the small perturbation reduce the sensitivity of the initial postbuckling response to the domain size [30]. The randomized structure was typically generated by a perturbed Kelvin cell model or Voronoi cell. A perturbed Kelvin cell model uses a small random scale to adjust the node position. Voronoi cell utilized randomly distributed cells with different size and shape to fill a space [14]. Both models produced a close ligament arrangement to the real open-cell foam structures.

For analyzing the size effect, Zhu et al. applied the finite element method to depict the size effects on the mechanical properties of the irregular open-cell foam [15, 31]. For

low relative density open-cell foam, the research has shown that the main mechanical response at low strain is the bending and twisting of the ligaments and the major response at high compressive strain is the struts buckling. Tekog˜lu and Onck et al. used 2D Voronoi cells to show the size effects of open-cell foam under different loads of compression, bending, shear and indentation [32]. The results show size effects is associated with the cell morphology and can be realized from the basic deformation modes. Li et al. further applied 3D Voronoi cells to investigate size effect in the dynamic response of close-cell foam and indicated the dynamic response is sensitive to the cell size when the material is rate dependent [33].

Kyriakides et al. have conducted a series of studies on the mechanical behavior of open-cell foam with Kelvin cells and random Voronoi cells under compressive loads. Gong et al. applied regular Kelvin cell model to predict the initial elastic modulus of foams and nonlinear aspects of the compressive response [29, 34, 35]. The study demonstrated that the onset of ligament buckling was associated with the first turning point in the measured response and it also showed the anisotropy of open-cell foam result in different crushing responses. Jang et al. continued the investigation into the crushing response of aluminum open-cell foams with Voronoi cells and Kelvin cells [30, 36-38]. Micro-computer X-ray tomography was utilized to develop the 3D image of open-cell foams and established the cell size and ligament length distribution. With the statistical data, Kelvin cell model is improved to have the same dependent foam properties with the actual open-cell foam and gives a better crush response prediction. Gaitanaros et al. utilized the Surface Evolver software to construct a 3D Voronoi cell

model and extended the numerical analysis of aluminum open-cell foam behavior in the dynamic crushing response at various impact speeds [39-41]. The simulation results show the impact speed can change the initial crushing location. Okumura et al. rendered some defects in the ligament and wall structure and observed the buckling behavior in the numerical analysis [42, 43].

With the advanced 3D print technology, the material in special lattice geometry can be produced and applied as the core material in the sandwich panel. A numerical method is widely used to predict the stress-strain distribution and indicates the failure modes [44-52]. Due to the precise geometry description in the ligament arrangement, the numerical analysis results are in excellent agreement with the experimental data.

2.1.4 Summary

From the review, it can be concluded that the analytical methods and numerical methods can have good predictions in mechanical properties of open-cell foam under compressive loads. However, the early fracture under bending deformation in the previous studies, a detailed analysis or experiment test of metallic open-cell foams under a large plastic bending behavior is missing. In addition, the size effect on the shear modulus and shear strength could be significant in the deformation process when the number of cells through the thickness of the foam is insufficient. Hence, numerical method and Kelvin cell model are implemented in this research to analyze the plastic bending behavior of metallic open-cell foam and to understand the size effect on plastic bending.

2.2 Bending theory

2.2.1 Elastic and plastic bending theory

Euler-Bernoulli beam theory and Timoshenko beam theory are the most well known elastic beam bending theories. The major discovery of Euler-Bernoulli beam theory was by Jacob Bernoulli. Leonhard Euler and Daniel Bernoulli put the theory together to become the classical beam bending theory in 1750. The model assumes the beam's cross-section is always perpendicular to the bending line. As a result, the curvature of a beam is proportional to the bending moment at any point. Euler-Bernoulli beam theory does not include the transverse shear deformation and is only able to describe the beam behavior with a small deflection. Timoshenko beam theory was developed by Stephen Timoshenko in 1921 - 1922 [53, 54]. The shear deformation is considered in Timoshenko beam model, and the rotational effect of the beam makes the model suitable for describing the behavior of short beam, composite sandwich panel, and beam under high frequency excitation.

The first plastic bending theory for non work hardening material was developed by Ludwick based on the assumption similar to the elastic bending theory [55]. Hill followed Ludwick's assumption and developed the plastic bending theory in plan-strain condition [56]. However, Ludwick neglected the transverse shear stress, and the model prediction is less accurate when the bending radius to the sheet thickness ratio is decreased. In the later advanced theories, the transverse shear effect was considered in bending of ideal plastic materials [57, 58]. Hill's work was extended to a hypothetical linear strain-hardening material in pure bending condition by Proksa [59].

In the industrial application of sheet metal forming, elastic and plastic bending theories are used to obtain the relationship between applied force and deformation. Yu and Johnson derived an analytical solution to show the influence of axial force on the elastic-plastic bending and springback of a beam [60]. DeVries and Lauderbaugh established a model for bending bimetallic strip and predicted the punch load and the strip shape. Stelson et al. used an elastic-plastic model to build an adaptive force control model for the press brake bending [61-64].

2.2.2 Sandwich bending theory

The analytical models of sandwich bending were developed after 1940. Plantema [65], Allen [66], and Zenkert [67] have made contributions to different problems in bending and buckling of sandwich plates and struts under in-plane loading condition. These classical bending theories used the following basic assumptions to derive deflection equations: 1. The antiplane condition: There is no transverse flexibility in core materials, and thus the deflections of the upper and lower face sheets are equal to each other. 2. The displacement distribution in the longitudinal direction is linear. With these assumptions, the total displacement could be separated into two parts. The primary deformation is the beam deformation without shear deformation and the secondary deformation is the face sheets bending on its own neutral axis, and the core is subjected to shear deformation [68].

To consider the sandwich panel with a transversely flexible core, the assumptions in the classical bending theory are no longer valid. As a result, the high order sandwich theories were introduced to account for the nonlinear effects on the distortion of the

section plane. Forstig [69-71] investigated the general behavior of sandwich beams with flexible core under concentrated loads and distributed loads, and developed the high order sandwich theory. The proposed sandwich theories could determine the transverse stress at the interface between the face sheets, which is helpful in analyzing the delamination problem of sandwich panels. The high order sandwich theories could also predict the stress under singular conditions.

From the review of sandwich theories, it is found that most of the sandwich panel bending theories assumes small deflections. Under a large plastic deformation, the deformation of sandwich panels is nonlinear, and the deformation behavior should be described by nonlinear differential equations. The existing sandwich theories would not be appropriate for a large deformation, and numerical methods could be applied to solve the complex nonlinear problem.

2.2.3 Failure mode map

The concept of failure mode map for sandwich beams in bending problem was developed by Triantafillou and Gibson in 1987. In the research, equations were developed to describe the load at each possible failure modes for sandwich beams when face sheets and core materials yield plastically [72]. Then, the failure map with the ratio of face sheet thickness to span length versus the core relative density was developed. The plot showed the major failure mode at given load configuration with a various combination of face sheet and foam core. The failure mode map is then used to optimize the design of sandwich beams.

McCormack et al. [73], Chen et al. [74] and Bart-Smith et al. [75] investigated plastic collapse modes for the sandwich panel in three points and four points bending using both experiments and analytical methods. The failure mode maps with the axes of beam dimensional parameters and test parameters were built by using limit load solutions, as shown in Figure 18. The analytical result shows the peak loads and the major failure modes agree well with the experimental observations over failure maps.

The published failure maps were developed for sandwich panels, and sandwich panels are not treated as a bendable material subjected to large plastic deformation. For two layered panels of interest in this research, no failure map has been developed and constructed.

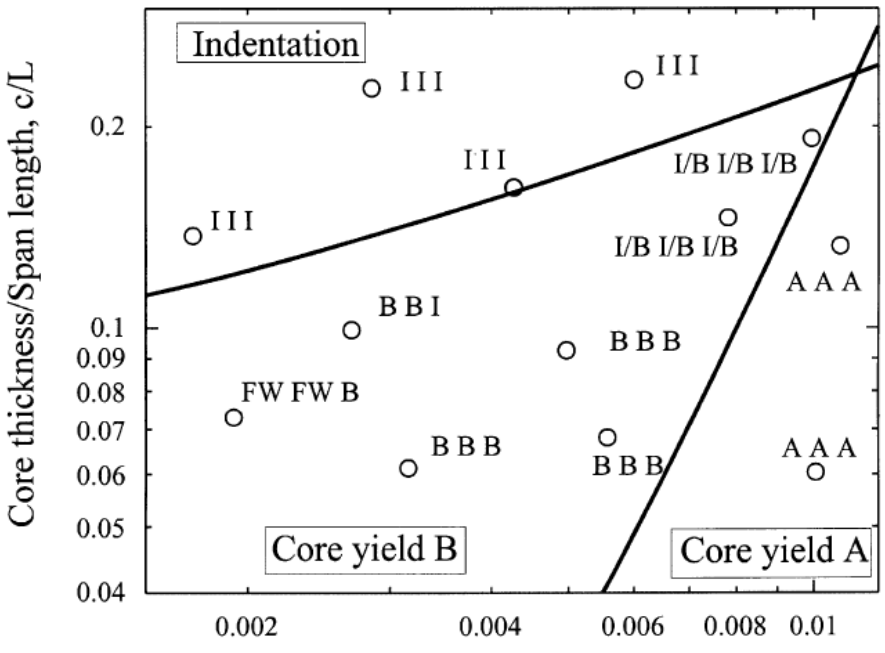

Figure 18 Failure mode map for a sandwich panel with aluminum sheet and aluminum foam core in three points bending test [73].

2.3 Sheet hydroforming

A comprehensive review of sheet hydroforming process was collected by Vollertsen Sheet hydroforming has been widely studied since 1950's [76]. Hill developed an analytical model to describe the deformation of the metal sheet in a bulge test [56]. Chakrabarty et al. improved Hill's work by including hardening coefficient in the model [77]. The effects of work hardening on the thickness and the dome height were investigated. Shang et al. developed a model to predict the influence of the die radius on sheet hydroforming [78-80]. They found that allowing draw-in of the flange can improve the formability of the sheet metal. Hein et al. presented the forming mechanisms at different areas in free hydroforming of a blank [81]. Controlling the blank holder force can improve the formability of the sheet was reported by Shulkin et al. [82]. However, thicker materials, such as sandwich panels and two-layered panels, were not considered as a deformable material in the hydroforming process. The failure mechanism of two layered panels in hydroforming process is not well understood. Hence, this research utilized experiment and finite element analysis to investigate and to describe the failure mechanism of metallic open-cell foam supported sheet panel in hydroforming process.

2.4 Research method

In this research, the major objective is to investigate the formability of the metallic open-cell foam supported sheet metals in both press brake bending process and hydroforming process. To accomplish the objectives, several tasks will be performed.

1. Establish the testing procedure and conduct tests to observe the deformation in the test specimens for both forming processes. Conclude the failure modes and indicate the failure cause.
2. Analyze the experimental results at different foam density, specimen dimensions, and test parameters to understand the effects of material properties and test parameters.
3. Conduct the numerical analysis with proper finite element models to capture the detail failure mechanism and to carry the parametric study in the specimen dimensions, material properties, and test parameters.
4. Construct the failure criterion and the design guideline based on the experimental and numerical results

According to the overall literature review, using sandwich beam theories to obtain the analytical load limit criterion can be challenging due to the large deformation and complex structure of the metallic open-cell foam. Therefore, a proper open-cell foam models based on the observation in the experimental result will be implemented in the finite element analysis and expected to capture the detail failure mechanism.

CHAPTER III

PRESS BRAKE BENDING EXPERIMENT

Press brake bending is a process that a machine punch is used to bend the sheet metal into a predesigned angle above a supporting die. The process is similar to the three points bending test. In this research, the machine punch was modified to have a larger radius to reduce the contact stress for a successful bending of two-layered panels with open-cell foam. The supporting die is replaced by two supporting columns with a fixed radius at the contact area. In this chapter, the experiment setup and results are described, and the discussion of the effects for different test parameters is also presented in the following section.

3.1 Characterization of Duocel Al 6101-T6 open-cell foam

In this study, three different relative densities of ERG Duocel 40 PPI Al 6101-T6 open-cell foam blocks were selected to produce the attached foam in the experiment. The relative density ranges of the foam blocks are 4-6 %, 6-8 % and 10-12 %. To evaluate the relative density precisely, each foam blocks was sliced into 1 inch wide rectangular cuboids by electrical discharge machine, then each small piece was measured and the average value of the blocks was taken as the relative density of the foam block. The obtained average relative densities of the foam blocks are 4.85 %, 7.69 %, and 11.14%. The chemical composition of Duocel Al 6101-T6 open cell foam is listed in Table 1. Table 2 shows the material properties of Duocel 6-8 % Al 6101-T6 open-cell foam given by the supplier ERG.

The previous experimental result already indicated the orientation of the cell has a great influence on the mechanical response of the metallic open-cell foam. In order to examine the cell geometry in the open-cell structure, each relative density block was characterized by 12 mm x 15 mm microscopic images in the rise-transverse plane at 20 different locations. The cell lengths in both rise and transverse direction were measured at least 5 cells in each image, and the value was used to calculate the aspect ratio. Figure 19 showed the measured plot in the microscope image. The average cell lengths in the rise direction are 3.01 mm, 2.82 mm, 3.06 mm, and the aspect ratios are 1.18, 1.24, and 1.25 for 4.85 %, 7.69 %, and 11.14 % Duocel Al 6101-T6 foams, respectively. Table 3 lists the mean values of cell length in the rise and transverse direction and the calculated aspect ratio.

Table 1 Chemical composition of Duocel Al 6101-T6 foam and bulk alloy of the foam raw material [83].

Materials	Cu	Mg	Mn	Si	Fe	Zn	B	Others	Al
Bulk alloy	0.04	0.47	0.02	0.29	0.18	0.01	0.04	—	98.93
Foams	0.03	0.29	0.01	0.25	0.14	0.01	0.03	—	99.22

Table 2 Material properties of Duocel 8% Al 6101-T6 open-cell foam.

Material property of 8% Duocel Al 6101-T6 Foam	
Compresssion Strength	367 psi
Tensile Strength	180 psi
Shear Strength	190 Psi
Modulus of Elasticity (Compression)	15000 psi
Modulus of Elasticity (Tensile)	14600 psi
Shear Modulus	29000 psi

Table 3 Average cell lengths in 4.85 %, 7.69%, and 11.14 % Duocel Al 6101 foam.

Relative Density	Average cell length in rise direction	Average cell length in transverse direction	Aspect ratio
4.85 %	3.011 mm	2.422 mm	1.24
7.69 %	2.822 mm	2.276 mm	1.24
11.14 %	3.061 mm	2.601 mm	1.18

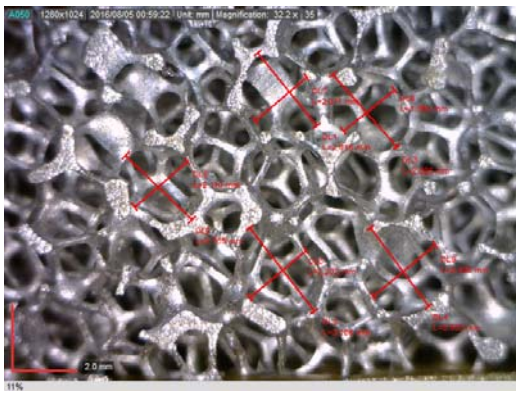

Figure 19 Cell length measurement of 11.14% foam block in the microscope image.

3.2 Experiment setup

3.2.1 Experiment setup

Figure 20 illustrates the experiment setup for the press brake bending process. The specimen was supported by two columns and was pushed down by the center semicircular punch in the rate of 6.35 mm per minute. During the test, the extensometer recorded the deflection in the middle of the bottom sheet, and the punch moved down until the deflection of the bottom sheet reached the desired depth. The desired depth was calculated by bending the panel into 90-degree angle without considering thickness reduction at the given span length (L), as shown in Figure 21.

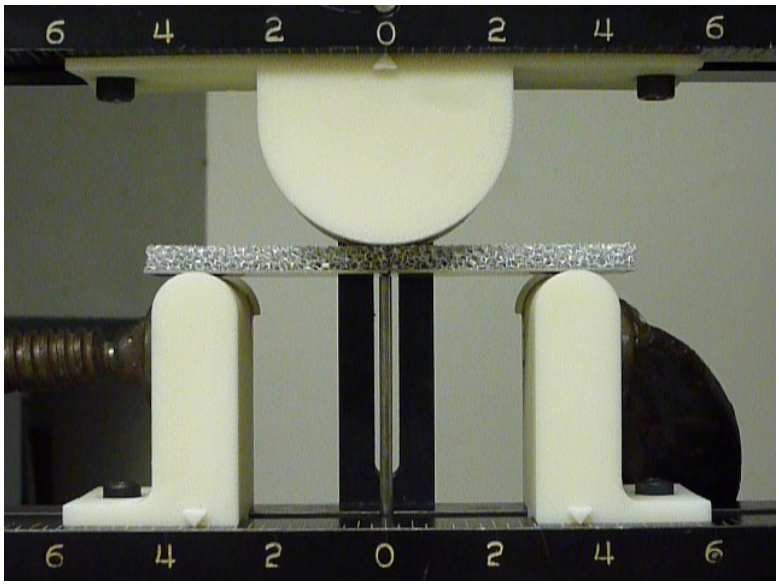

Figure 20 Three points bending experiment setup.

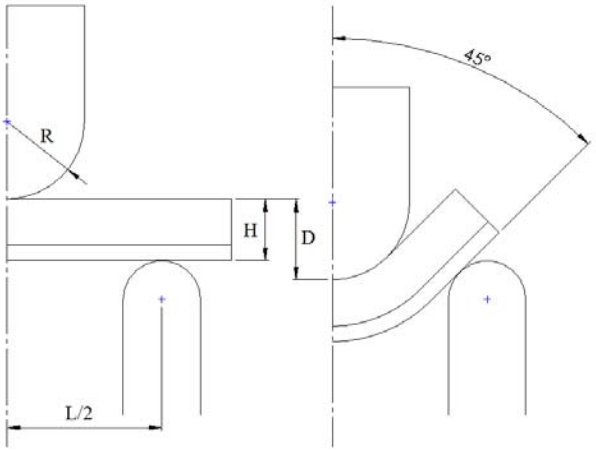

Figure 21 Schematic draw for the calculation of the test punch deflection (D) at specified punch radius (R), specimen thickness (H) and span length (L).

3.2.2 Specimen preparation

The two-layered panel was constructed by one layer of sheet metal and one layer of metallic foam. In this experiment, the face sheet used was aluminum 5052-H32 sheet metal in 0.8 mm thickness, and the metal foam is ERG Duocel aluminum 6101 T6, 40 PPI open-cell metallic foam. The electrical charged machine was applied to cut the foam block and sheet metal into designed dimensions. The width is 25.4 mm and the length is calculated based on the punch radius for both face sheet and foam. During the assembly process, the face sheet was cleaned with acetone first, then was applied a 0.2 mm thickness of Loctite H3151 acrylic adhesive to create the bond between the face sheet and the foam. The two-layered panel was fixed by the clamps for one day to allow the adhesive to cure completely.

3.2.3 Test parameters

The three point bending process was tested with three major test parameters to evaluate the bendability for the metallic open-cell foam supported sheet panel. These three major test parameters are punch radius, foam relative density and foam thickness. For punch radius, there were four different punch radii (R), 5 mm, 10 mm, 20 mm, and 30 mm, tested in the experiment. Each punch radius was tested in a fixed span length (L) between support columns. The length of the span are 50 mm, 60 mm, 80mm, and 90 mm corresponding to the punch radius, 5 mm, 10 mm, 20 mm, and 30 mm respectively. For foam relative density, 4.85%, 7.69%, and 11.14% relative densities of Duocel open-cell metallic foams were tested in the bending process. The relative density of foam was obtained from the averaged relative density of foam blocks after cutting by electrical discharge machine. For the foam thickness, three thicknesses, 6mm, 9mm, and 12mm, were selected for each relative density. For the 7.69% average relative density, an additional set of 15.8 mm thickness specimens was added to observe the thickness effect on the deformation of two-layered panels. Table 4 shows the correspondent punch radius to specimen length and Table 5 demonstrates the calculated punch deflection for the specified test parameters in the experiment.

Table 4 Correspondent punch radius to specimen length.

Punch Radius (mm)	5	10	20	30
Specimen Length (mm)	60	80	98	118

Table 5 Punch deflection (D) for specified test parameters.

Punch Radius (R)	5		10		20		30	
Specimen Thickness (H)	L	D	L	D	L	D	L	D
6.8	50	15.970	60	18.899	80	24.757	90	25.615
9.8		14.727		17.656		23.514		24.372
12.8		13.485		16.414		22.272		23.130
15.8		12.242		15.717		21.029		21.87

Unit: mm

3.3 Experimental result

3.3.1 Punch force to sheet metal deflection curve

Figure 22 presents the punch force to the sheet metal deflection curve in the test set with 9 mm thickness of 7.69 % foam and 10 mm punch radius. As shown in the curve, the punch force has a linear rise in the beginning of the test, and then turns gradually into a less steep rise. If the punch force has an apparently decrease, it means the foam is separated from the sheet metal due to weak adhesive bonding, such as the sample 5 in Figure 22. In the observation, even though the relative density of foams in the same test set has a small difference from one to another, the force-deflection curves are quite close and the variation is in an acceptable range. Hence the repeatability of the experiment is assured. For convenience, the averaged punch force to sheet metal deflection curve is used in the following discussion.

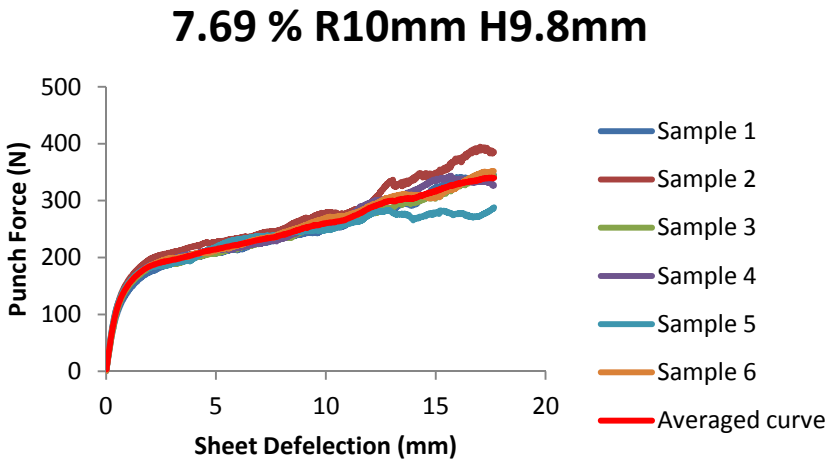

Figure 22 The averaged punch force to sheet metal deflection curve in the test set with 9 mm thickness of 7.69 % foam and 10 mm punch radius.

3.3.2 Deformation modes of two-layered panels

The deformation modes of press brake bending experiments can be discussed in three major categories. These three major deformation modes are curved panel with uniform thickness, foam indentation, and face sheet indentation. Each deformation condition is described as follows:

Curved panel with uniform thickness

Figure 23 shows the foam microstructure in the middle of the specimen before and after the bending process at the side view and the top view. The panel is bent into an arch panel successfully, and there is little change in the panel thickness. The face sheet only changes in its curvature, but the thickness and length do not vary in the bending process. The only significant deformation happened around the top layer of the open-cell foam. The cell structure is compressed in the transverse direction. The deformation is obvious with the increased foam thickness. As expected, the bond from face sheet limit the movement of the open-cell foams at the interface and leads the foam subjected to compressive bending deformation.

Foam indentation

Figure 24 and Figure 25 demonstrate the foam indentation mode in the middle of specimens during the bending process. The punch left a clear punch mark at the contact area with metallic foam and caused the reduction of foam thickness. From the observation, the deformation of struts collapse could be separated into two different behaviors. In the middle line of specimens, the cells were compressed along the

thickness direction, but the length along the longitudinal direction is unchanged. The cells near the punch had larger radial compression deformation than the cells near the face sheet. Besides collapse in the middle line, there are two shear zones appeared at the both edges of the punch contact area. From the observation in experiments, the shear zone happened near the edge of the punch contact area at first. With the increased punch deflection, the shear zone extended and the struts piled up near the punch contact area. Meanwhile, the struts at the top middle span started to collapse and led to a thickness reduction in the specimen.

Therefore, the parameter "thickness ratio" is introduced to characterize the thickness change in the process. The thickness ratio is calculated by using the deformed thickness divided by the original specimen thickness. The thickness ratio to punch deflection curve can depict the thickness status of the specimen during the experiment, as shown in Figure 26. Based on the observation of the curves, the foam indentation always happens in the early stage of the bending process. Here, a 3 % thickness ratio reduction is set to distinguish the foam indentation in the experiment. If the reduction of thickness ratio is greater than 3%, then the specimen is considered to have foam indentation. Table 6 lists the averaged thickness ratio in the final status for all test sets.

Face sheet indentation

The face sheet indentation happened when the foam thickness is over 12 mm in the experiment. The excessive contact force at the support columns left a mark at the sheet and led a non-straight edge in the face sheet, as shown in Figure 27. The face sheet

indentation is inspected after the experiment is completed. The face sheet and foam indentation deformation can happen in a specimen simultaneously.

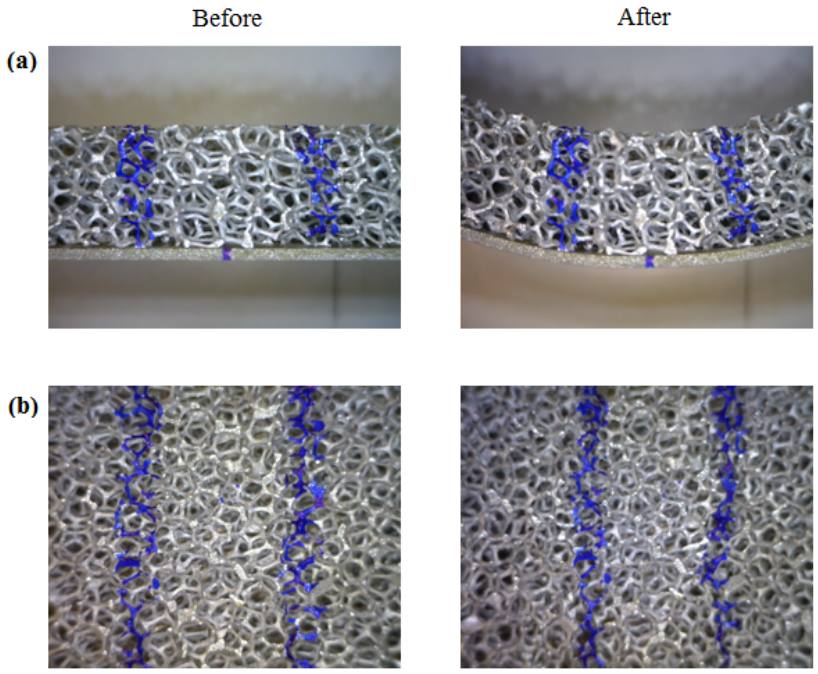

Figure 23 Foam microstructure deformation before and after the bending process, (a) side view, (b) top view.

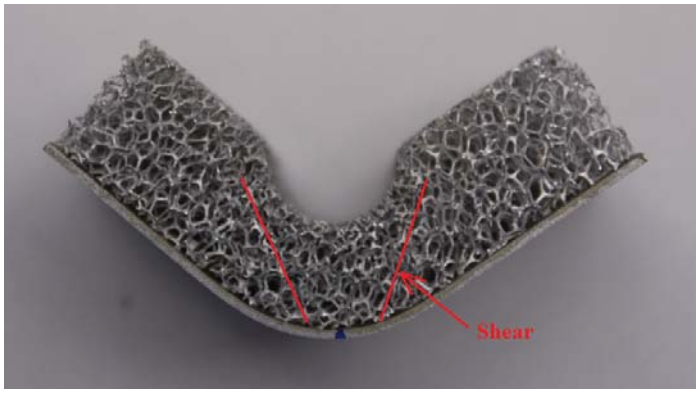

Figure 24 Foam indentation at 4.85%, thickness 12.8mm foam, radius 5 mm test.

Figure 25 Foam indentation at 4.85%, thickness 12.8 mm foam, radius 10 mm test.

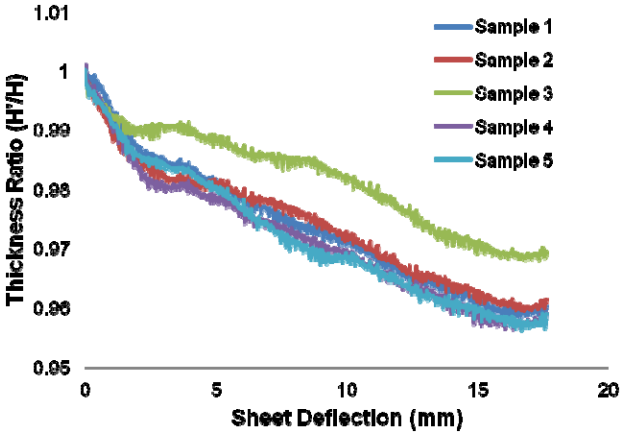

Figure 26 The thickness ratio to punch deflection curve in the test set with 9 mm foam thickness, 7.69% foam and 10 mm punch radius.

Figure 27 Sheet indentation at 7.69%, 15 mm foam thickness, radius 30 mm test.

Table 6 Thickness ratio at the final punch deflection.

Specimen average thickness ratio (H'/H)				
Punch Radius (mm)	Foam thickness (mm)	Foam relative density		
		4.85%	7.69%	11.14%
5	6	0.892	0.954*	0.972
	9	0.835	0.909	0.933
	12	0.741	0.79	0.871*
	15		0.695	
10	6	0.978	0.986	0.995
	9	0.961	0.962	0.975
	12	0.93	0.919*	0.954*
	15		0.873*	
20	6	0.998	1.022	1.009
	9	0.998	0.99	0.994
	12	0.987	0.978	0.992
	15		0.964	
30	6	0.982	0.999	1.012
	9	0.996	0.9963	1.003
	12	0.989	0.987	0.999
	15		0.981	

* Denote the set has less than three effective samples

3.3.3 Deformation modes at given test parameters

As a summary, the deformation modes in 4.85%, 7.69%, and 11.14% relative density foams at given test parameters are collected and summarized in Figure 28. The x-axis is the radius of punch in mm, and the y-axis is the foam thickness, also in mm. From the chart, it can be concluded that the higher relative density foam may have less foam indentation in the thinner foam thickness.

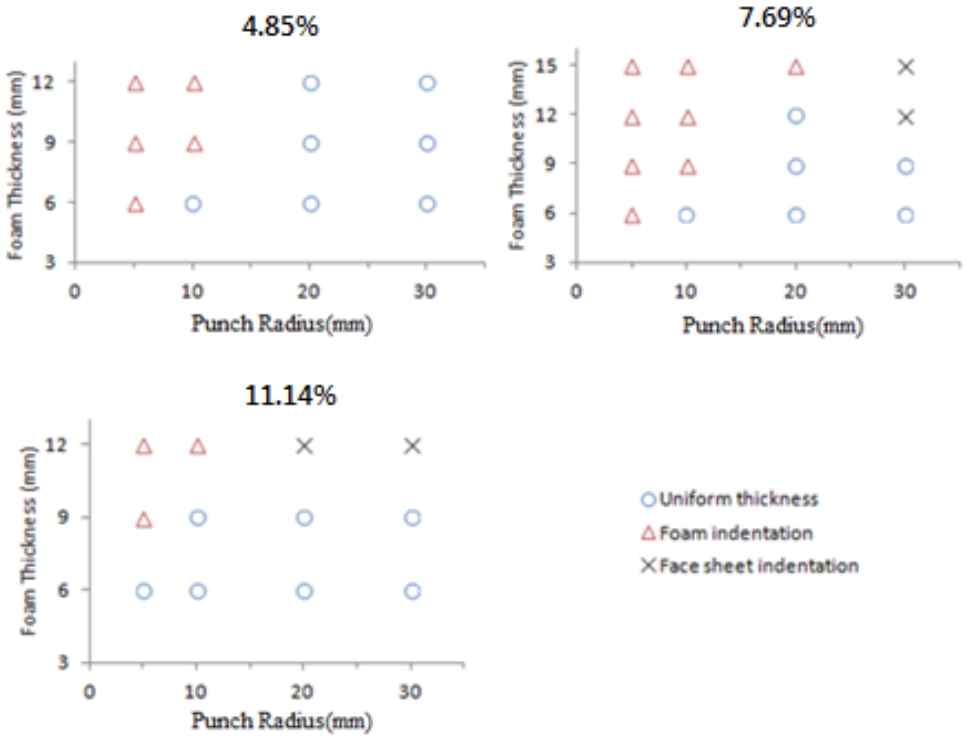

Figure 28 Deformation modes with three relative density foam at different test parameters.

3.3.4 Initial bending stiffness and effective moment of inertia

Since the foam indentation happens in the early stage, the initial bending stiffness of the foam supported panels is an essential property for identifying the occurrence of the foam indentation. To analyze the initial bending stiffness, the punch force to sheet metal deflection curve with sheet metal deflection between 0 to 0.5 mm sheet metal deflection is further examined. Then the linear fit method is applied to the linear portion of the curve to approximate the bending stiffness. Figure 29 to Figure 31 demonstrate the initial bending stiffness at the thickness of the foam and the span length of the supporting die for each relative density foam.

From the observation of the force to sheet metal deflection curve, the very initial bending stiffness of the test is linear and the response of the sheet metal should be elastic. The linear bending stiffness can be expressed mathematically as a function of test parameters from the flexure formula of in three points bending. The initial bending stiffness, K, is the reaction force of the punch, F, divided by the deflection of the sheet metal, δ, which is

$$K = \frac{F_{punch}}{\delta_{sheet\ metal}} = \frac{48(EI)'}{L^3} \tag{3.1}$$

Here, L is the span length and $(EI)'$ is the effective constant of the elastic modulus multiple the moment of inertia of the panel cross-section. In the test, the metallic foam and the sheet panel are both aluminum, and the values of the elastic modulus for both foam and sheet metal are the same. Hence, the elastic module of effective constant of

$(EI)'$ can be extracted as $E_{sheet} \cdot I'$. I' can be treated as the effective moments of inertia of the panel cross-section and the value can be written as

$$I' = \frac{1}{48}\frac{L^3 K}{E_{sheet}} \tag{3.2}$$

Here $E_{sheet} = 69\ GPa$ is applied in equation (3.2) to obtain the effective moments of inertia from the bending stiffness. Figure 29 to Figure 31 plot the effective moments of inertia of the foam supported sheet metal at different test parameters. As shown in the Figure 32, the effective moments of inertia in the sample without indentation is very consistent even in the different span length and the variation of the effective moments of inertia in 80 mm and 90 mm for each set is within 5% to 10%. In the sample with indentation failure, however, the value of effective moments of inertia is 19% to 32% lower than the value of the identical sample tested in the longer span with no indentation. According to the observation, we can conclude the indentation will reduce the bending resistance of the panel in the very beginning of the test when the indentation failure occurs. As a result, the difference of initial bending stiffness is significant between the samples with and without indentation failure and it may be treated as a failure criterion for the press brake bending process. Figure 34 plots the average value of the effective moment of inertia in 80 mm and 90 mm span length for each test, and the average value is a list in Table 7. The data are used to discuss the effects of different test parameters in the next section.

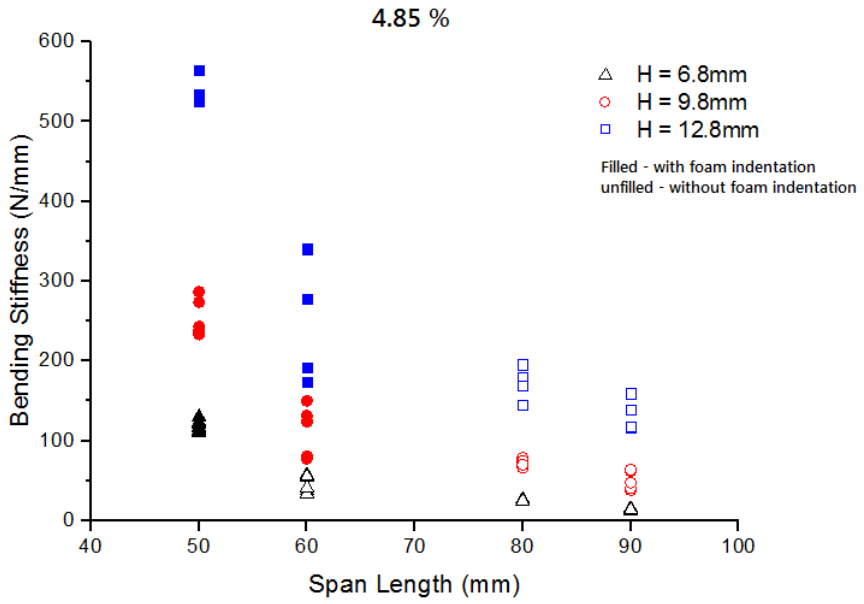

Figure 29 Initial bending stiffness of 4.85 % relative density foam at the given specimen thickness and span length.

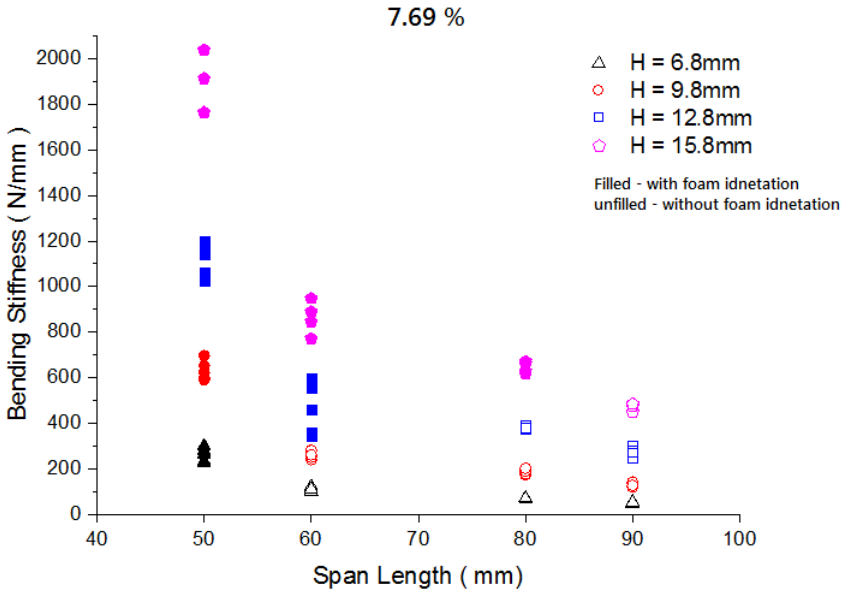

Figure 30 Initial bending stiffness of 7.69 % relative density foam at the given specimen thickness and span length.

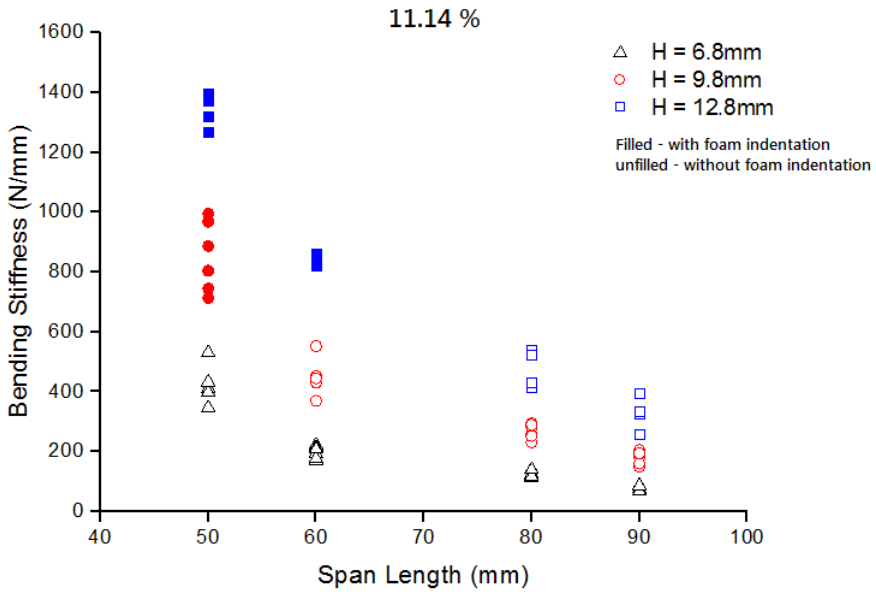

Figure 31 Initial bending stiffness of 11.14 % relative density foam at the given specimen thickness and span length.

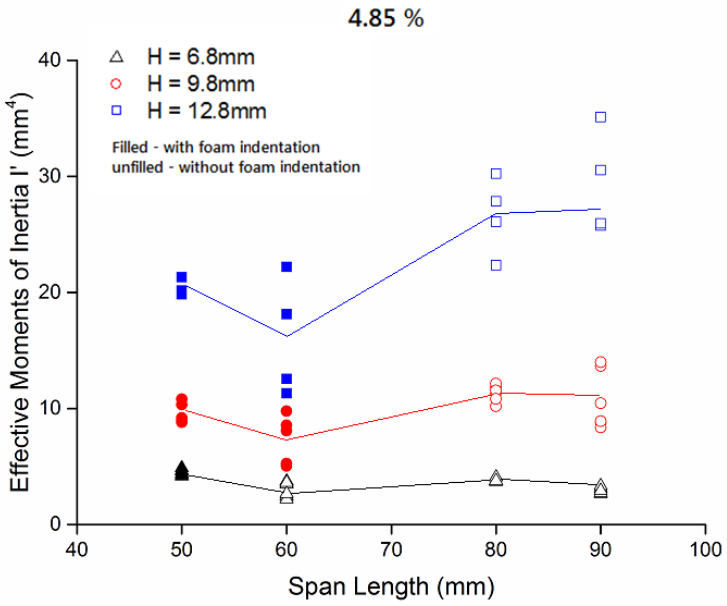

Figure 32 Effective moment of inertia of 4.85 % relative density foam at the given specimen thickness and span length.

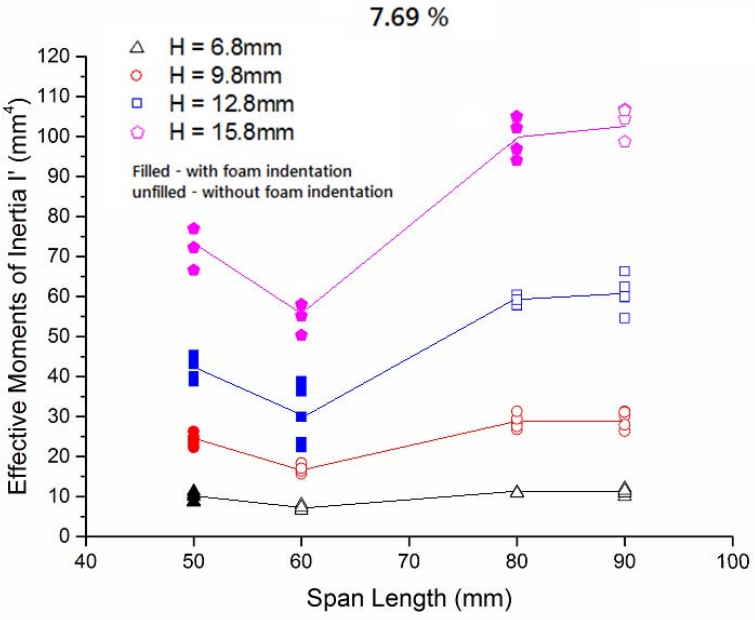

Figure 33 Effective moment of inertia of 7.69 % relative density foam at the given specimen thickness and span length.

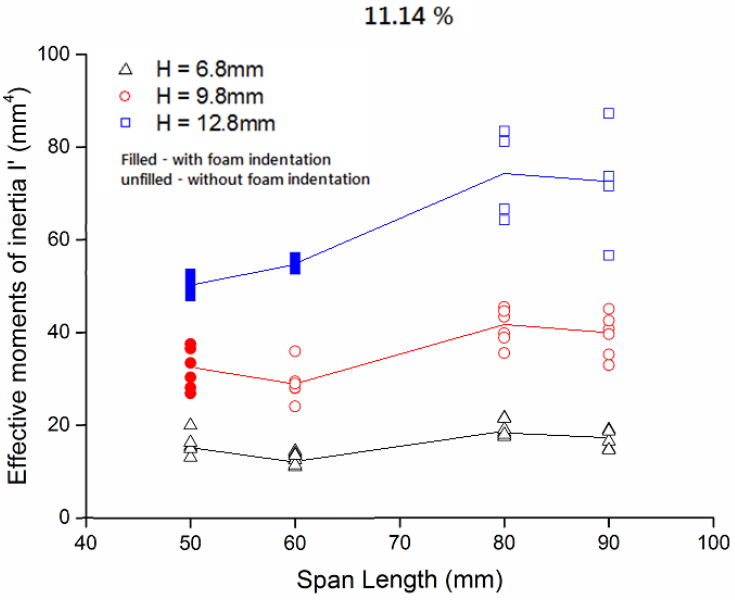

Figure 34 Effective moment of inertia of 11.14 % relative density foam at the given specimen thickness and span length.

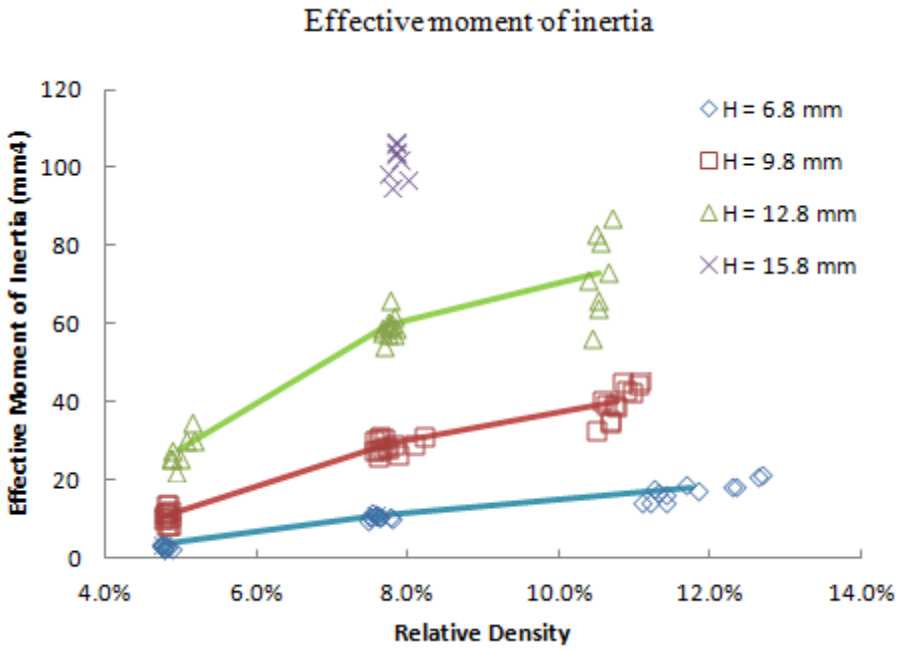

Figure 35 Effective moment of inertia in 80 mm and 90 mm span length via different relative density and sample thickness.

Table 7 The average value of the effective moment of inertia in 80 mm and 90 mm span length via different relative density and sample thickness.

Effective Moment of Inertia (mm^4)				
Relative density	Sample thickness (mm)			
	6.8	9.8	12.8	15.8
4.85 %	3.40	10.99	27.99	-
7.69 %	11.05	29.43	59.72	101.88
11.14 %	17.86	40.29	73.09	-

3.4 Discussion of experimental results

In this section, the effects of the foam thickness, the relative density of foam and the span length are discussed and summarized.

3.4.1 Effect of foam thickness

The increased thickness will make the panel has a better rigidity and cause a higher initial bending stiffness. Therefore, the punch force to bend the panel for the same sheet metal deflection is raised with the increase of foam thickness at the fixed span length. A larger punch force will lead a great contact stress and may cause the ligaments inside open-cell foam collapse in the middle of the span. Figure 36 and 37 illustrate the punch force to sheet metal deflection curve and the thickness ratio to sheet metal deflection curve in the different thickness experiments with 10 mm punch radius and 7.69% relative density foam As shown in Figure 36, the reduction of thickness ratio apparently increased in a thicker foam, and the foam in 12 and 15 mm thickness have significant changes in thickness ratio. The other test results in the 4.85% and 11.14% relative density also had the same trends in the both of the force to deflection curve and the thickness ratio to the deflection curve.

Compare to the effective moment of inertia in Figure 32, the thicker foam has a larger effective moment of inertia. For instance, the average value of the moment of inertia in 7.69 % relative density foam is 11.05 mm^4, 29.43 mm^4 and 59.72 mm^4 respectively to 6.8 mm, 9.8 mm and 12.8 mm sample thickness.

3.4.2 Effect of relative density

The relative density of foam affects the foam material properties. According to Ashby and Gibson's effective open-cell foam material model, the elastic modulus of foam is proportional to the square of the relative density and the yielding strength is proportional to one and a half power of the relative density. For the same pore size (PPI) open-cell foam, the greater relative density increases the cross-section area in the ligaments, and it also raises the elastic modulus and yielding strength at the same time. As a result, the higher relative density open-cell foam is more difficult to be bending. To compare with Figure 35 to Figure 38, the higher relative density will lead to a larger initial bending stiffness, and it agrees with the physical observation from the foam microstructure. From the view of the effective moments of inertia in Figure 32, the high relative density foam also led a large value of the effective moments of inertia in the panel.

Figure 38 shows the punch force to sheet metal deflection curve and Figure 38 shows the foam thickness ratio to punch deflection curve for 4.85 %, 7.69 %, and 11.14 % relative density in the experiment of 6 mm foam thickness and 10 mm radius. From the plots, the 11.14 % relative density foam had the largest punch force and the smallest reduction of thickness ratio among the three relative density foams under the same sheet metal deflection.

3.4.3 Effect of span length

The observation of the indentation failure in Figure 28 shows the indentation failure tests are on the left-hand side and the tests without the foam indentation are on the right-hand side. Although the test radius at each span length is different, but the initial contact area of the punch is relatively small and it leads the bending stiffness is not strongly affected by the punch radius. In the classic beam bending theory, the bending stiffness is proportional to the cubic of the inverse span length. The bending test results also give the same trend that the value of the initial bending stiffness has a rapid reduction with the increased span length. In the initial bending stiffness plot, a design guideline exists and it will separate the area with the foam indentation area and the area without foam indentation.

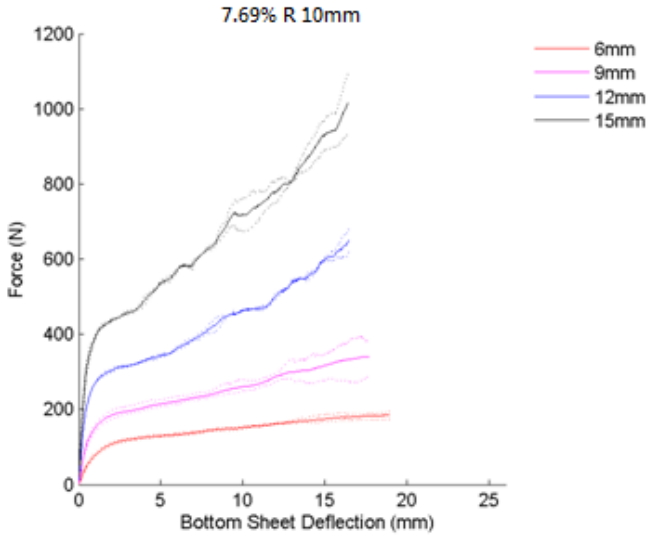

Figure 36 Force to sheet metal deflection curve in 7.69 % density and 5 mm punch radius experiment.

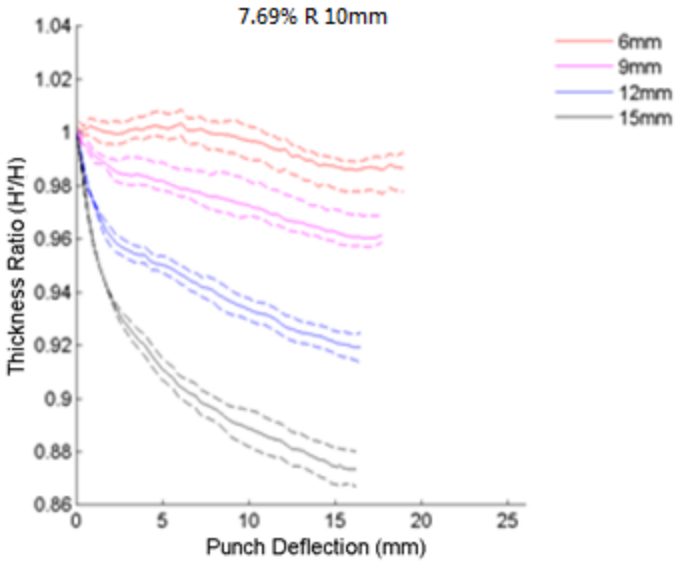

Figure 37 Thickness ratio in 7.69 % density and 5 mm punch radius experiment.

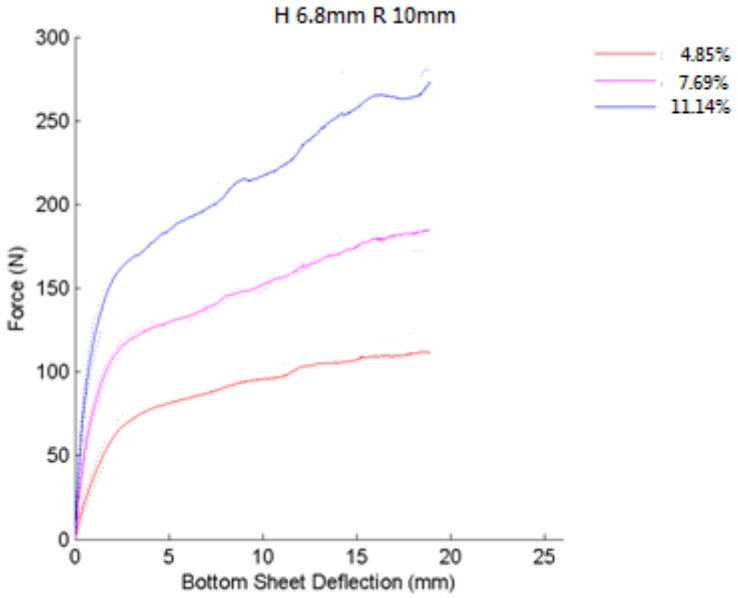

Figure 38 Punch force to deflection curve for each relative density foam in the experiment of 6 mm foam thickness and 10 mm punch radius.

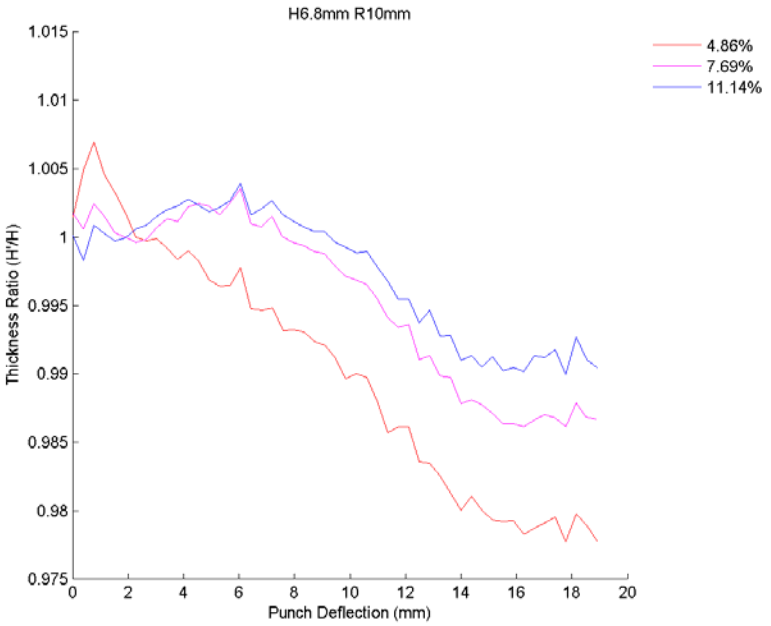

Figure 39 Foam thickness ratio to punch deflection curve for 5%, 8%, and 11% relative density in the experiment of 6 mm foam thickness and 10 mm radius.

3.5 Hoop strain failure criterion

From the observation in the experiment, two shear zones were appeared next to the mid-span in the indentation failure samples. The cell at the top edge of the shear zone had the most severe shear deformation, and it was the initial shear buckling location. As a result, the compressed stress and strain at the top cells would be the key parameters to build the failure criterion for this process. However, to describe the localized stress and strain for random foam ligaments is unrealistic. Therefore, a failure criterion is proposed based on the geometry of a perfect bending condition. A perfect bending condition, as shown in Figure 38, assumed the supported sheet metal would fully confirm the punch curvature without variation in foam and sheet metal thickness. Hence, the deformation behavior of the cross-section is linear in the perfect bending condition, and the bending strain can be described by the location of neutral axis and the bending curvature. From the observation in the experiment, the length change of sheet metal is minimal, and the midplane of sheet metal is able the assumed as the location of the neutral axis. The hoop strain along the cross-section can be written as:

$$\varepsilon_{\theta\theta} = -\frac{Y}{R'} = -\frac{Y}{(R + h + \frac{t}{2})} \tag{3.3}$$

where, $\varepsilon_{\theta\theta}$ is the hoop strain; Y is the location from the neutral axis; R' is the bending radius; R is the punch radius; h is the foam thickness; t is the sheet metal thickness. The proposed failure criterion hypothesis analyzed the hoop strain of the top cell in the perfect bending condition. The criterion assumed the shear zone failure will occur when

the compress hoop strain excess the compress strain limit, ∅. The location of the average hoop strain of the top cell is half of the nominal cell length, L_{cell}, under the top edge. The equation of hoop strain can be rewritten as:

$$\varepsilon_{\theta\theta} = -\frac{h + \frac{t}{2} - \frac{1}{2}L_{cell}}{\left(R + h + \frac{t}{2}\right)} > -\emptyset \tag{3.4}$$

$$h < \frac{1}{1-\emptyset}\left(\emptyset R + \frac{1}{2}L_{cell}\right) - \frac{t}{2} \tag{3.5}$$

The equation (3.5) is the final form of the proposed failure criterion. Figure 40 shows the criterion on the punch radius to foam thickness plot. The slope of the failure criterion is $\frac{\emptyset}{1-\emptyset}$ and the intersection value in the foam thickness axis. is $\frac{1}{2(1-\emptyset)}L_{cell} - \frac{t}{2}$. Here, equation (3.5) was further normalized by the sheet thickness, t, and can be written as,

$$\frac{h}{t} < \frac{1}{1-\emptyset}\left(\emptyset\frac{R}{t} + \frac{1}{2}\frac{L_{cell}}{t}\right) - \frac{1}{2} \tag{3.6}$$

The failure criterion equation (3.6) splits the plane into two regions with indentation and without indentation. For a larger compress strain limit, the slope becomes steeper and the intersection point moves up.

To validate the geometric failure criterion, the geometric parameters of the test set with the same radius were substituted in the equation and a range of the compress strain limit was obtained from the failure transition zone. Here, the nominal cell length was selected as 3 mm. The calculated compress strain limit range in the largest punch radius

which contained both indentation failure and uniform thickness samples are 0.3~0.4, 0.34~0.39, 0.41~0.48 for 4.85 %, 7.69 %, 11.14 % Duocel Al 6101-T6 open-cell foam respectively. The mean value of the upper and lower limit of the range was selected as the compress strain limit in the failure criterion. The average compress strain limit are 0.35, 0.365 and 0.445 for 4.85 %, 7.69%, 11.14 % Duocel foam respectively. Figure 42 expressed to the method to draw the failure criterion in the plot of 7.69 % Duocel foam. Figure 43 and Figure 44 shows the failure criterion in 4.85 % and 11.14 % Duocel foam. From the observation in the plots, the failure criterion successfully predicted the foam indentation failure from the geometry parameters in various relative density Duocel Al 6101-T6 open-cell foam. It is demonstrated that the failure criterion is able to evaluate the geometry parameters of the metallic open-cell foam supported sheet metal in the press brake bending process.

The average compress strain limit also implied that there is shear deformation resistant in the metallic open-cell foam. This observation agrees with the shear strength of ligament in the foam structure. The ligament in the large relative density foam has a larger profile, and the cell structure has a better rigidity to overcome the shear deformation.

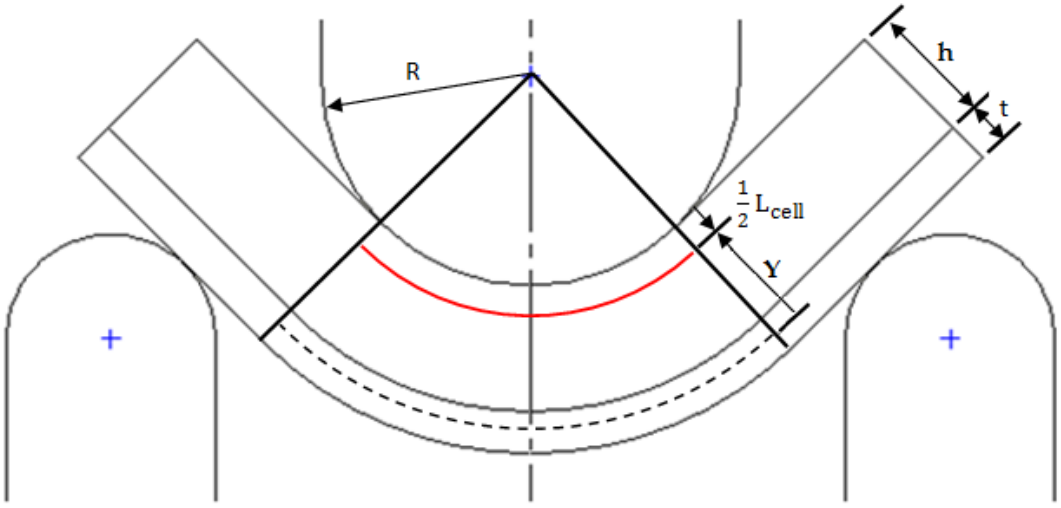

Figure 40 Configuration of the perfect bending condition.

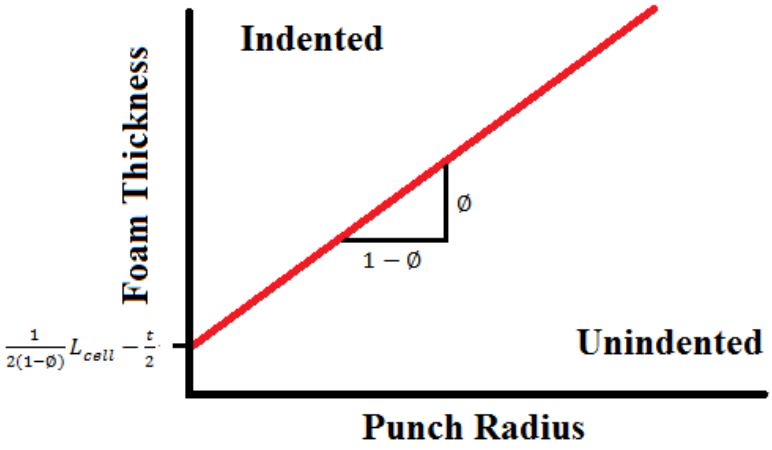

Figure 41 Geometric failure criterion hypothesis of metallic open-cell foam supported sheet panel in the press brake bending process.

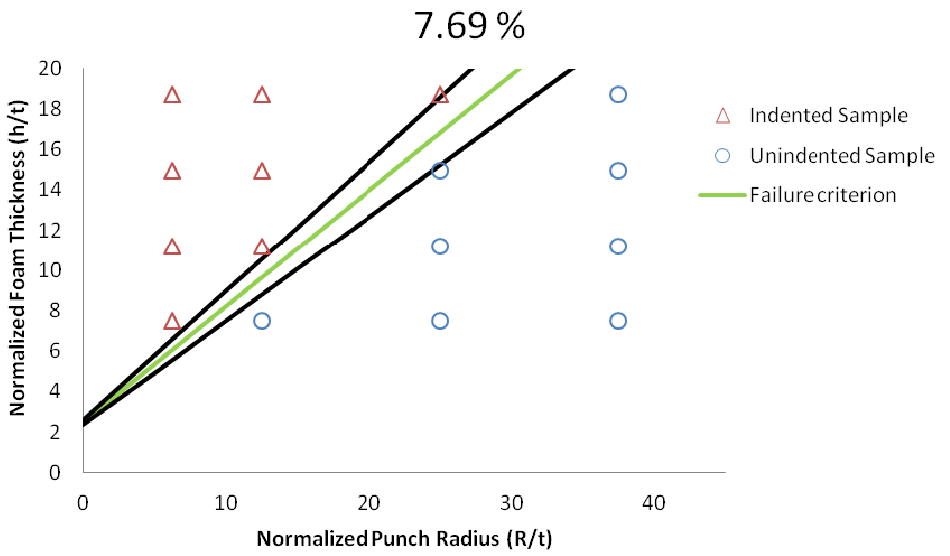

Figure 42 Failure criterion in 7.69 % Duocel Al 6101-T6 open-cell foam.

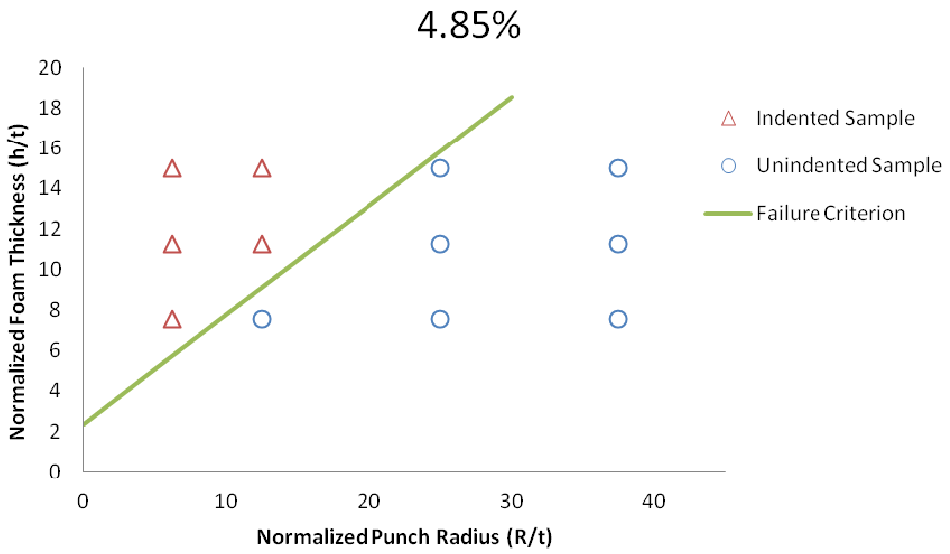

Figure 43 Failure criterion in 4.85 % Duocel Al 6101-T6 open-cell foam.

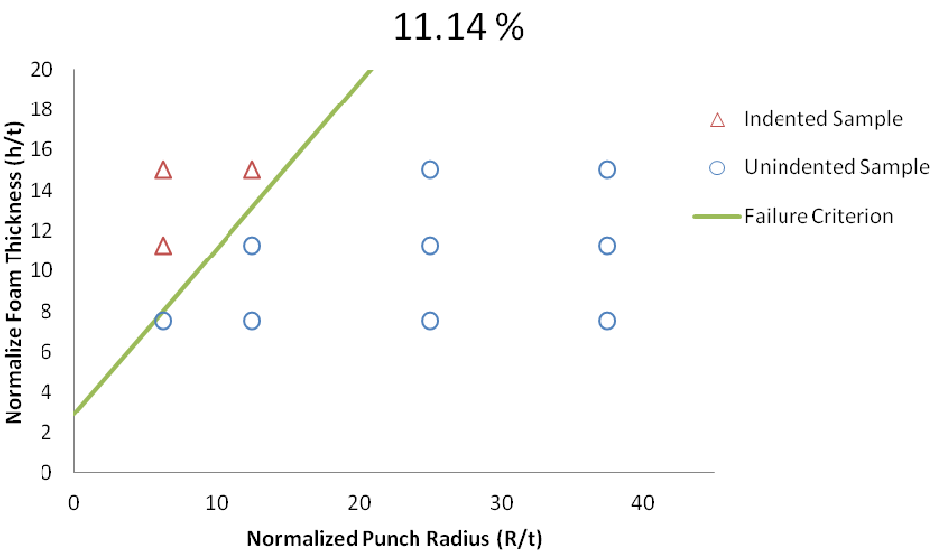

Figure 44 Failure criterion for 11.14 % Duocel Al 6101-T6 open-cell foam.

3.6 Summary and conclusions

The experiments of press brake bending process have successfully proved the idea to deform the metallic open-cell foam supported sheet metal. The results show several successful bending parameters and also indicate there might be a foam indentation failure in the very beginning of the test when the specimen dimensions and test parameters are inappropriately selected. A shear band in the foam microstructure is also observed near the mid-span of the sample. Besides, the indentation failure will damage the structure and lead a reduction in the initial bending stiffness of the panel.

Through observation in the experiment result, the indentation failure can be prevented by choosing a larger punch to span length ratio. From the aspect of the material property, the higher density foam can increase the ligament rigidity and can be bent by a smaller punch radius without indentation failure.

A geometric failure criterion was proposed based on the assumption of the perfect bending condition. By setting the maximum compressive hoop strain, the failure criterion successfully identified the indentation failure in the given specimen dimensions and the punch radius. The value of the maximum hoop strain for three density foams also proved that the higher density foam has a larger capability to be compressed without failure. This finding agrees with the experiments conclusion.

CHAPTER IV

NUMERICAL ANALYSIS OF PRESS BRAKE BENDING PROCESS

The experimental results had shown the feasibility of bending metallic foam supported sheet metal with press brake bending process. A shear band of buckled ligaments was observed in the indented samples before the thickness reduction ratio reaches to 3 %. Due to the complex ligament arrangement in the open-cell foam, the shear band was difficult to measure. Anisotropic Kelvin cell foam model was built using shear deformable beam elements and implemented in the finite element analysis to observe the open-cell foam deformation behavior. Grids were set up to calculate the strain of the top layer cells near the punch during the bending process. Through the observation of strain history at multiple test sets, a shear strain failure criterion was established and compared with the geometric failure criterion introduced in Chapter III.

4.1 Anisotropic Kelvin cell foam model

The structure of Kelvin cell model is consists of 6 squares, and 8 hexagons. The cluster of anisotropic Kelvin cell and the repeated ligament frame were shown in Figure 45. In the plot, l represents the ligament length in the horizontal plane, $tan\,\alpha$ is the height to width ratio in the cell, the 1 direction is along the rise direction; the 2 and 3 directions are along the transverse direction. The unit length in the transverse direction plane, h2, is equal to $2\sqrt{2}l$. For a convenience, anisotropy ratio (λ) is introduced to indicate the anisotropic geometry of Kelvin cell and $\lambda = tan\,\alpha$. Hence, the unit length in the vertical plane, h1, is equal to $\lambda \cdot 2\sqrt{2}l$. In this study, the sliced foam thickness

direction was selected in the rise direction and the thicknesses of blocks were selected as 6 mm, 9 mm, 12 mm and 15 mm. According to the statistical data, the range of the cell length along the rise direction is 2.6~3.4 mm and the mean value are close to 3.0 mm in each relative density foam. As a result, 3.0 mm was selected as the rise direction dimension of the unit cell length. The 6 mm, 9 mm, 12 mm and 15 mm thickness foam are equivalent to 2 cells, 3 cells, 4 cells and 5 cells in the thickness direction respectively.

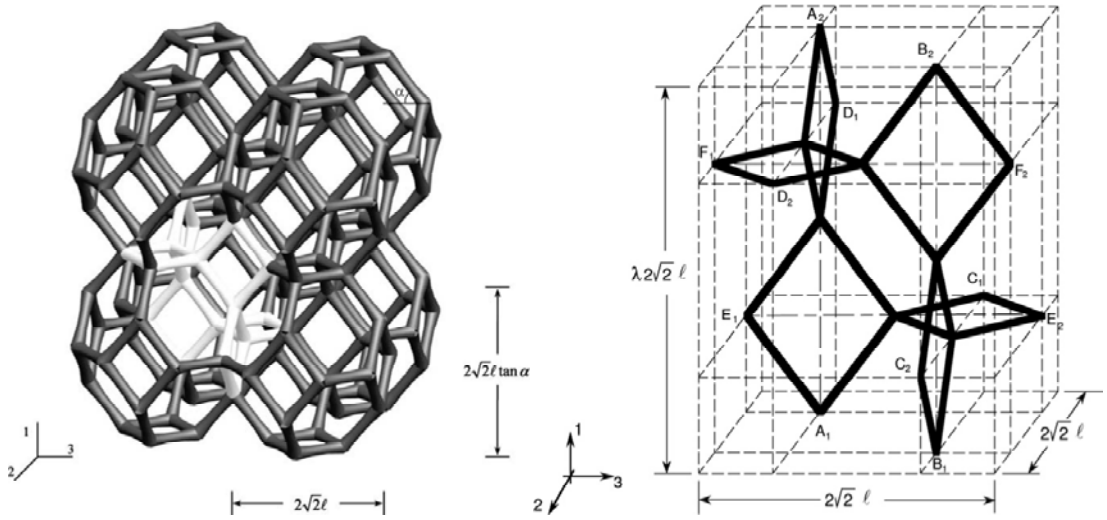

Figure 45 Cluster of Kelvin cells and the repeated ligament frame [38].

The ligaments are assumed to be uniform and share the same cross-section profile. To simplifying the ligament geometry for the three different density foams, a uniform triangular shape, as shown in Figure 46, was given as the ligament cross-section profile in Kelvin cell model. The relative density of model is equal to the volume ratio of the characteristic cell to the unit cell, and can be expressed by the edge length of the profile, *a*, and the ligament length, *l*, as:

$$\frac{\rho^*}{\rho_s} = \frac{V_{ligament}}{V_{cell}} = \frac{\sum_{i=1}^{24} A_i l_i}{h_1 {h_2}^2} \tag{4.1}$$

where A_i is the area of the cross-section area and the value is known as $\sqrt{3}/4 \cdot a^2$. The edge length of the ligament profile was decided from the average value of the relative density in each foam. The correspond profile edge length via various anisotropy ratio is listed in Table 8.

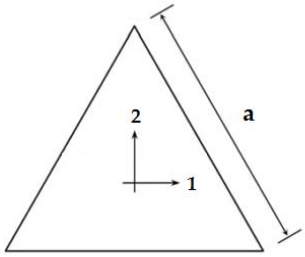

Figure 46 Triangular shape of the ligament cross-section profile.

Table 8 Edge length of the triangular shape via various anisotropy ratios for different foam density.

Edge length of the triangular shape (mm)				
Relative density	λ=1.0	λ=1.1	λ=1.2	λ=1.3
4.85%	0.346	0.324	0.305	0.288
7.69%	0.434	0.407	0.383	0.362
11.14%	0.522	0.49	0.461	0.436

4.2 Modeling of open-cell foam supported sheet metal

In the model of open-cell foam supported sheet panel, the sheet was constructed by cubic elements and the open-cell foam was built by anisotropy Kelvin cell foam model using beam elements. It is assumed that there is no separation between the open-cell foam and the sheet metal, hence two type elements were bonded by a tie constraint at the interface. From the observation of the experimental samples, the width change of metallic foam supported sheet panel in the indentation sample was insignificant after the bending. As a result, the bending of open-cell foam supported sheet metal was simplified as a plane-strain problem in the numerical analysis. Hence, a single layer of Kelvin cell foam model was implemented to simulate the foam behavior. The width of sheet metal has followed the width of the Kelvin cell. To achieve plane-strain condition, a proper periodical boundary constraint was applied at the correspondent nodes at the beam and cubic elements. Due to the symmetrical bending geometry, the model was further reduced into a half model with the symmetry boundary condition at the symmetry plane to increase the computational efficiency. Here the ligament arrangement of the unit Kelvin cell is modified to present the full Kelvin cell geometry at the side view. Figure 47 shows the finite element model, and Figure 48 shows the setup of the press brake bending simulation. The detail geometry parameters of the model are listed in Table 9.

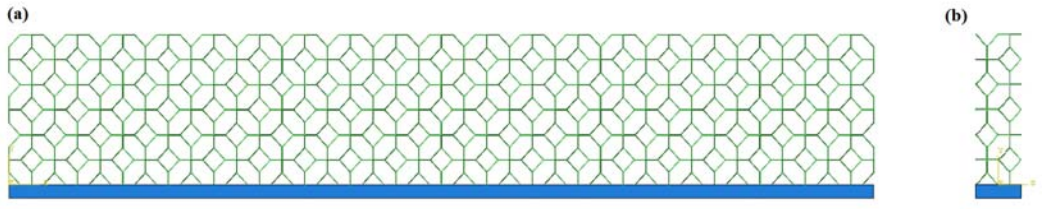

Figure 47 Hybrid model with Kelvin cell beam model, (a) Front view, (b) Side view.

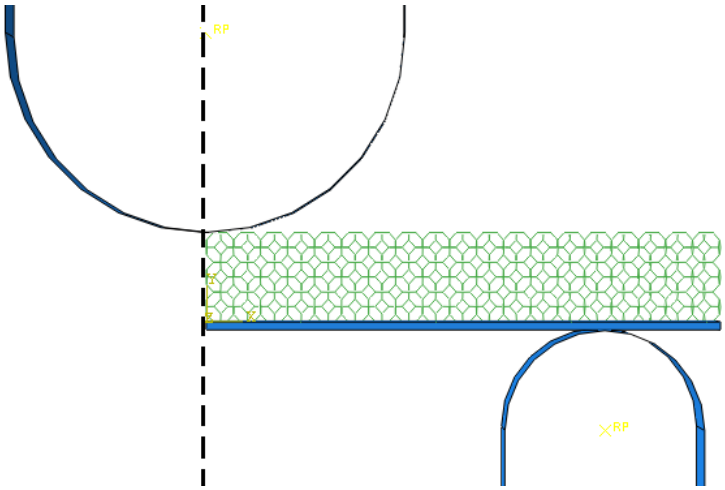

Figure 48 Model setup for the press brake bending analysis.

Table 9 Geometry parameters of the hybrid model.

Geometry dimensions	Value
Sheet metal thickness	0.8 mm
Foam thickness	6, 9, 12, 15 mm
Rise direction cell length	3mm
Rise driection cell numbers	2, 3, 4, 5
Anisotropy ratio	1 - 1.3
Punch radius (R1)	5 - 30 mm
Support Column radius (R2)	10 mm
Support column distance (L)	50 - 90 mm

4.2.1 Discretization

Each ligament of Kelvin cell was discretized and modeled by 6 quadratic beam elements, B32, in nonlinear finite element code ABAQUS. B32 is a shear deformable element, which includes the strain energy due to to the transverse shear in the governing equation. The mesh sensitivity of the beam element numbers was performed by 4, 6 and 8 elements in the test parameters which will induce the ligament shear in the experiment. The behavior of the ligament can be efficiently and correctly performed by 6 beam elements. The ligaments were assign specified orientations to show the nonhomogeneous geometry in the Kelvin cell model. The specified orientation led the Kelvin cell model has a close shape with the actual foam microstructure. The sheet was discretized by C3D8R brick elements, and the sheet thickness direction was assigned 5 elements to accurately model the sheet bending behavior.

4.2.2 Periodical boundary condition

In order to achieve the plane-strain assumption in the hybrid model, a periodic boundary condition was applied on the opposite bounding face of characteristic Kelvin cell and sheet metal. The periodic boundary condition prescribed a relationship in the displacement and rotation degree of freedom at the corresponding nodes. The prescribed degree of freedom relationship in each mating node set is described as following:

$$u_{i1} - u_{i2} = u_{i1}^{ref} - u_{i2}^{ref} \qquad i = 1, 2, 3 \tag{4.2}$$

$$\theta_{i1} - \theta_{i2} = 0 \qquad i = 1, 2, 3 \tag{4.3}$$

where i is the *i-th* degree of freedom; j is the node number in the mating node set; u_{ij} and θ_{ij} are the *i-th* displacement and rotation degree of freedom in the mating nodes set; u_{ij}^{ref} is the *i-th* displacement degree of freedom in the reference nodes set. Here, the original locations of the mating nodes set were selected as the reference nodes set. Because of the plane-strain condition, there is only a non-zero value in the width direction for the relative distance of the mating nodes set. Combined with anisotropy ratio, the value of the displacement periodic boundary condition is $2\sqrt{2}\,l$ in the width direction, and the value in the thickness and length directions are both zero.

4.2.3 Material properties

In the simulation, materials properties of Al 5052-H32 and Al 6101-T6 were assigned in the cubic element and beam element respectively. The behavior of Al 5052-H32 and Al 6101-T6 were modeled as elastic-plastic materials. For Al 5052-H32 material, ten test samples were cut from the sheet metal used in the experiment and material properties was obtained from the uniaxial tensile test. Here, the Ramberg-Osgood equation was applied to express the nonlinear stress-strain relationship in the test data. The equation of Ramberg-Osgood stress-strain (σ-ε) relationship is given by:

$$\varepsilon = \frac{\sigma}{E} + \alpha\frac{\sigma}{E}\left(\frac{\sigma}{\sigma_0}\right)^{n-1} \tag{4.4}$$

where $E\ and\ \sigma_0$ are elastic modulus and yield stress; n, α are the fit parameters. For Al 6061-T6 material, the Ramberg-Osgood parameters of the Al 6101-T6 base material in

Jang's research of crushable aluminum open-cell foam [30]. Table 10 listed the material property parameters of Al 5052-H32 and Al 6101-T6 in the numerical analysis.

Table 10 Material properties of Al 5052-H32 and Al 6061-T6.

Material	Young's Modulus (E)	Yielding Strength (σ_0)	n	α
Al 6101-T6	69 GPa	195 MPa	48	0.707
Al 5052-H32	67.74 GPa	163 MPa	11	0.831

4.2.4 Ligament contact

The previous research and experiments conducted in the present work have shown the initially localized buckling ligaments will lead the later collapse of cells in the compress test. From the experiment observation, the local cell buckling behavior would stop when the buckled ligaments contact one another. Then the collapse behavior is transmitted to the adjacent cells. As a result, to correctly arrest the ligament contact behavior is essential to perform a correct crush behavior in the Kelvin cell model. Gong has introduced a nonlinear spring in the Kelvin cell structure to model the ligament contact behavior at the corner nodes in the compressed direction [34]. Here, the same approach to add a nonlinear spring in the corner nodes in the transverse direction is adopted. The configuration of the spring is shown in Figure 49. The nonlinear spring is modeled by the spring element, SPRINGA, in ABAQUS. The spring force depends on the distance between the two connected nodes. Corresponding to the real force response

in the buckling element, the spring was activated only when the compress distant, δ, excess the threshold value. The nonlinear spring force is given by,

$$F = \begin{cases} 0 & ,\delta < d1 \\ k1(\delta - d1) & ,d1 < \delta < d2 \\ k1(d2 - d1) + k2(\delta - d2) & ,d2 < \delta \end{cases} \tag{4.5}$$

where $d1$ is the threshold distance to activate the spring; $d2$ is the final contact distance; $k1$ and $k2$ are the spring constants. The spring force to compress distance curve in the nonlinear spring is shown in Figure 50.

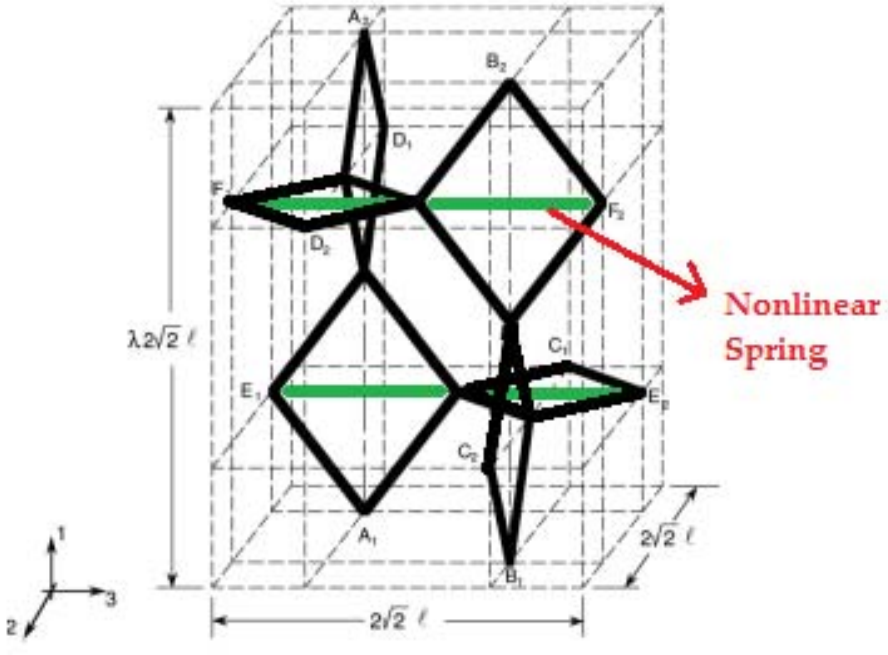

Figure 49 Configuration of the nonlinear spring in Kelvin cell model. Adapted from reference [38] with permission.

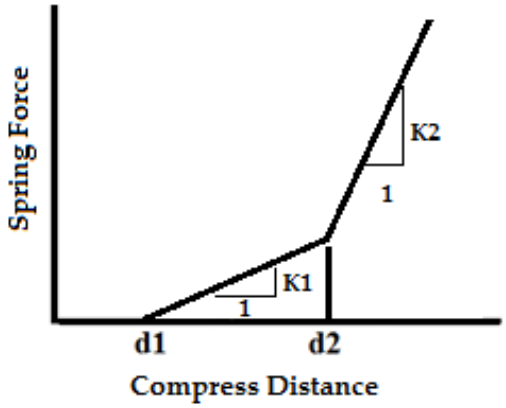

Figure 50 Force response of nonlinear spring element.

4.2.5 Strain calculation

In order to trace the strain of the Kelvin cell, the displacements at 4 nodes in the Kelvin cell were used to calculate the hoop strain and the shear strain. The hoop strain is obtained from the length change between the node 1 and node 2. The shear strain is calculated by the angle change of the two connected lines. Figure 51 shows the select nodes for calculating the hoop strain and shear strain.

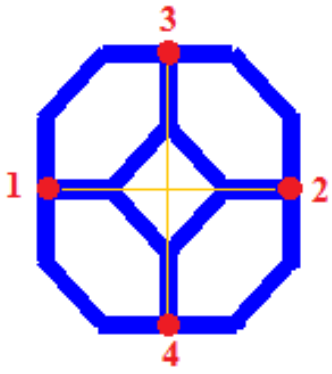

Figure 51 Specified nodes for the strain calculation in Kelvin cell.

4.3 Finite element simulation and results

The simulation of the press brake bending was analyzed by the nonlinear FEA code ABAQUS. Two sets of simulation were carried on for the specific purposes. The first simulation was designed to investigate the effect of the anisotropy ratio of Kelvin unit cell in the bending process. The simulation was conducted in ABAQUS Standard analysis. The span length was set at 60 mm and 80 mm, and the punch displacement was assigned 2.5 mm. The value of the aspect ratio of Kelvin cell was chosen as 1.0, 1.1, 1.2 and 1.3. During the simulation, the initial bending stiffness of the panel was calculated and compared with the experimental result. The anisotropy ratio which led to the best matched initial bending stiffness in the force-deflection curve for each relative density foam is selected for the second simulation to further investigate the large deformation response.

The second simulation was designed to investigate the strain history of Kelvin cell during the bending process, and the punch moves down until the panel bent to 90-degree in the simulation. During the bending process, the ligaments are expected to be under large deformation and may have lots of contacts. Hence the second simulation was conducted as the quasi-static problem in ABAQUS Explicit. Here, the time-scaling technique is applied to reduce the simulation time period to 10 seconds. The coefficients of the nonlinear spring were calibrated from the comparison of the simulation result and the experimental data at the 20 mm and 10 mm punch radius for a 9 mm thickness foam. After the calibration of the spring constants, the hybrid model was tested around the

geometric failure line for each foam thickness. The strain of the top layer cells was monitored and examined.

4.3.1 Bending response for various anisotropy ratio

At the very beginning of the bending process for a successful bending case, the ligament and sheet metal are still in the elastic behavior, and a linear force to the deflection response is expected. In order to accommodate the different sheet width for different anisotropy ratio in the hybrid model, the punch force response was divided by the width of the unit cell to achieve a normalized comparison value in the future discussion. The normalized punch force to the sheet deflection response for various anisotropy ratio for each density is shown in Figure 52. The past research has shown the increasing anisotropy ratio of Kelvin cell will reduce the elastic modulus in the transverse direction, which is the major material property to evaluate the bending stiffness. As a result, the increased value in the punch force and the initial bending stiffness can be observed at the large anisotropy ratio. The simulated normalized punch to sheet deflection curve at the initial bending for 4.85 %, 7.69 % and 11.14 % Duocel open-cell foam are matched with the experiment curve in the anisotropy ratio of 1.3, 1.1, and 1.3 respectively.

4.3.2 Spring constant calibration

The observation in the research of aluminum foam compress response has indicated the force response will become increasingly stiffer when the average strain reaches about 45 %, and the cells will collapse when the average strain reaches about 55 %[30].

In the uniaxial compress test, d_2 is the most significant parameter which is the gap to activate the stiffer spring coefficient, k2. Gong and Kyriakides have suggested the value of $d_2 = 0.792l$ would provide the best match with the experimental data [34].

The coefficients of the nonlinear spring were calibrated in the full simulation at 20 mm punch radius, 9 mm thickness foam, and 80 mm span length for each relative density. The normalized force to the deflection curve in the simulation was compared with the experimental data. Due to the dynamic response in ABAQUS explicit, the simulation curve fluctuated and the local regression method was implemented to smooth the data. Here, the calibrated spring coefficients are transferred to related the unit length

$$d_1 = \varphi_1 \frac{h_2}{2} \tag{4.6}$$

$$d_2 = \varphi_2 \frac{h_2}{2} \tag{4.7}$$

where φ_1 and φ_2 are the compress ratio of the unit Kelvin cell. The calibrated coefficients for each relative density foam are listed in Table 11. For the bending problem, the initial contact ratio, d_1, has the major effect on the curve. A larger value of d_1 will lead a larger force prediction when the nonlinear spring is activated. As shown in Figure 53, the hybrid model with the nonlinear spring can be calibrated to achieve a good agreement with the experimental result.

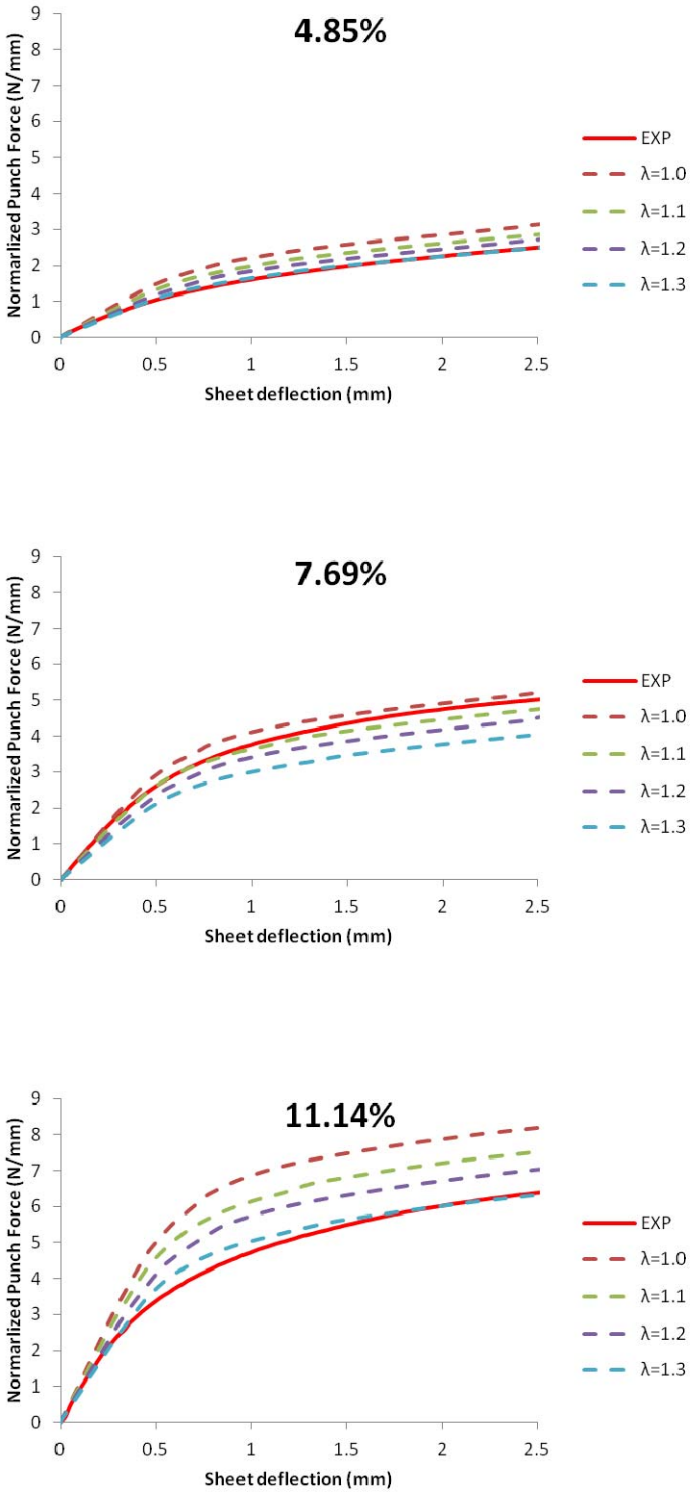

Figure 52 Normalized punch force to sheet deflection response via anisotropy ratio.

Table 11 Calibrated nonlinear spring coefficients.

Relative Density	$h_2/2$ (mm)	φ_1	φ_2	K_1 (N/mm)	K_2 (N/mm)
4.85%	1.154	0.2	0.55	15	50
7.69%	1.364	0.2	0.55	20	100
11.14%	1.154	0.2	0.55	40	200

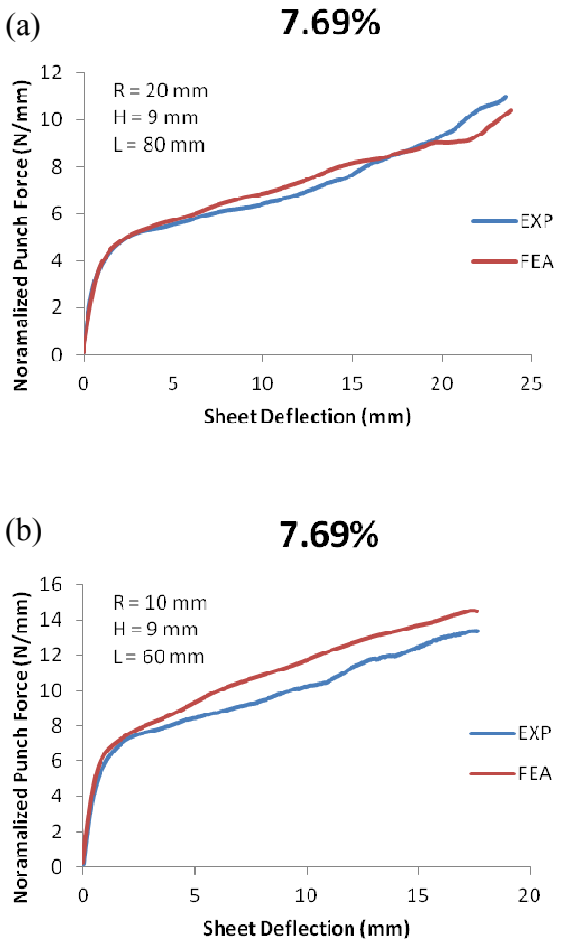

Figure 53 Prediction in punch force to sheet deflection curve of 7.69 % aluminum open-cell foam, (a) Uniform thickness case, (b) Indentation case.

4.3.3 Deformation response of Kelvin cell beam model

The bending deformation of Kelvin cell was observed in multiple simulations, and the deformation can be described into three stages: (1) Initial bending, (2) Spring activate, (3) Ligament buckling. For the simulation of bending without indentation failure, the deformation of Kelvin cell only experienced the first two stages. For the simulation resulted in the indentation failure, the deformation of Kelvin cells went through all three stages. The deformation plot for each stage is shown in Figure 54 and the detail of each stage is described below:

Initial bending

At the initial bending stage, the major deformation of Kelvin cell is the hoop compression of the diamond window in the vertical plane, as shown in Figure 54.(a). The initial and also the most significant deformation happened at the second cell in the top layer cells. In the linear region of the punch force to sheet deflection curve, the deformation of the Kelvin is .not obvious. A significant change in the deformation was observed after the punch force left the linear region.

Spring activate

After the first stage ended, the nonlinear spring is activated to model the resistant of the ligament contact and entered the second stage, as shown in Figure 54.(b). In the second stage, the activated spring will trigger a significant deformation on the nearby cells. As a result, Kelvin cells are observed consequent hoop compression propagation from the mid-span to the end of the panel when the punch displacement is increased.

Ligament buckling

During the second stage, the ligament buckling in the horizontal window at the top layer cells may happen at the top layer cells, as shown in Figure 54.(c). Once the horizontal window experiences the buckling deformation, the next Kelvin cell will undergo a significantly shear deformation and cause the following cells collapse. The location of the buckling window depends on the punch radius, the foam thickness, and the support span length. For the indentation simulation in a smaller punch radius, the location of the buckling ligament window is close to the mid-span.

To illustrate the deformation of Kelvin cell, two simulation results in successful bending and indentation failure for 9 mm thickness 7.69 % open-cell foam are discussed below. The strain of the five cells at the top layer cells are monitored and recorded. The strain calculation nodes and the location of the cells are shown in Figure 55.

For the simulation result in successful bending, the punch radius is 20 mm, and the span length is 80 mm. Figure 56 to Figure 58 illustrated the deformation plot, the hoop strain history and the shear strain history plots for the monitored cells. As shown in the deformation plot, the normal and shear strain is growing with the increased sheet deflection, then keep a stable value during the bending process. Compared with the other cells, the strain in cell 1 and cell 2 have a small value, which is supported by the experiments observation that the deformation of cell 1 and cell 2 are not obvious. The other cells were experienced in a consistent hoop strain and shear strain. The stabilized hoop strain is 0.3, and the stabilized shear strain is 0.07. Due to the insignificant deformation in cell 1 and cell 2, the other cells have to compensate the deformation and

result to a small shear strain value and the slight rotation in the vertical window. But the small shear strain didn't change the cell geometry, and the edge of the cell is still pointed to the radius center of the punch, as shown in Figure 56.

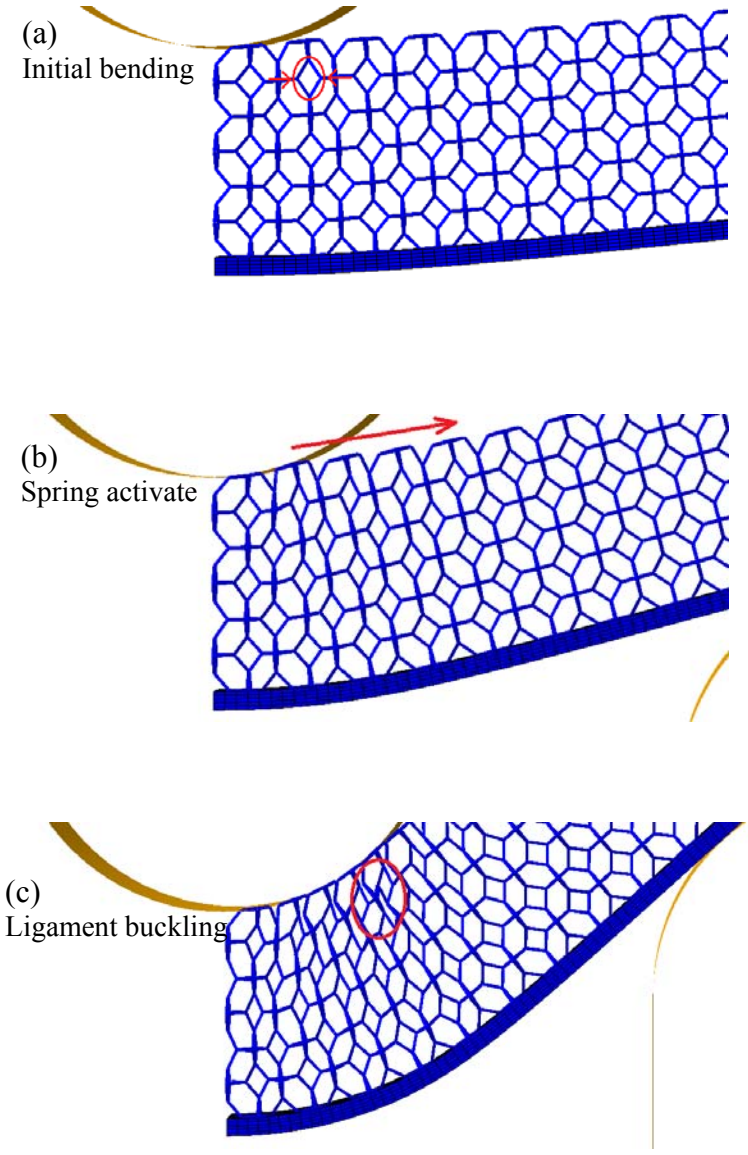

Figure 54 Deformation response of Kelvin cell beam model.

For the simulation result in indentation failure, the punch radius is 10 mm, and the span length is 60 mm. Figure 59 to Figure 61 illustrated the deformation plot, the hoop strain history and the shear strain history for the monitored cells. The cells in the indentation simulation go through a large deformation compared to the successful bending simulation. In the deformation plot, as shown in Figure 59, it can be indicated that the cell 5 experienced a severe distortion. From the strain plots, the cells stable hoop strain is near 0.37, and the stable shear strain is above 0.12. The hoop strain and shear strain of the distorted cell 5 keep growing up with the increased sheet deflection.

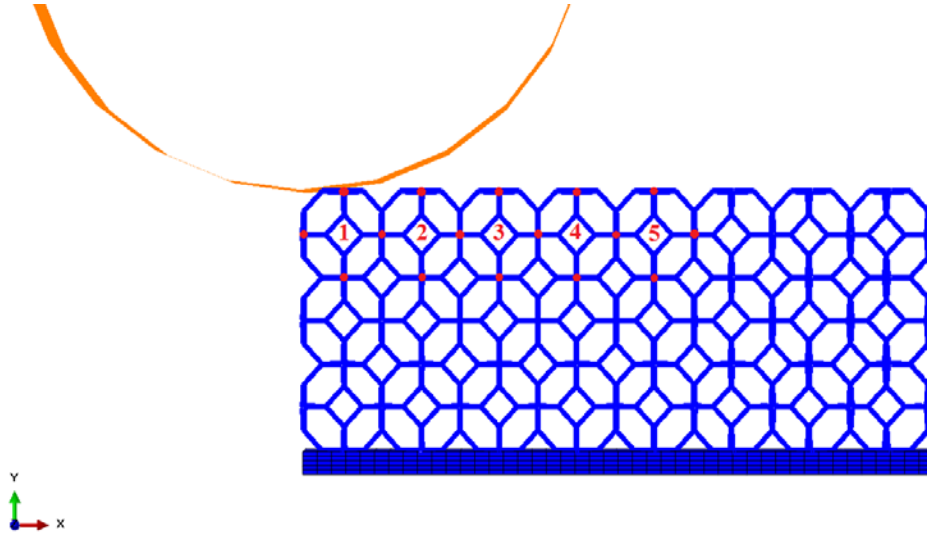

Figure 55 The location of the nodes and the monitored cells for 9 mm thickness 7.69% foam simulation.

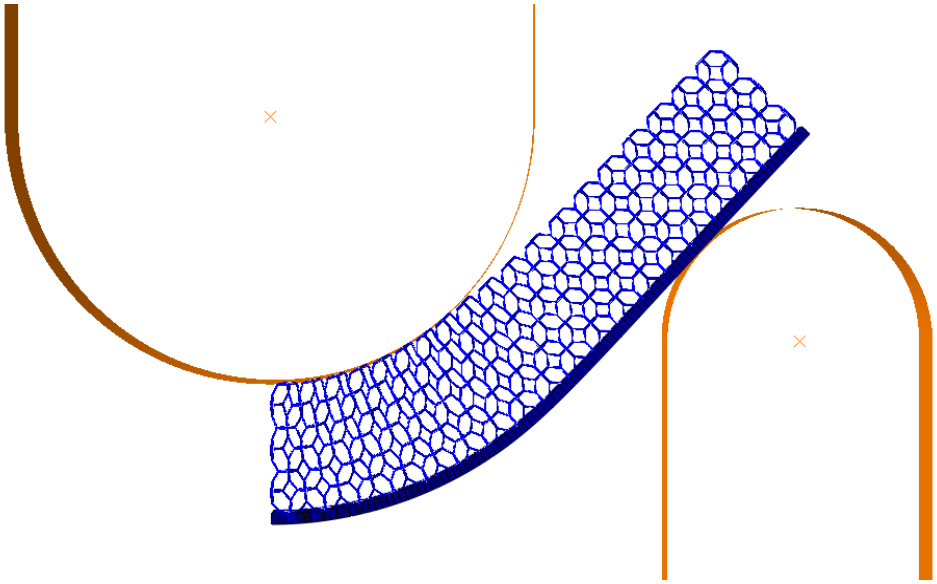

Figure 56 Deformation plot of a uniform thickness bending for 9 mm thickness 7.69% open-cell foam at 20 mm punch radius and 80 mm span length.

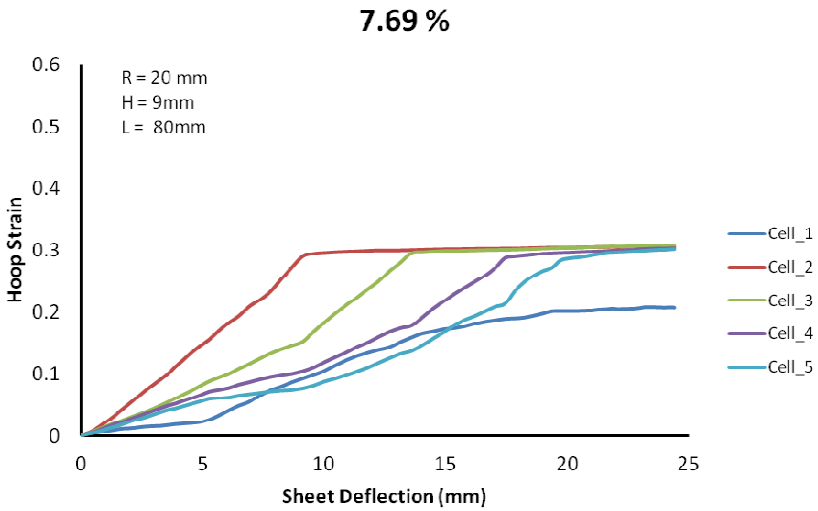

Figure 57 Hoop strain history plot of a uniform thickness bending for 9 mm thickness 7.69% open-cell foam at 20 mm punch radius and 80 mm span length.

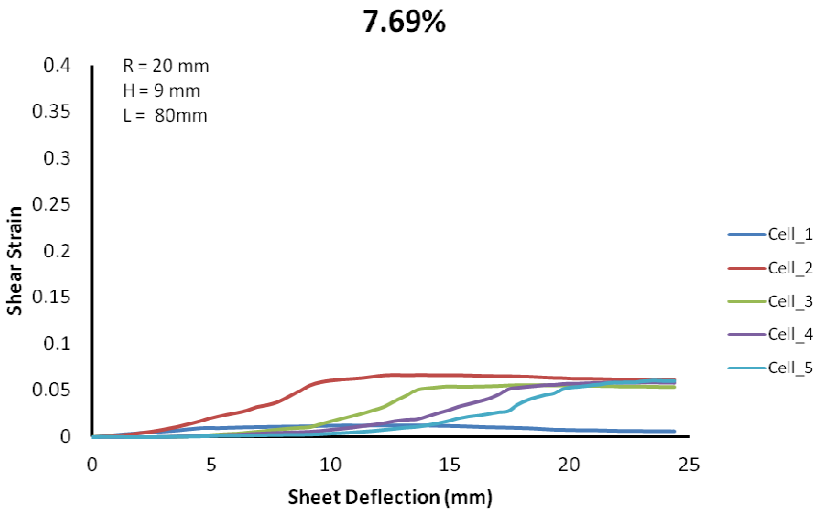

Figure 58 Shear strain history plot of a uniform thickness bending for 9 mm thickness 7.69% open-cell foam at 20 mm punch radius and 80 mm span length.

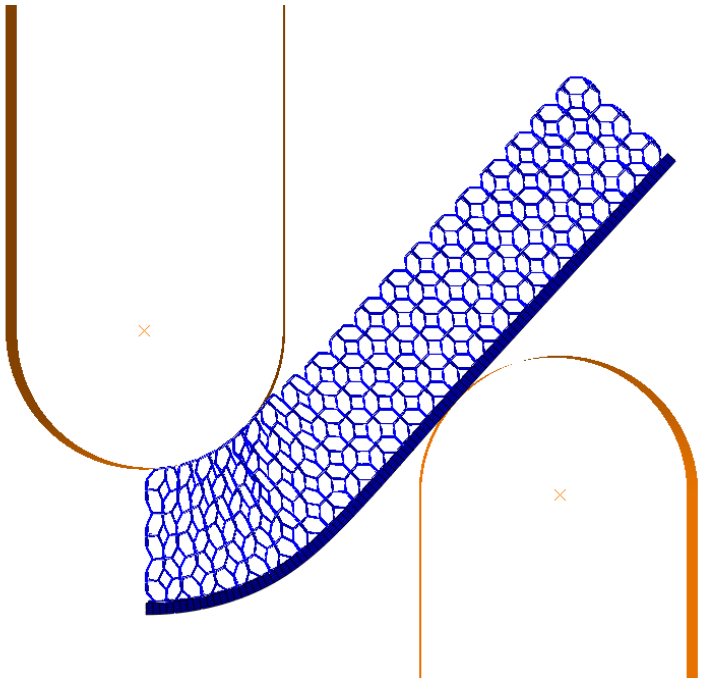

Figure 59 Deformation plot of an indentation failure bending simulation for 9 mm thickness 7.69% open-cell foam at 10 mm punch radius and 60 mm span length.

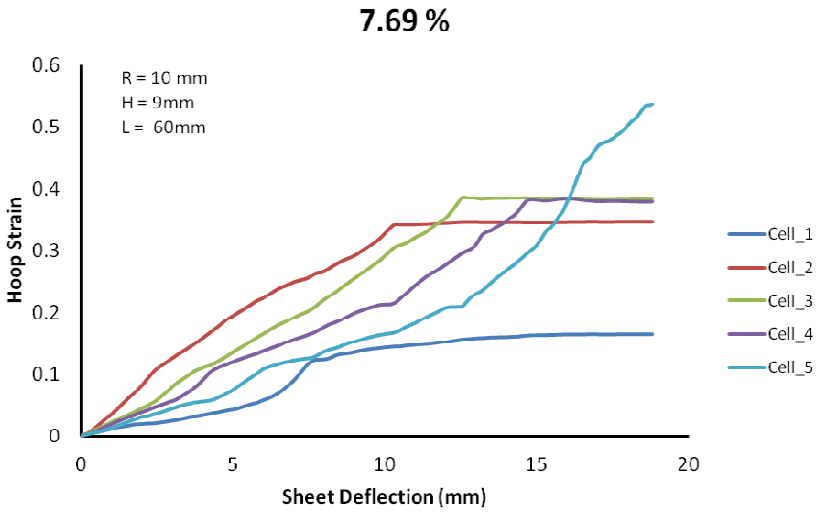

Figure 60 Hoop strain history plot of an indentation failure bending simulation for 9 mm thickness 7.69% open-cell foam at 10 mm punch radius and 60 mm span length.

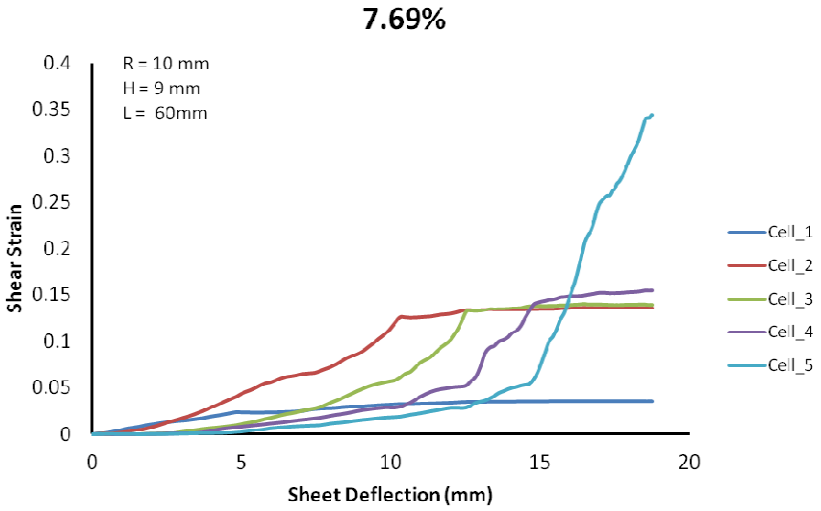

Figure 61 Shear strain history plot of an indentation failure bending simulation for 9 mm thickness 7.69% open-cell foam at 10 mm punch radius and 60 mm span length.

4.3.5 Indentation failure prediction

Compared the strain history of the two simulation results, the value of the stable shear strain has a significant difference. The stable shear strain in indentation simulation could be as twice as that in the successful bending simulation. Hence, a shear strain failure criterion can be defined to identify the indentation failure in the finite element analysis. The failure criterion claims that the indentation happens in the Kelvin cell when the shear strain excesses the set value. Multiple indentation simulation results supported the shear strain value in 0.12 gives the best prediction of the indentation failure in the Kelvin, cell model. Here, several simulations were conducted to identify the indentation failure near the hoop strain failure criterion at 6 mm, 9 mm, 12 mm, and 15 mm foam thickness for each foam. The span length was modified with the same change ratio in the punch radius. The results are compared with the hoop strain failure criterion and listed in Figure 62. As shown in the plot, the indentation prediction by Kelvin cell model is very close to the prediction by the hoop strain failure criterion at 9 mm, 12 mm, and 15 mm thickness foam. For 6 mm foam thickness, however, the shear strain didn't various a lot for all three density foam because the insufficient cell numbers in the thickness direction.

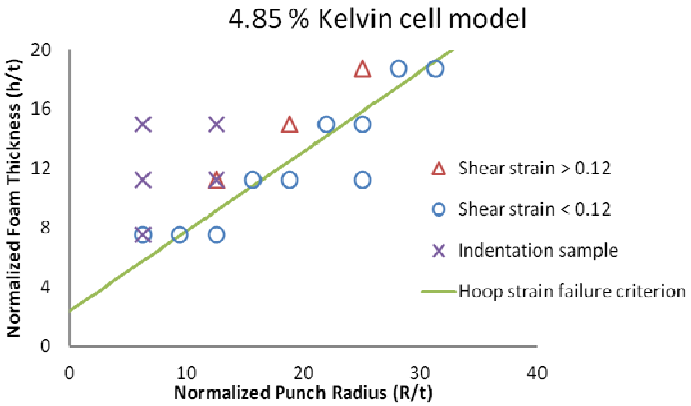

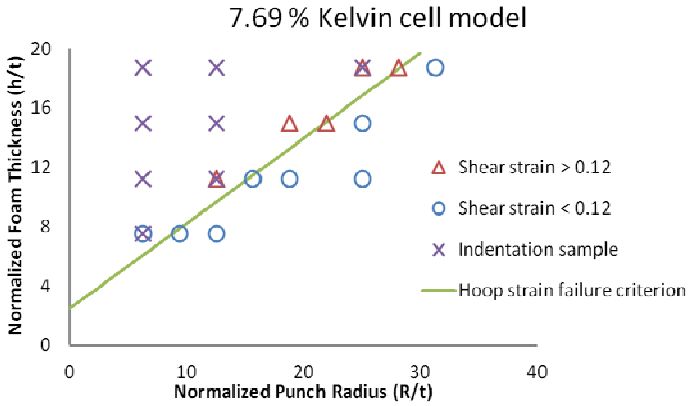

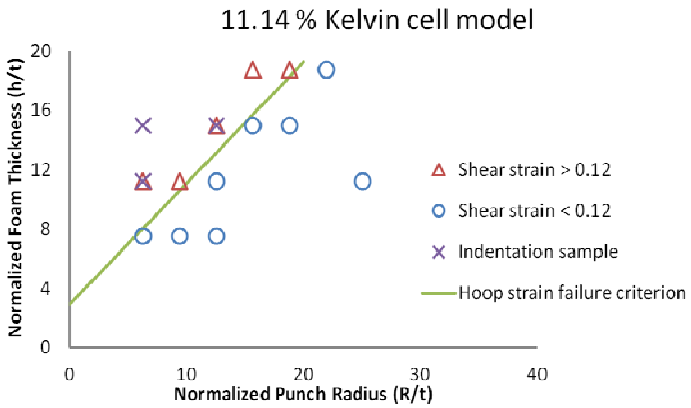

Figure 62 Failure prediction by 0.12 shear strain in the hybrid finite element model via different relative density.

4.4 Summary and conclusions

In this chapter, a hybrid finite element model with anisotropy Kelvin cell was constructed to analyze the response of open-cell foam supported sheet metal in the press brake bending process. The most significant findings are concluding as below:

- With the calibration in the anisotropy ratio of Kelvin cell and the nonlinear spring coefficients, the model has a good prediction in the punch force to sheet deflection curve within the acceptable engineering tolerance range. The model deformation also shows the similar shear failure at the top layer cells with the foam thickness and test parameters at the indentation failure experiment.
- The primary failure mechanism of Kelvin cell in the press brake bending is the ligament buckling in the horizontal window at the top layer cells. The buckling ligament will cause the next cell undergo a significant shear deformation and lead the following cell collapse.
- The history strain observation in both indentation and successful bending simulation shows the normal and shear strain will reach a stabilized value during the bending process. The indentation simulation will give a higher stabilized shear strain value and show a sudden increase value when the cell collapse. With setting a limit shear strain value at 0.12, the indentation prediction in Kelvin cell model gives a good agreement with the hoop strain failure criterion.

CHAPTER V

HYDROFORMING PROCESS[1]

In this chapter, the feasibility of using sheet hydroforming technique to deform two-layered and sandwich panels is demonstrated by experiments and numerical simulation. The process is similar to the bulge forming test [84] that is used to test the biaxial formability of sheet metals. In the experiment, the porous open-cell metallic foam was attached to the sheet metal to form a two-layered panel. As needed, an additional bottom face sheet can be attached to the other side of the metallic foam to make a sandwich panel. With different specimens and deformation conditions in the experiment, various failure modes were observed. The experimental failure modes can also be explained from the results of the finite element simulation, and a better understanding of the failure mechanism of two-layered panels in the hydroforming experiment is achieved.

5.1 Hydroforming experiment

Figure 63 depicted the process of a sandwich panel hydroforming experiment in the axial symmetric diagram. During the hydroforming process, the upper face sheet was first clamped, and the hydraulic fluid can fill the sealed chamber and directly apply pressure over the upper face sheet to deform. Then the upper face sheet was pushed into a bulge deformation with continuously increased pressure, and the core material and the

[1] Part of this chapter is reprinted with permission from "Failure Analysis of Hydroforming of Sandwich Panels," by Wang, J., and Yang, C.-K. *Journal of Manufacturing Processes* 15, 256-262.

bottom face sheet was also be bulged into the upper die cavity due to the adhesive bonding of the upper face sheet.

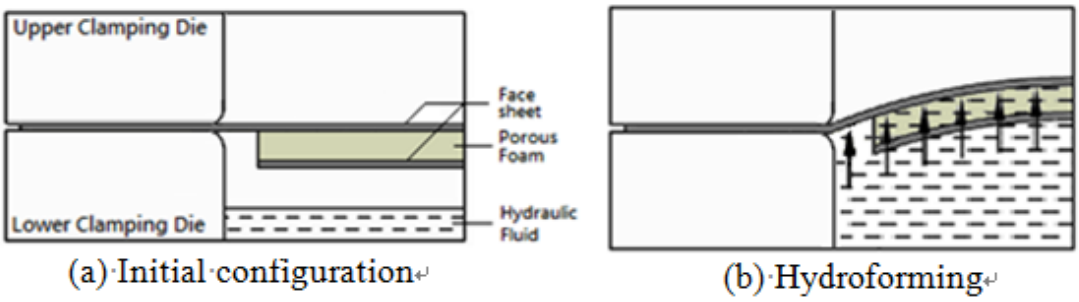

Figure 63 Axial-symmetric schematic diagram of hydroforming experiment process.

5.1.1 Specimen preparation

To produce shaped panels, two-layered and sandwich blanks with metallic open-cell foam core are used in this hydroforming experiment. Aluminum 5052-H32 sheet metal was selected as face sheets and the Duocel aluminum 6101-T6 open-cell foam in 8% relative density was selected as the core materials. Both sheet metal and metallic foam were cut into circular disks by the electrical discharge machining (EDM) processed. The upper face sheet was cut into a larger diameter to fit the die shoulder in apparatus. Metallic open-cell foam core and lower face sheet were cut into a smaller diameter to fit the die cavity. After the face sheet and foam core were cut by the EDM, the face sheet, and the foam disk was attached together by flushed by a thin layer of adhesive. Since two-layered and sandwich panels are subjected to a stretch forming, the flexibility adhesive was selected. Similarly to the procedure to produce the two-layered blanks, the

sandwich attached another face sheet on the other side of the foam disk. This additional face sheet has the same diameter with the foam disk.

5.1.2 Experiment apparatus and setup

There were two apparatuses to test the hydroforming experiment. The first apparatus is the hydraulic press in Michigan State University (MSU), and the other apparatus is the hydroforming bulge machine in Texas A&M University, which was built later. The apparatus in MSU is a close die press, which concealed the deflection of the panel, and it was not able to provide the pressure history during the experiment. In order to get an advanced test data in the future research, a hydroforming bulge machine was designed and manufactured based on Dr. Koc's prototype of warm hydraulic bulge system [86]. Figure 64 shows the schematic diagram of the hydraulic bulge machine. The capacity of the hydraulic bulge machine allows the hydroforming experiment reaches a maximum pressure at 35 MPa and a maximum dome height at 10 mm. During the test, the hydraulic pressure, the dome height and the pneumatic pressure will be recorded and saved from the data acquisition device.

The experiment setup in both two apparatuses uses the same steps to deform the panel. The steps are described as following, (1) fill the lower chamber with hydraulic oil; (2) place the specimen in the center of the die and close the die set, (3) pump the hydraulic oil to deform the panel. During the experiment, the hydraulic pressure was slowly increased, and the bulge forming process was stopped at a preset pressure or when a sharp pressure drop was detected. The specimen was then inspected for any failure.

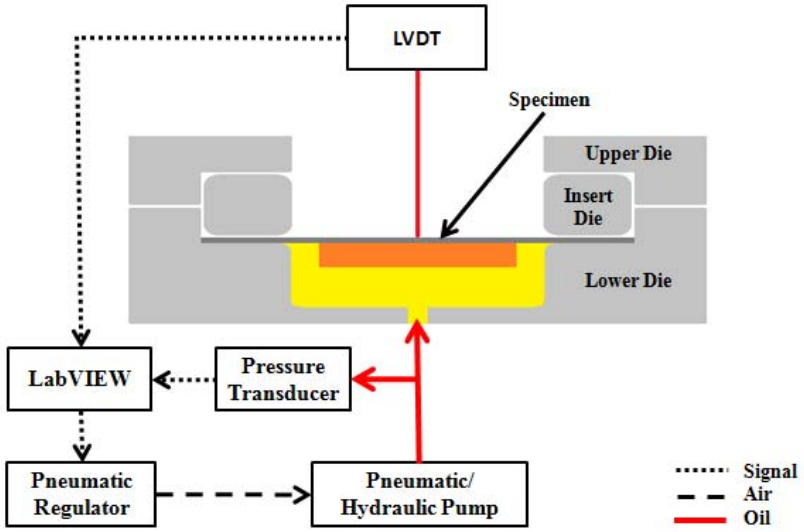

Figure 64 Schematic diagram of hydroforming bulge machine.

5.1.3 Experimental results

From the experiments in MSU, the bulge deformation of sandwich panels is very limited. The two-layered panels, on the other hand, can be deformed into a deeper dome shape. Since the fluid can flow into the porous open-cell foam, no foam damage (collapsing of foam core) was observed in foam disk. The major failures in forming the two-layered and sandwich panels can be classified into three categories.

The first mode of failure is top face sheet fracture. It can be detected from a sudden pressure drop. The fracture location can be at the radius of the clamping die or at the area near the edge of the foam blank, as shown in Figure 65. As the top face sheet

was stretched over a hard corner (the die radius or the edge of the foam), the deformation was localized and the fracture occurred.

The second failure mode was observed is the delamination between the face sheet and foam blank in both two-layered and sandwich panels, and it occurred frequently in sandwich panels. It was found that delamination can take place between the top face sheet and the foam (Figure 66), or between the bottom face sheet and the foam. The different failure modes could be due to the difference in bonding strength at the two interfaces.

The third failure mode was the circumferential buckling of the bottom face sheet. The failure can occur without complete delamination initially. As the sandwich panel was further deformed, separation of the foam blank from one of the face sheets can be observed. Figure 67 shows that along with the foam blank the buckled bottom face sheet was separated from the top face sheet. It is believed that the buckling was due to the induced hoop stress and the non-uniform adhesive strength at the interface between the bottom face sheet and the foam blank.

In the experiment at Texas A&M University, a specimen with a mixed failure mode was observed. As illustrated in Figure 68, this two-layered panel was tested until the face sheet failure, hence, there is a vertical crack on the sheet metal. In particularly, partial delamination and cracks along the foam were observed from the other side view of the specimen. The delamination area happened at the center of the disk and certain circumferential edge. Besides the biggest crack in the foam core, several cracks in the

radial direction near the disk edges were observed. The radial cracks proved that the foam proved was subjected to a biaxial stretching deformation.

From the experiment results from both apparatuses, the adhesive debonding was the most significant and earliest failure mode. To achieve a better hydroforming result, the relationship between the adhesive strength and the deflection of the panel must be analyzed. Therefore, a finite element simulation of hydroforming process was conducted to obtain a better understanding of the failure mechanisms.

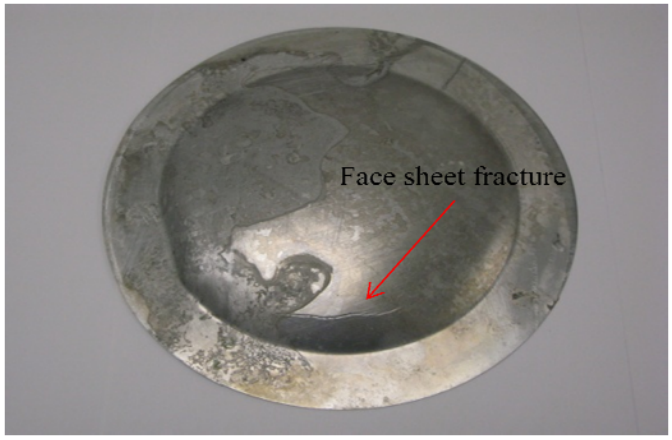

Figure 65 Fracture occurred at the top face sheet.

Figure 66 Delamination between the top face sheet and the foam blank.

Figure 67 The delamination in the sandwich panel.

Figure 68 The mixed failure mode in the two-layered panel.

5.2 Hydroforming finite element analysis

Hydroforming simulation of the two-layered panels was analyzed by using ABAQUS to investigate the effects of material properties and adhesive bonding strength on the failure modes. The simulation followed the same geometry and experiment setup with the hydraulic press experiment.

5.2.1 Finite element analysis

Due to the geometry symmetry, an axisymmetric model was created to simulate the hydroforming process of sandwich panels (as shown in Figure 69) and two-layered panels. To save the computational cost, the open-cell foam was modeled by a solid element with an equivalent material properties model. A bilinear hybrid element CAX4H was utilized in the foam and face sheets, and a removable cohesive element, COHAX4, based on the cohesive zone model, was applied in the adhesive layer. The cohesive element can be removed to demonstrate the adhesive failure after the failure criterion is satisfied. The pressure was distributed on the lower surface of the top face sheet for both the two-layered and sandwich panels. To implement the stretching forming on the top face sheet, a fixed boundary condition was added in the circumferential edge of top face sheet to constraint the sheet deformation.

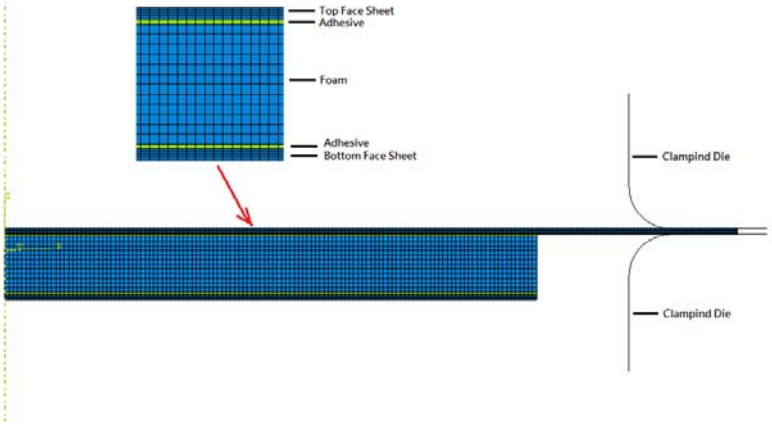

Figure 69 Finite element model of sandwich panels.

5.2.2 Material parameters

The material selection of face sheet and open-cell foam are aluminum 5052-H32 sheet metal and Duocel aluminum 6101-T6 open-cell foam respectively in this simulation. The mechanical properties of aluminum 5052-H32 were considered isotropic material and the elastic/perfect plastic material model was assumed to describe the constitutive behavior in the plastic deformation. For aluminum 5052-H32, the Young's modulus, yielding strength, and the Poisson's ratio are set at 70.3 GPa, 89.6 MPa, and 0.33 respectively.

The equivalent material models of open-cell foam material properties have been widely studies [7, 8, 15, 24, 87, 88]. The density-dependent constitutive material model developed by Gibson and Ashby [7] was adopted in this simulation. The density-dependent Young' modules E^* and plastic collapse strength σ_{ys}^* are given by

$$\frac{E^*}{E_s} = C_1 \left(\frac{\rho^*}{\rho_s}\right)^2 \tag{5.1}$$

$$\frac{\sigma_{pl}^*}{\sigma_{ys}} = C_2 \left(\frac{\rho^*}{\rho_s}\right)^{3/2} \tag{5.2}$$

where E_s, ρ_s and σ_{ys}^{pl} are the Young's modulus, density, and yield strength of the raw material in foam, respectively, and ρ^* is the density of the foam. C_1 and C_2 are geometry related constants. From the experimental data [7], the values of the constants are recommended that C_1 = 1 and C_2 = 0.3. The Poisson ratio of open-cell foam was suggested as 0.3. The open-cell foam was also assumed to have an elastic-perfect plastic behavior during the plastic deformation. In the finite element hydroforming simulations, the aluminum 6101-T6 used as the raw material of metallic foam which has the properties of E_s = 68.9 GPa and σ_{ys}^{pl} = 193 MPa. In order to investigate the effect of foam properties on the results of hydroforming process, the density of the open-cell foam was set to value of 8 %, 16 %, 24 %.

5.2.3 Cohesive zone model

Cohesive zone models have been successfully used to analyze the interface fracture of composite materials [89-91]. The technique of cohesive zone model was also capable of describing the adhesive delamination behavior. As a result, the model was applied in the adhesive layer in this hydroforming simulation. In the cohesive zone model, the adhesion in the normal and shear direction was assumed independent. To characterize the mixed mode adhesive fracture, an energy-based failure criterion is

introduced, and the cohesive element fracture will occur when the following failure criterion is satisfied:

$$\frac{G_n}{G_n^C}+\frac{G_{s1}}{G_{s1}^C}+\frac{G_{s2}}{G_{s2}^C}=1 \tag{5.3}$$

where G_n, G_{s1} and G_{s2} are the energy release rate in the normal, first shear and second shear direction, and the G_n^C, G_{s1}^C and G_{s2}^C were the energy toughness under each mode. The energy release rate is given by

$$\begin{cases} G_n=\int_0^{\sigma_n}\sigma(\delta_n)d\delta_n \\ G_{s1}=\int_0^{\sigma_{s1}}\tau(\delta_{s1})d\delta_{s1} \\ G_{s2}=\int_0^{\sigma_{s2}}\tau(\delta_{s2})d\delta_{s2} \end{cases} \tag{5.4}$$

where σ and τ are displacement-related normal and shear stress, and δ_n, δ_{s1} and δ_{s2} are the normal, first shear and second shear displacements [92].

The energy toughness is equal to the area under the stress–displacement curve in the traction–separation law. As shown in Figure 70, the normal stress σ is proportional to the displacement δ before the normal stress reached to a maximum value. Beyond the maximum normal stress, the steep drop indicates the debonding of the adhesive. Hence, the energy toughness G_n^C can be approximated as:

$$G_n^c=\frac{1}{2}\sigma\cdot\delta=\frac{1}{2}\frac{\sigma^2}{\tilde{E}/t} \tag{5.5}$$

where t is the thickness of the adhesive and $\tilde{E}$ is the modulus defined as $\tilde{E}/t=\sigma/\delta$. For simplicity, the behavior of the adhesive in the first and the second shear directions was

assumed the same as that of the normal direction in the present study. To investigate different potential failure modes, different adhesive strength values were assigned in the model. In the finite element analysis, once the energy failure criterion, Equation (5.3), is satisfied in a cohesive element, then the element is removed to depict the delamination.

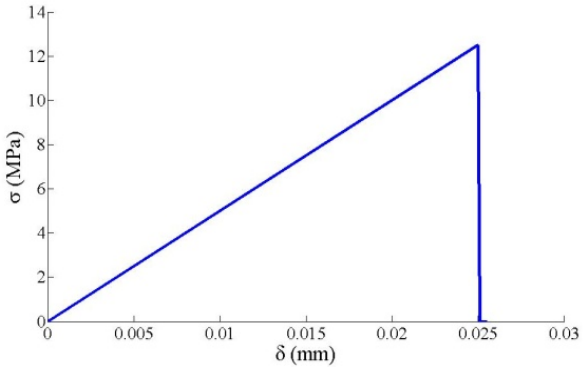

Figure 70 The normal stress to displacement plot for the adhesive bond between the face sheet and the foam.

5.2.4 Simulation parameters

There were three major parameters, adhesive strength, foam relative density and foam disk diameters, to be investigated in the hydroforming finite element simulation. The adhesive strength varied from 0.5 MPa to 6 MPa by 0.5 MPa incremental amounts, and the adhesive thickness and modulus were set at 0.3 mm and 150 MPa respectively. By adjusting the relative density of the open-cell foam (8 %, 16 %, 24 %), three different values of mechanical properties were simulated. Three different diameters of foam disks (101.6 mm, 127 mm, 152.4 mm) were also selected to simulate the disk effect to the delamination. The thickness of foam was selected at 8 mm. Besides these study

parameters, the remain geometry parameters of face sheets and open-cell foam were set as constant values.

5.3 Finite elements results and discussion

The objective of the present finite element simulations is to investigate the causes of various failure modes observed in the hydroforming experiments. It was found that the simulation results are consistent with the experimental observations. The simulation results can be used to guide the selection of the foam, and the adhesive for the hydroforming processes.

5.3.1 Failure modes in sandwich panels

From finite element simulation, it was found that the deformation behavior of sandwich panels was different from that of two-layered panels. The model in Figure 67 has 8% foam density and 1.5 MPa adhesive strength for both top and bottom interfaces. The figure shows that the bottom face sheet provides high bending rigidity and thus the deformation of the top face sheet took place mostly near the edge of the foam block. As a result, the top face sheet fracture can easily occur. If the top face sheet has a high strength to delay fracture, the delamination of the bottom face sheet can happen. To compare with the model in Figure 71, a model with the increase top adhesive strength to 6 MPa was also simulated. In Figure 72, the delamination, due to insufficient adhesion strength at the bottom interface, was initiated near the perimeter/edge of the foam and sheet metal. The delamination can shift to the top interface only when the adhesion strength at the bottom interface is much stronger than the adhesion strength at the top.

As shown earlier, the mechanical properties of the foam are determined by its relative density. For low relative density (i.e. 8 %), the delamination was initiated at the bottom interface. The upper interface can then delaminate at a later stage. A high relative density leads to a high Young's modulus, which in turn makes the foam difficult to bend. As shown in the simulation, the bottom interface was not subject to significant stress, and the delamination occurred at the top interface first.

5.3.2 Failure modes in two-layered panels

There were primarily three competing failure modes in hydroforming of two-layered panels. Figure 73 shows that the delamination can be observed for panels with low bonding strength at the sheet metal–foam interface. In this model, the panel has a low adhesive strength (1.5 MPa) and foam relative density (8%). Figure 74 shows that, with higher adhesive strength (6.0 MPa) and relative density (24%), the face sheet fracture at the clamping die radius or at the edge of the foam block can occur before delamination. With increasing strength or thickness of the face sheet, the fracture is delayed, and the failure mode can shift to delamination failure.

The maximum attainable dome height of two-layered panel was typically greater than that of the sandwich panels. This is because that the localized deformation of the top face sheet is not as severe, and there is no debonding of the bottom face sheet to be considered. Since no deformation limit is specified for the elastic-perfect plastic foam model, no foam failure was predicted. The result is in agreement with the experiments that, although the ligaments of the foam were plastically deformed, no significant damage was noted.

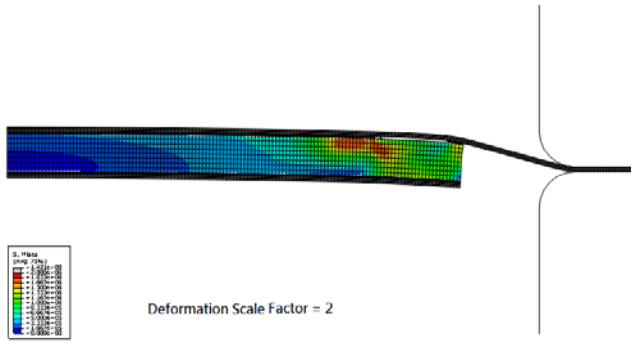

Figure 71 Face sheet stress concentration near the edge of the foam in the sandwich panel.

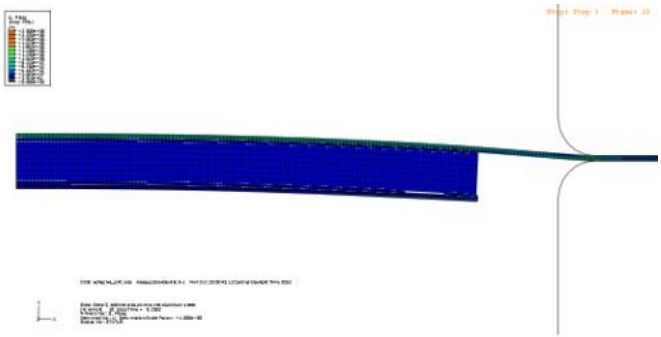

Figure 72 Bottom adhesive delamination with a lower strength in the bottom adhesive.

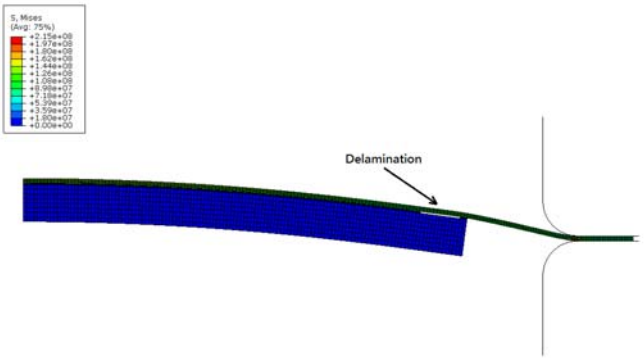

Figure 73 Delamination in two-layered panels.

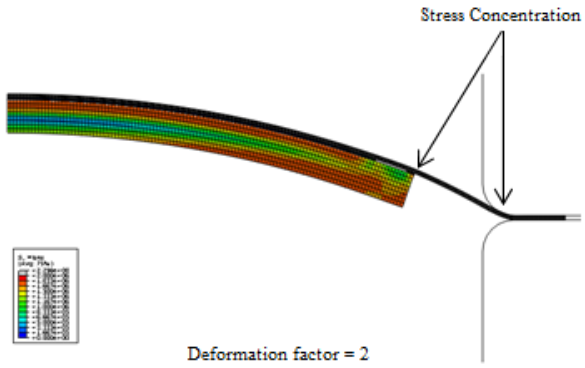

Figure 74 Face sheet stress concentration in two-layered panels.

5.3.3 Parametric study

The effect of the foam's relative density on the attainable dome height in the bulge test of two-layered panels was further investigated quantitatively. The maximum dome height at the onset of delamination was plotted against the adhesive strength for the foam blank with 8%, 16% and 24% relative density. Figure 75 shows the plots in three sizes of foam diameters, 101.6 mm, 127.0 mm, and 152.4 mm. The filled mark presented the final dome height without delamination at 2 MPa maximum hydraulic pressure.

It can be seen that the gain in the dome height due to the improved adhesion strength was initially significant (large slope) for panels with low relative density foam. Also, note that panels with high relative density foam required a stronger adhesive strength to carry the foam during the hydroforming process to achieve a specified dome height (e.g. a horizontal line at 10 mm). It can also be observed that for a given adhesive strength (e.g. a vertical line at 3 MPa), a panel with a higher relative density foam (24 %) had a lower dome height compared to a panel with a lower relative density foam (8

%). To reach a certain dome height, the difference of the required adhesive strength between each foam density was decreased with increased foam diameter as observed from Figure 76 (a) through (c).

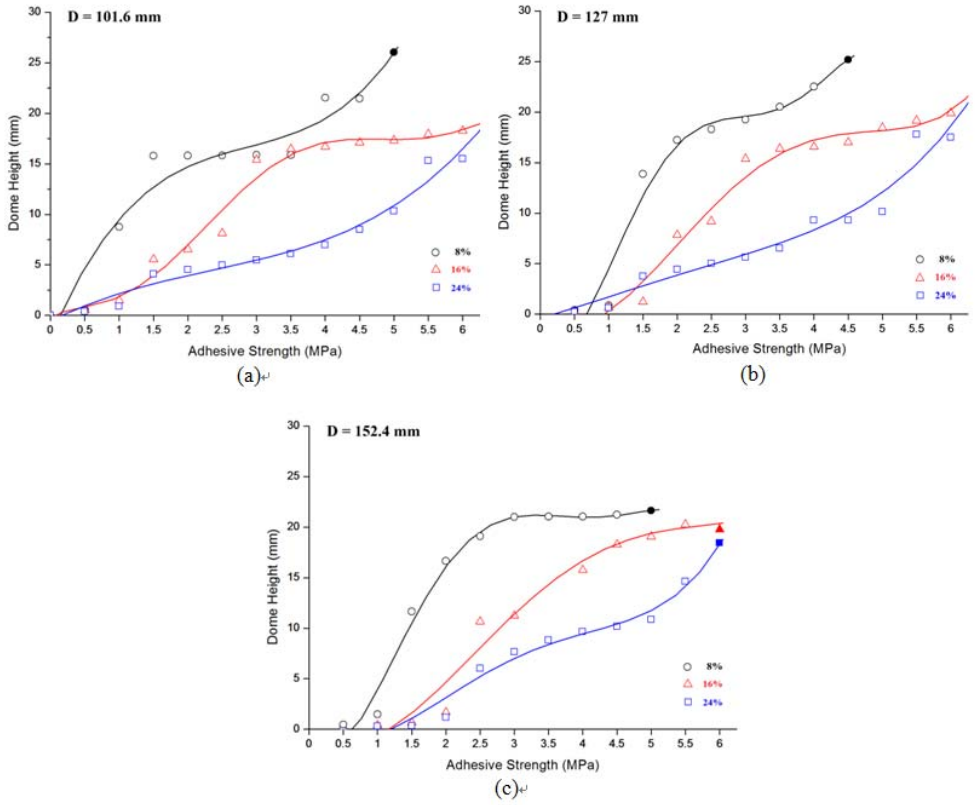

Figure 75 Maximum attainable dome height vs. adhesive strength for foam with 8 mm thickness and different diameters (D) for bi-layered panels: (a) D = 101.6mm (b) D = 127mm, (c) D = 152.4mm.

For low relative density foam (8 %), the effect of foam diameter is further illustrated in Figure 71. Without curve fitting, the data show that the dome height can reach a plateau despite an increase in adhesive strength. This could be due to continued

stress build up without bulge deformation prior to delamination. For the panel with smaller foam blank, the plateau was reached at a lower dome height compared to the panel with larger foam blank (16 mm for D = 101.6mm and 21mm for D = 152.4 mm).

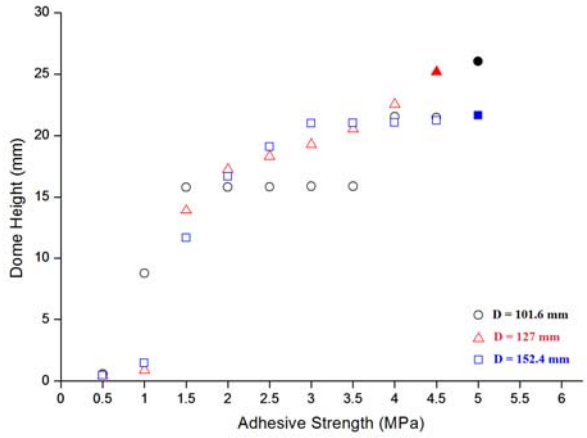

Figure 76 The maximum attainable dome height vs. adhesive strength for blanks different foam diameter for bi-layered panels.

5.4 Conclusion

Forming sandwich panels with conventional stamping die has been proven difficult as the foam core can be easily damaged during the deformation process. In this chapter, experimental work, and numerical simulation are presented to demonstrate the feasibility of using sheet hydroforming technique to form two-layered panels and sandwich panels. With metallic open-cell foam core, the hydraulic fluid can flood the pore without collapsing the foam. The approach, however, can lead to other failure modes such as face sheet fracture and delamination. Through finite element simulation of the conducted bulge test, the followings can be concluded:

- The qualitative results of finite element simulation are in agreement with experimental observation. The failure modes depend on the properties of the face sheet, the foam, and the adhesive.
- Compared to forming two-layered panels, forming sandwich panel is a more difficult task as the delamination of the bottom face sheet can easily occur.
- A low relative density of the foam can reduce the stiffness of the foam core and improve the maximum dome height in the bulge test.
- Finite element simulation of the hydroforming processes can facilitate the identification of failure modes and can be used to determine the appropriate constituents (face sheet, foam, and adhesive) of sandwich panels.
- Additional FEA simulations can be conducted to investigate the failures of sandwich panels. Other materials and tooling parameters such as the face

sheet thicknesses and properties and clamping die radius can be included in the future study.

CHAPTER VI

CONCLUSIONS AND SUGGESTIONS FOR FUTURE WORK

In this research, the press brake bending and the hydroforming processes were implemented to forming metallic open-cell foam supported sheet metals. Experiments and finite element analysis were carried to find the failure mechanism and connected to the material properties and test parameters in both processes.

For the press brake bending process, the experiment results have shown the supported sheet metal can be successfully bent into a large deformation within small thickness reduction. The most significant findings are listed below:

- Before the indentation failure occurs, the cells at the top layer go through a shear collapse deformation and form a shear band. The shear collapse is considered as the result of the excessive hoop strain in the specimen.
- A geometric hoop strain failure criterion was proposed to predict the indentation failure by the foam thickness, sheet thickness and punch radius. From the criterion, the higher density foam can go through a large hoop strain without indentation.
- A hybrid model with anisotropy Kelvin cells was conducted in the bending simulation to monitor the history strain during deformation. The idealized structure shows the buckling in the horizontal window at the top layer cell is the initial failure mechanism of the shear collapse.

- Hybrid model with 0.12 shear strain failure criterion shows a good agreement with the hoop strain failure criterion in the prediction of indentation failure.

For the hydroforming process, the test sample experienced an adhesion issue, and the open-cell foam was separated from the sheet metal at the early stage. Finite element analysis was conducted to investigate the failure mechanism, and the main discovery is listed as following:

- The primary failure mechanism is the insufficient adhesive shear strength. At the early stage, the adhesive near the perimeter of the foam disc undergo an obvious shear deformation and is the first fail location. Increasing the adhesive strength will delay the adhesive fail and attain a larger dome height.
- The dome height is affected by the attached foam properties. Lower density foam will reach a higher dome height. A higher density led a stress concentration at the sheet metal in the location of the clamping edge and the perimeter of the foam disc.

Based on the research result, there are several suggestions for the future work in both deformation processes. For press brake bending process, a further mechanical test on the deformed specimen is required. The current indentation criterion would be over restricted, and the failure sample for 3% thickness reduction may have an acceptable mechanical response. Through the understanding of the mechanical response, the indentation failure criterion can be reevaluated. Besides, the bulking behavior of the horizontal window in the Kelvin cell can be analyzed and establish a mechanism to connect the failure with the foam properties. For the hydroforming process, a better

adhesion technique needs to apply to make the open-cell foam firmly bonded with the sheet metal and continue to test the deformed behavior of the two-layered panel.

REFERENCES

[1] K.F. Karlsson, B. TomasÅström, Manufacturing and applications of structural sandwich components, Composites Part A: Applied Science and Manufacturing, 28 (1997) 97-111.

[2] D.M. Elzey, H.N.G. Wadley, Open-die forging of structurally porous sandwich panels, Metallurgical and Materials Transactions A, 30 (1999) 2689-2699.

[3] D. Mohr, On the role of shear strength in sandwich sheet forming, International Journal of Solids and Structures, 42 (2005) 1491-1512.

[4] K. Jackson, J. Allwood, The mechanics of incremental sheet forming, Journal of Materials Processing Technology, 209 (2009) 1158-1174.

[5] J. Banhart, Manufacture, characterisation and application of cellular metals and metal foams, Progress in Materials Science, 46 (2001) 559-632.

[6] E.A. Corp., The Basics of Duocel® Foam, (2011).

[7] L.J. Gibson, M.F. Ashby, Cellular solids : structure and properties, 2nd ed., Cambridge University Press, Cambridge ; New York, 1997.

[8] M.F. Ashby, Society of Automotive Engineers., Metal foams : a design guide, Butterworth-Heinemann, Woburn, MA, 2000.

[9] C. Chen, N.A. Fleck, Size effects in the constrained deformation of metallic foams, Journal of the Mechanics and Physics of Solids, 50 (2002) 955-977.

[10] N.A. Fleck, O.B. Olurin, C. Chen, M.F. Ashby, The effect of hole size upon the strength of metallic and polymeric foams, Journal of the Mechanics and Physics of Solids, 49 (2001) 2015-2030.

[11] P.R. Onck, E.W. Andrews, L.J. Gibson, Size effects in ductile cellular solids. Part I : modeling, International Journal of Mechanical Sciences, 43 (2001) 681-699.

[12] E.W. Andrews, G. Gioux, P. Onck, L.J. Gibson, Size effects in ductile cellular solids. Part II: experimental results, International Journal of Mechanical Sciences, 43 (2001) 701-713.

[13] A.M. Kraynik, W.E. Warren, The elastic behavior of low-density cellular plastics, in: Low density cellular plastics: Physical basis of behaviour, Springer Netherlands, (1994) 187-225.

[14] C. Betts, Benefits of metal foams and developments in modelling techniques to assess their materials behaviour: a review, Materials Science and Technology, 28 (2012) 129-143.

[15] H.X. Zhu, J.R. Hobdell, A.H. Windle, Effects of cell irregularity on the elastic properties of open-cell foams, Acta Materialia, 48 (2000) 4893-4900.

[16] A.N. Gent, A.G. Thomas, The deformation of foamed elastic materials, Journal of Applied Polymer Science, 1 (1959) 107-113.

[17] J.M. Lederman, The prediction of the tensile properties of flexible foams, Journal of Applied Polymer Science, 15 (1971) 693-703.

[18] P.S. Liu, Mechanical relations for porous metal foams under several typical loads of shearing, torsion and bending, Materials Science and Engineering: A, 527 (2010) 7961-7966.

[19] J. Zhou, W.O. Soboyejo, Mechanics Modeling of the Compressive Stiffness and Strength of Open-Celled Aluminum Foams, Materials and Manufacturing Processes, 19 (2004) 863-882.

[20] W.E. Warren, A.M. Kraynik, The Linear Elastic Properties of Open-Cell Foams, Journal of Applied Mechanics, 55 (1988) 341-346.

[21] W.E. Warren, A.M. Kraynik, The Nonlinear Elastic Behavior of Open-Cell Foams, Journal of Applied Mechanics, 58 (1991) 376.

[22] W.E. Warren, A.M. Kraynik, Linear Elastic Behavior of a Low-Density Kelvin Foam With Open Cells, Journal of Applied Mechanics, 64 (1997) 787-794.

[23] B. Budiansky, E. Kimmel, Elastic Moduli of Lungs, Journal of Applied Mechanics, 54 (1987) 351-358.

[24] L.J. Gibson, Mechanical Behavior of Metallic Foams, Annual Review of Materials Science, 30 (2000) 191-227.

[25] C.H. Rycroft, Voronoi volumes and local density - Introduction, Harvard University, (2014).

[26] A.G. Dement'ev, O.G. Tarakanov, Effect of cellular structure on the mechanical properties of plastic foams, Polymer Mechanics, 6 (1970) 519-525.

[27] H.X. Zhu, N.J. Mills, J.F. Knott, Analysis of the high strain compression of open-cell foams, Journal of the Mechanics and Physics of Solids, 45 (1997) 1875-1904.

[28] H.X. Zhu, J.F. Knott, N.J. Mills, Analysis of the elastic properties of open-cell foams with tetrakaidecahedral cells, Journal of the Mechanics and Physics of Solids, 45 (1997) 319-343.

[29] L. Gong, S. Kyriakides, W.Y. Jang, Compressive response of open-cell foams. Part I: Morphology and elastic properties, International Journal of Solids and Structures, 42 (2005) 1355-1379.

[30] W.-Y. Jang, S. Kyriakides, On the crushing of aluminum open-cell foams: Part II analysis, International Journal of Solids and Structures, 46 (2009) 635-650.

[31] H.X. Zhu, A.H. Windle, Effects of cell irregularity on the high strain compression of open-cell foams, Acta Materialia, 50 (2002) 1041-1052.

[32] C. Tekog˜lu, L.J. Gibson, T. Pardoen, P.R. Onck, Size effects in foams: Experiments and modeling, Progress in Materials Science, 56 (2011) 109-138.

[33] L. Li, P. Xue, Y. Chen, H.S.U. Butt, Insight into cell size effects on quasi-static and dynamic compressive properties of 3D foams, Materials Science and Engineering: A, 636 (2015) 60-69.

[34] L. Gong, S. Kyriakides, Compressive response of open cell foams Part II: Initiation and evolution of crushing, International Journal of Solids and Structures, 42 (2005) 1381-1399.

[35] L. Gong, S. Kyriakides, N. Triantafyllidis, On the stability of Kelvin cell foams under compressive loads, Journal of the Mechanics and Physics of Solids, 53 (2005) 771-794.

[36] W.-Y. Jang, A.M. Kraynik, S. Kyriakides, On the microstructure of open-cell foams and its effect on elastic properties, International Journal of Solids and Structures, 45 (2008) 1845-1875.

[37] W.-Y. Jang, S. Kyriakides, On the crushing of aluminum open-cell foams: Part I. Experiments, International Journal of Solids and Structures, 46 (2009) 617-634.

[38] W.-Y. Jang, S. Kyriakides, A.M. Kraynik, On the compressive strength of open-cell metal foams with Kelvin and random cell structures, International Journal of Solids and Structures, 47 (2010) 2872-2883.

[39] S. Gaitanaros, S. Kyriakides, A.M. Kraynik, On the crushing response of random open-cell foams, International Journal of Solids and Structures, 49 (2012) 2733-2743.

[40] A.T. Barnes, K. Ravi-Chandar, S. Kyriakides, S. Gaitanaros, Dynamic crushing of aluminum foams: Part I – Experiments, International Journal of Solids and Structures, 51 (2014) 1631-1645.

[41] S. Gaitanaros, S. Kyriakides, Dynamic crushing of aluminum foams: Part II – Analysis, International Journal of Solids and Structures, 51 (2014) 1646-1661.

[42] D. Okumura, Y. Takahashi, N. Ohno, Influence of closed faces on compressive strength of open cell metallic foams, Materials Research Innovations, 15 (2013) s61-s64.

[43] D. Okumura, T. Kuwayama, N. Ohno, Effect of geometrical imperfections on swelling-induced buckling patterns in gel films with a square lattice of holes, International Journal of Solids and Structures, 51 (2014) 154-163.

[44] L. Dong, V. Deshpande, H. Wadley, Mechanical response of Ti–6Al–4V octet-truss lattice structures, International Journal of Solids and Structures, 60-61 (2015) 107-124.

[45] L. Dong, H. Wadley, Mechanical properties of carbon fiber composite octet-truss lattice structures, Composites Science and Technology, 119 (2015) 26-33.

[46] T. Tancogne-Dejean, A.B. Spierings, D. Mohr, Additively-manufactured metallic micro-lattice materials for high specific energy absorption under static and dynamic loading, Acta Materialia, 116 (2016) 14-28.

[47] L.-J. Feng, L.-Z. Wu, G.-C. Yu, An Hourglass truss lattice structure and its mechanical performances, Materials & Design, 99 (2016) 581-591.

[48] O.E. Sotomayor, H.V. Tippur, Role of cell regularity and relative density on elastoplastic compression response of 3-D open-cell foam core sandwich structure generated using Voronoi diagrams, Acta Materialia, 78 (2014) 301-313.

[49] L. Yang, O. Harrysson, H. West, D. Cormier, A Comparison of Bending Properties for Cellular Core Sandwich Panels, Materials Sciences and Applications, 04 (2013) 471-477.

[50] X. Zhu, S. Ai, X. Lu, K. Cheng, X. Ling, L. Zhu, B. Liu, Collapse models of aluminum foam sandwiches under static three-point bending based on 3D geometrical reconstruction, Computational Materials Science, 85 (2014) 38-45.

[51] A. Xu, T. Vodenitcharova, K. Kabir, E.A. Flores-Johnson, M. Hoffman, Finite element analysis of indentation of aluminium foam and sandwich panels with aluminium foam core, Materials Science and Engineering: A, 599 (2014) 125-133.

[52] J. Zhang, Q. Qin, W. Ai, H. Li, T.J. Wang, The Failure Behavior of Geometrically Asymmetric Metal Foam Core Sandwich Beams Under Three-Point Bending, Journal of Applied Mechanics, 81 (2014) 071008.

[53] S.P. Timoshenko, On the correction for shear of the differential equation for transverse vibrations of prismatic bars, Philosophical Magazine, 41 (1921) 744-746.

[54] S.P. Timoshenko, On the transverse vibrations of bars of uniform cross-section, Philosophical Magazine, 43 (1922) 125-131.

[55] C. Wang, G. Kinzel, T. Altan, Mathematical modeling of plane-strain bending of sheet and plate, Journal of Materials Processing Technology, 39 (1993) 279-304.

[56] R. Hill, C. A theory of the plastic bulging of a metal diaphragm by lateral pressure, The London, Edinburgh, and Dublin Philosophical Magazine and Journal of Science, 41 (1950) 1133-1142.

[57] J. Lubahn and G. Sachs, Bending of an ideal plastic metal , Trans. ASME , 72 (1950) 201-208.

[58] R. Hill, On the problem of uniqueness in the theory of a rigid-plastic solid—IV, Journal of the Mechanics and Physics of Solids, 5 (1957) 302-307.

[59] F. Proksa, Zur Theorie des Plastischen Blechbiegens, Diss. T.H., (1958).

[60] T.X. Yu, W. Johnson, Influence of axial force on the elastic-plastic bending and springback of a beam, Journal of Mechanical Working Technology, 6 (1982) 5-21.

[61] K.A. Stelson, D.C. Gossard, An Adaptive Pressbrake Control Using an Elastic-Plastic Material Model, Journal of Manufacturing Science and Engineering, 104 (1982) 389-393.

[62] K.A. Stelson, An Adaptive Pressbrake Control for Strain-Hardening Materials, Journal of Engineering for Industry, 108 (1986) 127.

[63] F. Pourboghrat, K.A. Stelson, Pressbrake Bending in the Punch-Sheet Contact Region—Part 1: Modeling Nonuniformities, Journal of Manufacturing Science and Engineering, 110 (1988) 124-130.

[64] F. Pourboghrat, K.A. Stelson, Pressbrake Bending in the Punch-Sheet Contact Region—Part 2: Gap Formation and the Direction of Sheet Motion, Journal of Manufacturing Science and Engineering, 110 (1988) 131-136.

[65] F.J. Plantema, Sandwich Construction: The Bending and Buckling of Sandwich Beams, Plates and Shells, (1966).

[66] H.G. Allen, Analysis and design of structural sandwich panels, 1st ed., Pergamon Press, Oxford, New York, 1969.

[67] D. Zenkert, The Handbook of Sandwich Construction, (1997).

[68] I.J. V. Straalen, Comprehensive Overview of Theories for Sandwich Panels, Modeling of Sandwich Structures and Adhesive Bonded Joints, (2000) 48-70.

[69] Y. Frostig, M. Baruch, Bending of sandwich beams with transversely flexible core, AIAA Journal, 28 (1990) 523-531.

[70] Y. Frostig, Behavior of delaminated sandwich beam with transversely flexible core — high order theory, Composite Structures, 20 (1992) 1-16.

[71] Y. Frostig, On stress concentration in the bending of sandwich beams with transversely flexible core, Composite Structures, 24 (1993) 161-169.

[72] T.C. Triantafillou, L.J. Gibson, Failure mode maps for foam core sandwich beams, Materials Science and Engineering, 95 (1987) 37-53.

[73] T.M. McCormack, R. Miller, O. Kesler, L.J. Gibson, Failure of sandwich beams with metallic foam cores, International Journal of Solids and Structures, 38 (2001) 4901-4920.

[74] C. Chen, A.M. Harte, N.A. Fleck, The plastic collapse of sandwich beams with a metallic foam core, International Journal of Mechanical Sciences, 43 (2001) 1483-1506.

[75] H. Bart-Smith, J.W. Hutchinson, A.G. Evans, Measurement and analysis of the structural performance of cellular metal sandwich construction, International Journal of Mechanical Sciences, 43 (2001) 1945-1963.

[76] F. Vollertsen, State of the art and perspectives of hydroforming of tubes and sheets, J. Mater. Sci. Technol., 17 (2001) 321-324.

[77] J. Chakrabarty, J.M. Alexander, Hydrostatic bulging of circular diaphragms, The Journal of Strain Analysis for Engineering Design, 5 (1970) 155-161.

[78] H.M. Shang, T.C. Hsü, Deformation and Curvatures in Sheet-Metal in the Bulge Test, Journal of Engineering for Industry, 101 (1979) 341.

[79] H.M. Shang, V.P.W. Shim, A model study of the effect of the size of the die shoulder in hydroforming, Journal of Mechanical Working Technology, 10 (1984) 307-323.

[80] H.M. Shang, F.S. Chau, C.J. Tay, S.L. Toh, An approximate solution for the hydrostatic bulging of circular diaphragms with draw-in allowed, Journal of Mechanical Working Technology, 13 (1986) 279-289.

[81] P. Hein, F. Vollertsen, Hydroforming of sheet metal pairs, Journal of Materials Processing Technology, 87 (1999) 154-164.

[82] L.B. Shulkin, R.A. Posteraro, M.A. Ahmetoglu, G.L. Kinzel, T. Altan, Blank holder force (BHF) control in viscous pressure forming (VPF) of sheet metal, Journal of Materials Processing Technology, 98 (2000) 7-16.

[83] J. Zhou, Z. Gao, S. Allameh, E. Akpan, A.M. Cuitino, W.O. Soboyejo, Multiscale Deformation of Open Cell Aluminum Foams, Mechanics of Advanced Materials and Structures, 12 (2005) 201-216.

[84] ASTM Standard E2712-09e1, Test Methods for Forming Superplastic Metallic Sheet, ASTM International, (2009).

[85] J. Wang, C.-K. Yang, Failure analysis of hydroforming of sandwich panels, Journal of Manufacturing Processes, 15 (2013) 256-262.

[86] S. Mahabunphachai, M. Koç, Investigations on forming of aluminum 5052 and 6061 sheet alloys at warm temperatures, Materials & Design, 31 (2010) 2422-2434.

[87] E. Andrews, W. Sanders, L.J. Gibson, Compressive and tensile behaviour of aluminum foams, Materials Science and Engineering: A, 270 (1999) 113-124.

[88] L. Peroni, M. Avalle, M. Peroni, The mechanical behaviour of aluminium foam structures in different loading conditions, International Journal of Impact Engineering, 35 (2008) 644-658.

[89] S. Li, M. Thouless, A. Waas, J. Schroeder, P. Zavattieri, Use of a cohesive-zone model to analyze the fracture of a fiber-reinforced polymer?matrix composite, Composites Science and Technology, 65 (2005) 537-549.

[90] S. Li, M.D. Thouless, A.M. Waas, J.A. Schroeder, P.D. Zavattieri, Use of mode-I cohesive-zone models to describe the fracture of an adhesively-bonded polymer-matrix composite, Composites Science and Technology, 65 (2005) 281-293.

[91] S. Li, M.D. Thouless, A.M. Waas, J.A. Schroeder, P.D. Zavattieri, Mixed-mode cohesive-zone models for fracture of an adhesively bonded polymer–matrix composite, Engineering Fracture Mechanics, 73 (2006) 64-78.

[92] D. Systèmes, ABAQUS Analysis User's Manual, version 6.9-EF, (2009) 25.29.26.